UNIVERSITÀ DEGLI STUDI DI MILANO-BICOCCA
Dipartimento di Scienza dei Materiali

Doctorate in Nanostructures and Nanotechnologies

Spin physics of Ge-based heterostructures

Doctorate thesis of
Anna Giorgioni

Supervisor : Prof. Mario Guzzi

Coordinator: Prof. Gianfranco Pacchioni

Doctorate Cycle XXVI

To my husband

Contents

Introduction

Spin physics is a wide and rich field: having his roots in the 1920s, it was at the basis of a number of discoveries in the last century. In the case of semiconductors spin physics has been particularly rich from the 1950s up to now for the understanding of the fundamental physical properties of these materials. In addition, some researchers conceive semiconductor materials at the basis of possible spintronic applications.

Besides the electrical spin injection, semiconductors offer the possibility to investigate the carrier spin by means of polarized light, providing a tool to efficiently orient carrier spins, read and manipulate the spin states [1]. Moreover, in these materials the carriers can present slow decoherence effects and long spin lifetime.

A lot of data and several theoretical works were mainly reported in the literature on the spin properties of carriers in III-V compounds. The Dyakonov-Perel relaxation mechanism dominates the spin dynamics of conduction electrons in these systems. III-V quantum wells (QWs) were widely investigated, providing a quite interesting system to study the effects of confinement on the spin properties of the carriers [2, 3].

Group IV materials, on the other hand, show peculiar differences respect

to III-V semiconductors. First, the centrosymmetric crystal prevents the Dyakonov-Perel spin relaxation mechanism [3], and the isotopic refinement can reduce the hyperfine interaction [4], thus providing a longer electron spin lifetime. Second, from a spintronic point of view, group IV semiconductors offer a feasible integrability on the well-established Si platform. In fact, the literature reports a wide investigation of teh spin properties of bulk silicon and Si-based nanostructures. A plenty of works discuss electrical injection, detection and manipulation of the carrier spin [5, 6], because of the important role of the electric control in the device implementation. Particularly, nowadays a number of researchers study Si and SiGe quantum dots in order to create spin quantum bits aiming to Si spintronics: such an activity has provided a deepening in the understanding of quantum phenomena in Si [7]. Besides, the fundamental properties of the spin of electrons confined in Si quantum wells (QWs) [8], quantum dots [9] and nanowires continues to stimulate the research interest. One of the interesting features of these systems consists in the small spin-orbit coupling of Si, resulting in the possibility to study conduction electrons by the Electron Spin Resonance (ESR) technique [10]. Optical orientation of conduction electrons in Si was demonstrated already in the late 1960s [11], although in this direction very little improvement has been achieved so far. The main reason lies in the indirect nature of the fundamental gap, which in these materials hampers the exploitation of photoluminescence measurements.

Recently it has been recognized that the Ge band structure provides an effective means [12] to overcome the aforementioned shortcoming, opening up the possibility to perform optical investigations of the spin properties also in group IV semiconductors. In contrast to Si, in Ge the energy

difference between the Γ and the fundamental *L* minima of the conduction band is small, so that the radiative recombination through the direct gap can be observed together with the one through the indirect gap [12]. As a result, Ge offers the possibility to fully exploit the coupling between the angular momentum of circularly polarized photons and the electronic spin states. On one hand, carrier spins can be efficiently oriented by the absorption of circularly polarized light through the direct gap, and on the other hand, the polarization of the emitted photons provides information on the spin orientation of carriers when they recombine radiatively. Since the direct and the indirect gap recombination are characterized by different decay times, the detection of both emissions provides the possibility to investigate different time scale dynamics of the carrier spins. Particularly, the polarization of the direct (indirect) gap emission reveals information on the hole (electron) spin lifetime. In addition, Ge is characterized by a higher carrier mobility with respect to Si, which is useful for spin transport experiments [13], and importantly, the heavier atomic mass provides a larger spin-orbit coupling resulting in a highly anisotropic *g* factor [14]. This feature constitutes an efficient tool for the manipulation of the carrier spin. According to recent studies, this can be achieved by applying an external electric field to the sample [15].

The *g* factor of electrons in bulk Ge was widely investigated by means of ESR measurements on doped samples [16, 17]. These studies report about donor electrons. The localization on an impurity atom indeed usually results in a longer electron spin lifetime, with the consequent possibility to investigate the carrier spin by means of ESR [16]. The spin properties of conduction electrons, instead, were initially studied by spin polarized

photoemission measurements [18]. In the last years the first studies of the spin lifetime of conduction band electrons [19] and valence band holes in Ge [20, 21] appeared in the literature. The group of Prof. H. Dery at Rochester calculated the first theoretical model of the spin dynamics of electrons in the *L* valley of the conduction band [22], assuming the Elliott-Yafet mechanism [3] as the most important source of depolarization, since the Dyakonov-Perel spin relaxation process is hampered in Ge as in Si. In the work by Dery et al. [22], the electron-phonon interaction results in an extremely long conduction electron spin lifetimes at low temperatures ($\sim$10 ms at T=10 K). Besides, the first experimental data were reported, providing estimations of the electron spin lifetime in agreement with the theoretical calculation for T>30 K [23, 24].

In the meantime, I undertook the study of the spin properties of conduction electrons in Ge and Ge-based systems by optical means. The aim of my work is to demonstrate the possibility of an all-optical study of the spin properties of free carriers in Ge-based systems, and to provide a characterization, as complete as possible, of the electron spin, eventually including the evaluation of the spin lifetime. I employed the polarization-resolved photoluminescence technique, that resulted to be an efficient tool to address the spin dynamics of the photoexcited carriers. A great advantage of the optical injection and detection is to avoid the spin depolarization due to the interfaces between ferromagnetic and semiconductor materials that affects the electrical measurements, and reduces the estimated spin lifetime [25, 26]. The information provided by the analysis of the photoluminescence signal due to the direct and the indirect transitions were compared with the results of a theoretical calculation, creating a solid basis for the data interpretation.

In addition, I carried out ESR measurements on Ge-based heterostructures. Up to now, ESR is the most accurate technique to determine the g factor of electrons, and this allowed me to address the spin-orbit coupling of confined carriers in Ge QWs. Moreover, the detection of the spin resonance line provides information on the spin decoherence and relaxation processes which dominate the carrier spin dynamics.

In this thesis, I investigate: 1) the optical injection of carrier spins and the polarization of the photoluminescence in bulk Ge and Ge heterostructures; 2) the possible ways to optically control the spin orientation, mainly related to the confinement degree of freedom; 3) the spin dynamics in the multivalley conduction band of Ge-based systems and the relaxation mechanisms governing the spin depolarization 4) the spin-orbit coupling of conduction electrons confined in quantum wells; 5) the spin lifetime of free carriers both in bulk and confined structures.

The present thesis is organized as follows: the first chapter addresses the spin properties of free carriers in bulk Ge by means of polarization-resolved photoluminescence measurements. Data of the polarization of the direct gap emission from low to room temperature and for samples with different doping are compared with the results of a Monte Carlo simulation, resulting in a detailed outline of the spin dynamics. The physical picture is confirmed by the data of the indirect gap emission, that are used to study the spin lifetime of electrons in the L valleys, and provide the first experimental evidence of the extremely long electron spin lifetime at low temperature. In addition, the effects of the carrier density on the polarization of the direct gap emission are shown.

Chapters 2 and 3 report the study of the photoluminescence polarization

in Ge QWs, and demonstrate the optical injection in these systems. In Ge QWs the compressive strain removes the degeneration between light and heavy hole bands at the center of the Brillouin zone; thus the direct gap recombinations involving heavy holes and light holes can be detected separately. In chapter 2 the analysis of these two emissions is exploited to describe the spin dynamics of holes in the confined system. Data of the indirect gap emission are compared with the theoretical prediction of the intrinsic spin lifetime of electrons, resulting in the evaluation of the spin lifetime of $\sim$5 ns around T=150 K. Chapter 3 reports the analysis of the effects of confinement on the optical spin polarization of photoexcited electrons in the Γ valley of the conduction band, through the study of the polarization of the lowest energy direct gap emission. The confinement degree of freedom is demonstrated to be an efficient tool to tailor the initial polarization of the oriented spins.

In chapter 4 the ESR study of Ge QWs is reported. The first measurements of the *g* factor of conduction electrons confined in a Ge-based system are shown, together with the demonstration of the confinement effects. The study of the lineshape of the spin resonances of conduction electrons provides the first information on the spin decoherece time and on the spin relaxation time at T=2 K in these systems.

Finally, in the Conclusions the results reported in the thesis are revised and discussed. In the last part some appendixes are found. In Appendix A the polarization-resolved photoluminescence technique, the experimental apparatus and the Stokes analysis of the polarization of light are described. Appendix B reports a list of data of the polarization of the direct gap emission of bulk Ge samples as a function of the excitation power density,

that supports the discussion in section 1.2.2. In Appendix C a description of the Ge QW samples structure is reported, and Appendix E reports a discussion of the ESR technique, of the cyclotron resonance and of the spin resonance signals.

Part I

Bulk germanium

Chapter 1

Spin relaxation and carrier dynamics

In the present chapter we address optical orientation of spins in intrinsic and doped bulk Ge. Ge is an elemental semiconductor of the group IV of the periodic table, characterized by an indirect fundamental gap (see Fig. 1.1). The top of the valence band (VB), at the Γ point of the Brillouin zone, is doubly degenerate, and it consists of the heavy hole (HH) and the light hole (LH) bands. The split-off band (SO) is located 290 meV below the top of the VB. The conduction band (CB) presents the absolute minimum at the L points: the L valley is four times degenerate, and at room temperature (RT) its energy is 0.66 eV above the top of the VB. Local minima of the CB are found at the Γ and X points, 140 meV and 200 meV above the absolute minimum, respectively.

Our study relies on the photoluminescence (PL) properties of Ge. We report PL measurements carried out in backscattering configuration, using

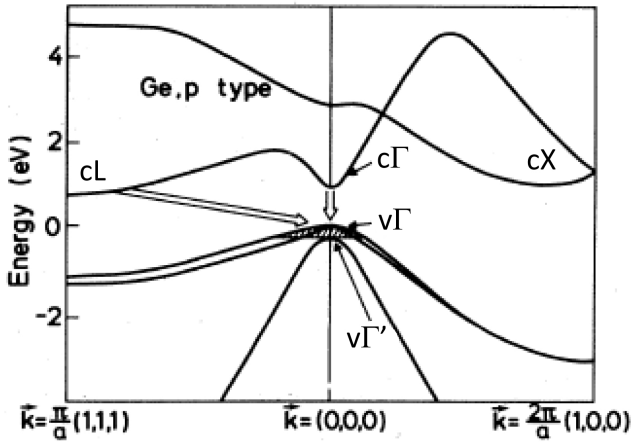

Figure 1.1: Band structure of bulk Ge from Ref. [27]. The shadowed region indicates the hole population for a p-type sample. The two arrows sketch the direct transition cΓ →vΓ, and the indirect transition cL→vΓ.

the 1.165 eV line of a Nd:YVO_4 laser, with a power density ranging from $\sim$0.05 to 2kW/cm^2. We employed two InGaAs array detectors, characterized by 0.75 eV and 0.56 eV cutoff energies, depending on the PL features of interest.

The use of a near infrared excitation allowed us to enhance optical access to the Γ states in the CB, and to exploit the large absorption coefficient of the direct gap interband transitions ($\sim 10^4$ cm^{-1} [28]). After excitation to the Γ valley, electrons thermalize and are distributed in the CB before recombination. Fig. 1.1 shows the energy profile of the CB: thanks to the small energy distance between the Γ and the *L* valleys, electrons recombine radiatively through the direct and the indirect gaps. Therefore, one can detect at the same time the PL from the two transitions, at different photon

energies. This peculiarity provides an interesting tool to investigate the carrier relaxation, because it provides the ability to gather several information on the thermalization process.

In order to address the spin properties, we employed the polarization resolved photoluminescence (PRPL) technique (App. A). In this case the excitation was circularly polarized, and the emitted light was analyzed by a rotating quarter waveplate retarder followed by a linear polarizer, to study the polarization of photons (App. A.2). In the following, we use the symbol σ^- (σ^+) to indicate the left (right) handed circularly polarized light. PRPL exploits the coupling between the angular momentum of circularly polarized photons and the spin degree of freedom of electrons in semiconductors, in order to orient carrier spins and to observe the effects of the spin orientation on the radiative recombination. First we report a study of the polarization of the direct gap PL emission as a function of doping, temperature and excitation power. Our results highlight the rich dynamics of photoexcited electrons in Ge. The comparison of the experimental findings with theoretical predictions reveals many details of the carrier behavior related to the multi-valley CB, pointing out the so far overlooked role of scattering to the X valleys during the electron thermalization. We demonstrate how doping, temperature and excitation power are used to control the depolarization mechanisms of the direct gap emission.

Second, in section 1.3 the indirect gap PL emission is considered. The PRPL study offers a confirmation of the physical picture obtained by the analysis of the direct gap emission. It provides an evaluation of the spin lifetime of electrons in the L valley, which is found in the order of hundreds of μs at $T = 4$ K, in agreement with the theoretical prediction. To the best of our knowledge, this time is longer than all the measured values reported in the literature so far.

Table 1.1: Analysed bulk Ge(001) samples: free carrier concentrations have been obtained by means of RT resistivity. The $n-$Ge sample is 6° miscut.

Ge sample	free carrier concentration (cm^{-3})	resistivity ($\Omega \cdot cm$)
i	$\approx 10^{13}$	47
p^-	1.4×10^{15}	2.39
n	8.3×10^{16}	0.358
p^+	3.6×10^{18}	0.0046

1.1 Photoluminescence of bulk Ge

During our PL measurements, electrons are mostly photogenerated in the Γ states of the CB (Fig. 1.1). Since Ge lacks the Froelich interaction due to its purely covalent bonds [29], scattering to lower energy valleys turns out to be much more efficient than the electron thermalization to the bottom of the Γ valley. The phonon-mediated transfer of electrons to the side valleys takes a few hundred femtoseconds [30], therefore limiting the lifetime of electrons in the Γ states. On the other hand, the large number of electrons reaching the L valleys reside there for hundreds of μs (at T = 300 K) before recombination [31, 32], due to the indirect nature of the cL$\rightarrow$vΓ transition.

In Fig.1.2 we report the PL spectra obtained in this work, at T = 4 K. Parameters of the samples studied are reported in Table 1.1.

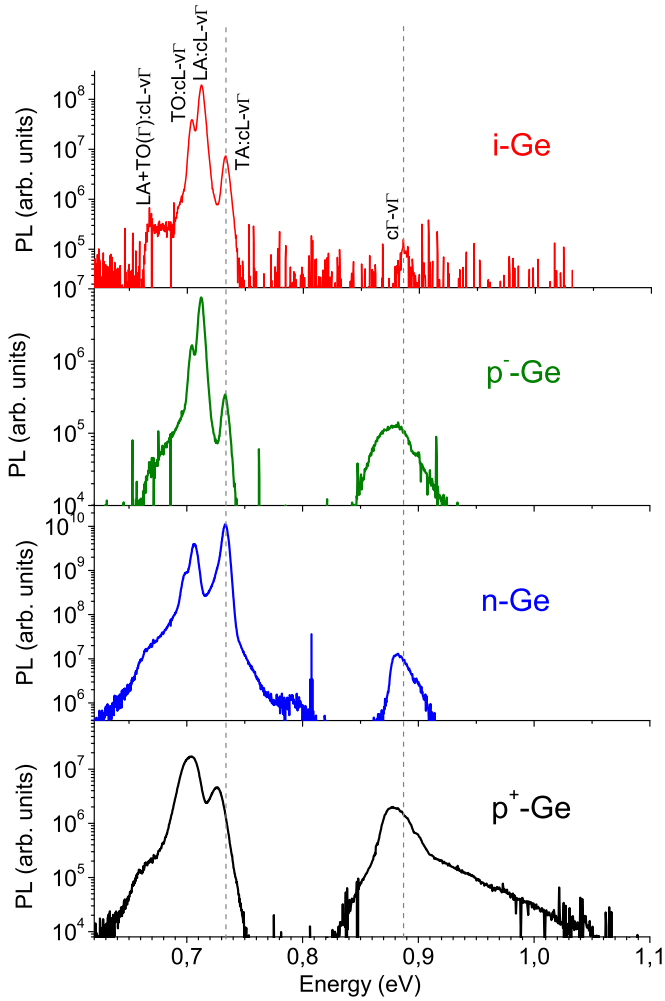

Figure 1.2: PL spectra of samples $i-$Ge, $p^{-}-$Ge, $p^{+}-$Ge, and $n-$Ge (described in Tab. 1.1) measured at T = 4 K, under excitation with 1.165 eV laser (power density $\sim$4.5 kW/cm^2). The phonon mediated indirect $L \rightarrow \Gamma$ transitions (cL-vΓ) and the direct transition (cΓ-vΓ) are labeled on the $i-$Ge spectrum. Dashed lines indicate the peak positions of the cΓ-vΓ and the TA:cL-vΓ emissions from $i-$Ge sample.

Table 1.2: Energies of (111) phonons in bulk Ge at 4 K [33], and positions of the PL peaks of the corresponding phonon replicas of the indirect cL→vΓ emission for the samples of Tab. 1.1. NP stands for 'no-phonon': in doped samples indirect transitions can eventually take place without the phonon assistance. Energies are in meV.

phonon	phonon energy	$i-$Ge	p^--Ge	$n-$Ge	p^+-Ge
TA (or NP)	7.7	733	733	732	727
LA	27.4	712	712	705	704
TO	35.4	704	704	699	

In all the PL spectra the emission due to the indirect cL→vΓ transitions (we will refer to them as 'indirect emission') dominates over the emission due to the direct cΓ →vΓ transition (we will refer to that as 'direct emission').

PL features related to the indirect emission are found in the energy range between 0.6 and 0.8 eV. The main peaks in the spectra are phonon replicas [34] of the cL →vΓ transition (742 meV for pure Ge at 4 K [35]). In the spectrum of $i-$Ge we find the following peak energies: 733 meV for the TA-phonon replica, 712 meV for the LA-phonon replica, and 704 meV for the TO-phonon replica. In the doped samples the highest energy line of the indirect emission may be due to no-phonon (NP) recombination, rather than to the TA-phonon replica. Indeed, impurities alter the periodic potential providing a possible breaking of the selection rules of the crystalline momentum. At ∼662 meV, the spectra of all the samples show a structure presenting much lower intensity (about 500 times) with respect to the previous lines. Lieten et al. attributed this feature to radiative recombination

assisted by two phonons: a (111) LA phonon (Tab. 1.2) and a TO phonon at the Γ point of the Brillouin zone [34].

In the spectra of the doped samples the PL peaks are broader compared to the ones of $i-$Ge due to disorder induced by impurities (see Fig. 1.2). In the PL spectrum of $p^{+}-$Ge the broadening is so large that the TO-phonon replica can not be resolved.

The PL peak of the direct emission is found at $\sim$880 meV for all the samples. In the spectra of the doped samples, the direct emission lines are red shifted with respect to the one of $i-$Ge (886 meV). This is an effect of the band gap narrowing [36]: the higher the dopant concentration, the larger the shift (see Fig. 1.3). As a general trend, the integrated intensity of the direct emission increases with the doping level.

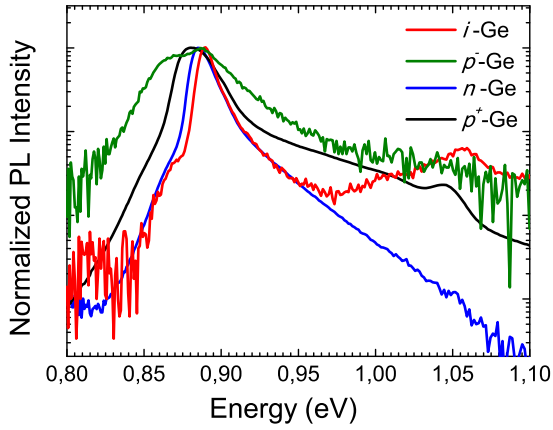

Figure 1.3: Normalized PL spectra between 0.8 and 1.1 eV at T = 4 K, using an InGaAs photodiode array detector with cutoff at 0.75 eV. The low energy feature at $\sim$0.87 eV, that can be observed in sample $p^{-}-$Ge, may be tentatively attributed to recombination of carriers bound to shallow states.

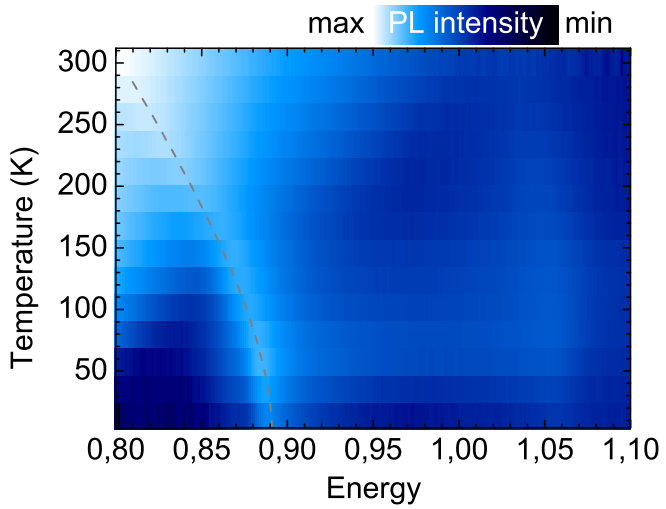

Figure 1.4: Colour-plot of the PL direct emission from $i-$Ge vs temperature. The dashed line indicates the calculated energy position of the PL peak of the direct emission [37]. In these measurements the detection was carried out with a 0.75 eV cutoff InGaAs photodiode array. The colour code for the PL intensity is shown above the figure.

In Fig. 1.3 we report the PL spectra of the direct emission, measured in all the samples of Tab. 1.1. The PL peaks are characterized by a long tail on the high energy side, due to the carrier distribution in the Γ valley. The feature at $\sim$1.05 eV in the spectra of $p^{+}-$Ge and $i-$Ge will be discussed in section 1.4.

Figure 1.4 shows a colour-plot of the PL direct emission from $i-$Ge, as a function of the temperature, T. The peak position follows the behavior described by the Varshni's law [37]

$$E_G(T) = 0.8853 \pm 0.0002 - \frac{(6.5 \pm 0.7) \cdot 10^{-4} \cdot T}{T + (410 \pm 100)} \qquad (1.1)$$

for the shift of the fundamental gap to lower energies when the temperature increases. Noteworthy, the structure at 1.056 eV remains almost at the same energy over the whole temperature range, and becomes weak when the temperature rises.

1.2 Direct gap polarized emission

In the previous section we have shown that the PL emission due to $\Gamma \rightarrow \Gamma$ transition can be observed from bulk Ge, after excitation by infrared laser light. In this section we report a PRPL study of the direct gap emission.

Polarization-resolved PL measurements were carried out in backscattering configuration, using the 1.165 eV line of a Nd:YVO_4 laser with $\sigma-$ circular polarization. The light emitted by the sample is filtered by a rotating quarter waveplate retarder followed by a linear polarizer, and analyzed by a polichromator. Emitted photon energy is given with an accuracy of 6 meV. PL spectra are measured at different orientation angles θ between the fast axis of the analyzing quarter waveplate and the linear polarizer axis. The dependence of the intensity of each PL peak on θ allowed us to perform a Stokes analysis (App. A.2) of the data, from which the polarization degree (ρ) and type were obtained. ρ is given by the ratio between the intensity of the polarized component and the total intensity of the detected light. ρ is related to the spin polarization of the photoexcited carriers right after the absorption $P_S(t = 0)$, the carrier lifetime τ, and the spin lifetime τ_s, through

the relation [1]:

$$\rho = \frac{\rho_0}{1+\tau/\tau_s} \sim \frac{P_S(t=0)}{1+\tau/\tau_s} \tag{1.2}$$

where ρ_0 is the expected polarization degree of the PL in the absence of depolarization mechanisms. Since the spin relaxation of holes in Ge is fast due to the strong mixing of the valence spin and orbital states [3, 21], the helicity and the polarization degree of the PL emission is governed by spin polarized electrons.

The polarization type is defined by the angular position of the maximum intensity I_{max} of the PL peak: a sinusoidal behavior vs θ is the feature of circular polarization (App. A.2). The phase of the sinusoidal profile ($\pi/4$ or $3\pi/4$) is related to the helicity of the circularly polarized light. In our experimental conditions (excitation by σ^- polarized light) for I_{max} at $\theta = 45°, 225°$ the emitted photons have the same helicity respect to the exciting beam (co-circular photons), while for I_{max} at $\theta = 135°, 315°$ the emitted photons have the opposite helicity (counter-circular photons). We attribute negative ρ to co-circular photons, and positive ρ to counter-circular photons. All the ρ values reported in this work are charaterized by an experimental error lower than 0.5%.

1.2.1 Temperature dependence: energy and spin relaxation

The polarization of the direct emission shows a marked dependence on the temperature. In the following, we discuss the results of the PRPL analysis with the support of Monte Carlo simulations of the polarization of

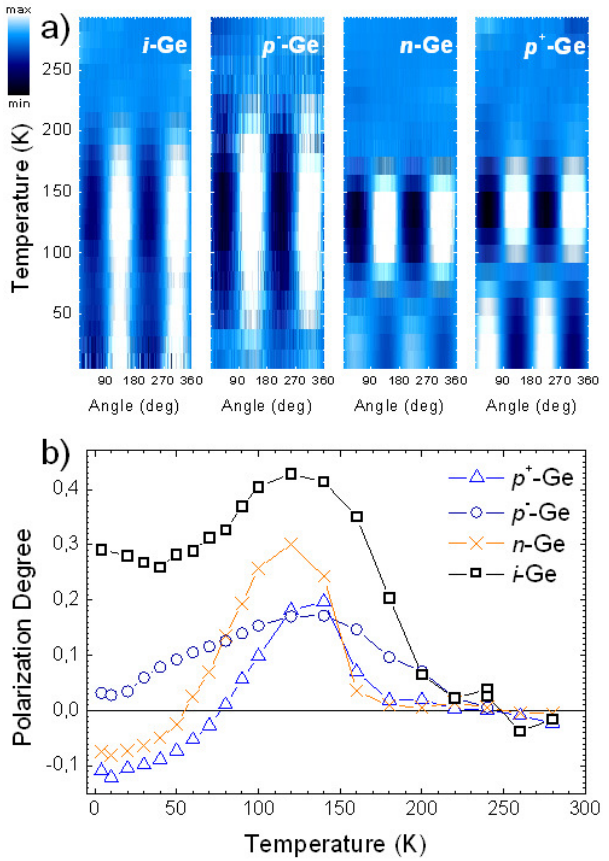

Figure 1.5: a) Colour-coded maps of the modulation of the direct emission peak intensity with θ, depending on temperature, for the four samples of Tab. 1.1. b) Polarization degree of the direct emission obtained by PRPL measurements for all the samples, as a function of temperature.

the direct emission after excitation by circularly polarized light [1].

Figure 1.5a) reports a colour-coded map of the intensity modulation of the direct emission peak vs temperature from 4 K to 300 K, for the samples reported in Tab. 1.1. In Fig. 1.5b) the corresponding polarization degrees (ρ) are shown. The modulation of the peak intensity in Fig. 1.5a) presents the feature of circular polarization (sinusoidal behavior). This is the smoking gun proof of optically oriented electrons (App. A.3).

Two spin-polarized electron populations contribute to the emission polarization [Fig. 1.6a)]. The first one consists of electrons excited from the SO band by the high energy tail of the 1.165 eV laser [2]. Electrons from the SO band are excited to the very bottom of the Γ valley [Fig. 1.6b)], for this reason we will refer to them as 'low-energy' electrons. According to the selection rules [39] this spin population provides a contribution of $\rho = +50\%$ in the $\Gamma \rightarrow \Gamma$ radiative recombination. The second one consists of electrons excited from the HH and LH bands (at the top of the VB). The energy of the intial states of these electrons is 290 meV above the SO, therefore after absorption they populate high energy states in the Γ valley; thus we will term them 'high energy' electrons. According to the selection rules, this second spin population provides a circular ρ of -25%. The balance between 'high energy' and 'low energy' electrons taking part in the $\Gamma \rightarrow \Gamma$ radiative recombination determines ρ of the direct emission.

[1] Monte Carlo simulations were carried out by Professor H. Dery and co-workers at the University of Rochester.

[2] Actually the energy profile of the solid state laser is Gaussian has a finite linewidth, thus there is a finite possibility that electrons are photoexcited from the SO band [38]. Despite the very low number of these electrons, their contribution to the direct emission can be important because they are photoexcited directly at bottom of the Γ valley.

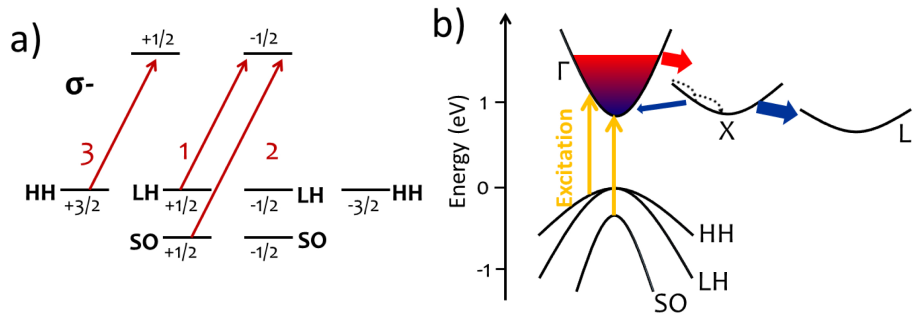

Figure 1.6: a) Γ-point states contributing to spin injection: the VB states are labeled by HH (heavy holes), LH (light holes), and SO (split-off band), and with the projection of the total angular momentum along the direction of the light propagation. Arrows indicates the optical selection rules under σ^- excitation: the relative weight of the matrix element of the dipole allowed transitions are reported. b) Sketch of the Ge band structure and of the photoexcited carrier dynamics before recombination in a doped sample.

Consequently, it can change from -25% (when 'high energy' electrons dominate) to $+50\%$ (when 'low energy' electrons dominate) in absence of spin depolarization.

We now analyze the PRPL results of the direct emission. The polarization degrees at 4 K for all the samples are reported in Figure 1.5b). For $i-$Ge the direct emission is counter-circularly polarized with respect to the excitation with $\rho \sim +30\%$, for the sample p^-−Ge $\rho \sim +5\%$, and for samples $n-$Ge and p^+-Ge the luminescence has the same helicity of the excitation with $\rho \sim -8\%$ and $\rho \sim -11\%$, respectively. $-25\% < \rho < +50\%$ for all the samples, as expected. Since the studied samples differ from each other by the doping, these results suggest that the relative portion of 'high-energy' and 'low-energy' electrons taking part in the luminescence

depends upon the free carrier concentration (Tab. 1.1). In addition, since $n-$Ge and p^+-Ge samples show similar ρ values, free electrons and holes seem to affect the polarization in the same way.

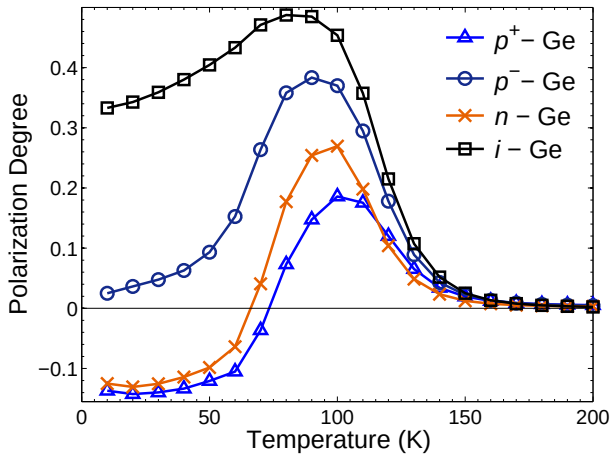

Figure 1.7: Calculated degree of the circular polarization of the direct gap PL of bulk Ge excited with circular σ^- light, obtained by Monte Carlo simulations [38].

Figure 1.7 reports the results of Monte Carlo simulations [38], which fully recover the experimental data shown in Fig. 1.5b). According to these calculations, after excitation to the Γ states 'high-energy' electrons are transferred to the X valleys with a higher probability. Calculations further demonstrate that the dynamics of 'high-energy' electrons in the X states depends on doping. If the free carrier concentration is negligible, the phonon-induced intervalley scattering efficiently transfers electrons to the lower energy L valleys. As a result, the direct emission is mainly dominated by 'low-energy' electrons, providing $\sigma+$ polarization. Thie

mechanism is in agreement with the positive ρ measured in $i-$Ge. On the other hand, for higher doping levels, the Coulomb interaction between photoexcited electrons and extrinsic carriers (background carriers) activates thermalization in the X valleys [Fig. 1.6b)]. Energy relaxation is much more effective in the X states rather than in the Γ valley, due to the similarity of the electron mass to the one of the background carriers. 'High-energy' electrons reaching the bottom of the X valleys are mainly transfered to the L states, but a small part of them can scatter back to the bottom of the Γ valley. Such electrons take part to the radiative recombination, contributing to the polarization of the direct emission. As a result, in the polarization of the doped samples we observe a $\sigma-$ contribution, and the higher the doping level, more negative is ρ [Fig. 1.5b), Fig. 1.7]. Since the thermalization is activated by background carriers, the higher is the doping level, the larger is the contribution of 'high-energy' electrons to the direct emission.

Noteworthy, the effect of doping on electron thermalization accounts for the increase in intensity of the direct emission in the PL spectrum of the highly doped samples (Fig. 1.2 in sec. 1.1), along with the higher electron population due to the increased Fermi level [40].

We now discuss the behavior of the polarization observed at higher temperatures. When the temperature increases the band gap shrinks according to the Varshni's law (Eq. 1.1); consequently the 'low-energy' and 'high-energy' electron populations change, and a change of ρ is expected. Between 4 K and 50 K, however, the band gap shrinks by only $\sim$3 meV, and indeed the experimental findings show an almost constant ρ.

The results reported in Fig. 1.5 show that when the temperature rises above $\sim$50 K, ρ increases in all the samples. The enhancement of ρ is

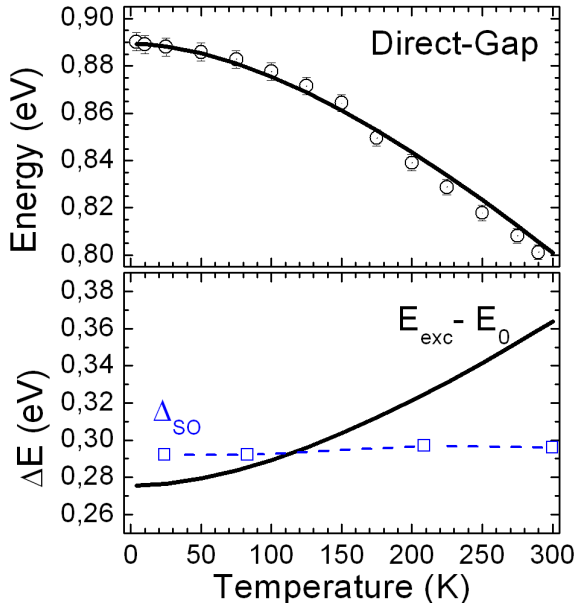

Figure 1.8: Upper panel: energy variation of the direct gap with temperature. Open dots are the PL peak positions measured for $i-$Ge, while the solid line represents Varshni's law [37]. Lower panel: temperature dependence of the excess energy ΔE, for photoexcited carriers in Ge by a 1.165 eV laser (solid black line). The blue squares show the variation of the energy of the SO, Δ_{SO}, with temperature, according to [41]

due to the increasing contribution of the 'low-energy' electrons. The upper panel of Fig. 1.8 reports the temperature dependence of the energy E_0 of the direct $\Gamma \rightarrow \Gamma$ transition in Ge (solid line), and superimposed the measured positions of the direct emission PL peak in sample $i-$Ge. The lower panel reports the resulting temperature dependence of the excess energy $\Delta E = E_{exc} - E_0$, where E_{exc} is the energy of the excitation. When the temperature increases E_0 decreases following the Varshni's law, and thus

ΔE becomes larger. As a consequence, the temperature rise allows us to excite carriers in higher energy states of the bands. Particularly, at $\sim$100 K the excitation becomes resonant with the transition between the top of the SO band and the bottom of the Γ valley in the CB, therefore above this temperature the population of 'low-energy' electrons increases significantly. At the same time the kinetic energy of 'high-energy' electrons increases, and their transfer towards the L side valleys becomes more efficient [42].

At T$\sim$120 K ρ is maximum for all the samples (Fig. 1.5b). Indeed, above this temperature the thermal activation of spin depolarization mechanisms reduces the polarization, as discussed in the following.

Fig. 1.5 shows that for temperatures above $\sim$170 K the direct emission from Ge is no more polarized. The quenching of the circular polarization is due to spin depolarization mechanisms, which shorten the spin relaxation time relative to the carrier lifetime, with a consequent decrease of ρ (Eq. 1.2).

According to the Monte Carlo simulations, the main source of depolarization is the thermal activation of unpolarized electrons from the L valleys, which scatter back to the Γ valley, and eventually recombine radiatively from there [38]. The backscattering of L electrons to Γ states has already been invoked in the literature to explain the increase of the direct gap emission at high temperature in Ge-based systems [43]. This process is characterized by a probability $\sim exp(-\Delta_{\Gamma,L}/k_BT)$, where the barrier height value between the two valleys $\Delta_{\Gamma,L}$ is $\sim$140 meV. At RT, electrons in the L valleys presents a microsecond long lifetime [31], and a spin lifetime of $\sim$0.5 ns [44]. As a consequence, for T$>$170 K electrons in the L valleys are likely to be unpolarized, and their depolarization increases with

the temperature. The increase of both $L \rightarrow \Gamma$ backscattering and electron spin relaxation in the L states accounts for the depolarization of the direct emission observed experimentally in the high T range (Fig. 1.5).

1.2.2 Polarization dependence on the excitation power

In this section we discuss the results of the PRPL study of the direct emission as a function of the excitation power density (D) at T=4 K. We report only the analysis carried out for samples $i-$Ge, $n-$Ge, and p^+-Ge, which provides a sufficiently wide experimental support to outline the underlying physics.

In the following we report the Poincaré sphere instead of the modulation of the peak intensity (App. A.2), to represent the photon polarization. This is an eye-catching graphical method to fully describe the polarization type of light. On the Poincaré sphere the polarization type is represented by a point on the sphere surface: the north pole corresponds to circular σ^+ polarization, the south pole to σ^- polarization, the equator line to linear polarization, and the points on the hemispheres correspond to elliptical polarization. In our study, the Poincaré sphere shows only the polarized component of the detected light to improve the readability of the results. Since in our measurements the excitation is circularly σ^- polarized, when the Stokes analysis (App. A.2) provides a point at the north pole, the emitted light is counter-circular with respect to the excitation ($\rho > 0$). Viceversa, a point at the south pole means that the light emitted by the sample is co-circular with respect to the excitation ($\rho < 0$).

In Fig. 1.9 we report the polarization type (Poincaré spheres) and degree (ρ) obtained for samples $i-$Ge, $n-$Ge, p^+-Ge, when D is varied from

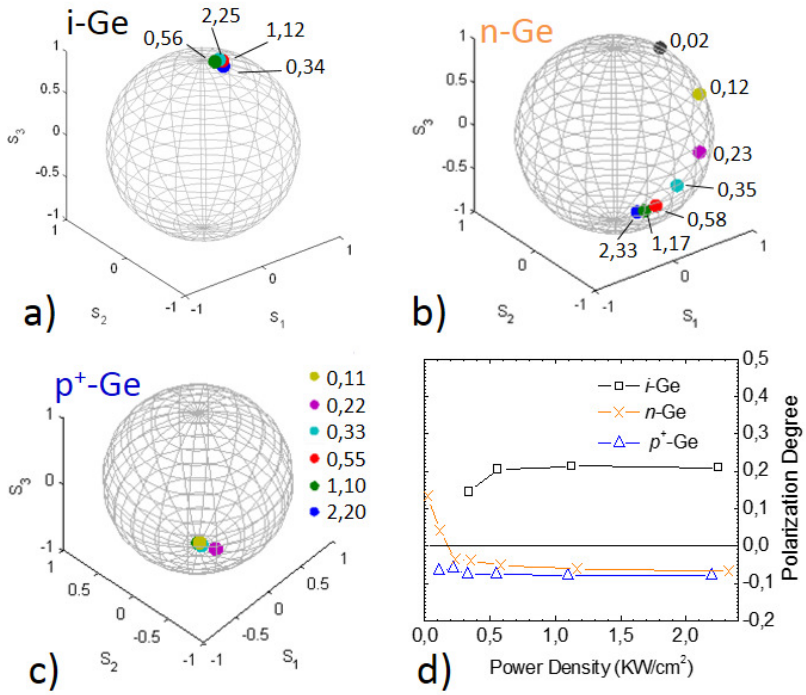

Figure 1.9: Poincaré spheres showing the polarization type of the direct emission for samples a) $i-$Ge, b) $n-$Ge, and c) $p^{+}-$Ge, at T=4 K, as a function of the excitation power density D, under σ^{-} excitation. Data are labeled by D in $\mathrm{kW/cm^2}$ units. d) Polarization degree obtained by the Stokes analysis, as a function of D.

$\sim$2.3 kW/cm^2 to $\sim$0.1 kW/cm^2. When D changes, for samples $i-$Ge and p^+-Ge both polarization type [Fig. 1.9a),c)] and degree [Fig. 1.9d)] are almost constant. On the contrary, for $n-$Ge the polarization shows a stronger dependence on D. In this sample, for 2.33 kW/cm^2 $> D >$ 0.58 kW/cm^2 the polarization of the direct emission is co-circular to the excitation [Fig. 1.9b)] with $\rho \sim -10\%$. Surprisingly, when D is reduced below $\sim$0.5 kW/cm^2 the polarization changes from co-circular ($\rho \sim -5\%$) to counter-circular ($\rho \sim +13\%$), being linearly polarized with almost null ρ at $D \approx 0.2$ kW/cm^2. The change of the polarization type corresponds to the change of position from the south pole to the north pole of the Poincaré sphere.

Taking into account that the co-circular contribution to the polarization is due to 'high energy' electrons, as described in sec. 1.2.1, these results show that the decrease of D affects the weight of 'high energy' electrons in the c$\Gamma \rightarrow$vΓ radiative recombination. Since the 'high energy' electrons can take part in the radiative emission from Γ only after their thermalization in the X valleys, our findings suggest that D affects the efficiency of that process. Similar arguments were discussed in the literature by Zhou et al. in Ref. [45]. [3]

In the previous section we showed that doping supports the thermalization of 'high-energy' electrons. As a result, the doping and the excitation power density D control the number of 'high-energy' electrons taking part into the direct emission.

[3] In Ref. [45] Zhou and co-workers studied the decay curve of the direct gap PL of bulk Ge at T=10 K. The authors observed a fast component of the decay curve characterized by an intensity increasing with D, which is attributed to electrons excited in the high energy states of the Γ valley and thermalized to the band edge.

For sample $i-$Ge [Fig. 1.9a), d)] neither doping nor D are large enough to provide a significant contribution of the 'high-energy' electrons to the direct emission. Consequently, the $\Gamma \rightarrow \Gamma$ emission is dominated by 'low-energy' electrons, yielding constant counter-circular polarization in the $0.34\text{kW/cm}^2 < D < 2.25\text{kW/cm}^2$ range. Sample $n-$Ge lies in a particular window where the doping level is not sufficient to assure an efficient thermalization of the 'high-energy' electrons at low D, but the combined effect of background carriers and high D increases their contribution to the direct emission, resulting in the inversion of helicity of its polarization. Finally, as opposed to sample $i-$Ge, in sample p^+-Ge the high doping level provides a high efficiency of the scattering process. Therefore the direct emission is dominated by the 'high-energy' electrons over the whole D range (0.11-2.2 kW/cm^2), accounting for the constant co-circular polarization.

We carried out the same analysis at higher temperatures, and results are reported in App.App. B. At T=50 K the polarization of all the samples shows the same behavior observed at T=4 K. The only difference is that in sample $n-$Ge the helicity inversion takes place at higher D respect to the 4 K case, because the excitation of 'low energy' electrons is already helped by the temperature (sec. 1.2.1).

At higher temperatures ρ reaches its maximum value [Fig. 1.5b)]. In samples $n-$Ge and $i-$Ge the maximum value is found at T=120 K, and the power dependence shows that at this temperature the variation of D does not affect the polarization. This result highlights that in such conditions 'low energy' electrons dominate the direct emission, suggesting that the maximum ρ value is determined by the sample doping independently on D (at least

in our operating range). At T=160 K ρ is reduced by thermally activated depolarization mechanisms [Fig. 1.5b)], however in samples $i-$Ge and p^+-Ge the decrease of D still provides an enhancement of the polarization degree.

In conclusion, the combination of doping and D allows us to control the polarization type and, partially, the polarization degree of the direct emission from bulk Ge. The two parameters, indeed, affect the fraction of 'high-energy' electrons contributing to the direct emission, which changes the polarization in the way described in sec. 1.2.1. Moreover, the weight of 'high energy' electrons depends on the number of 'low energy' electrons contributing to the direct emission, which is determined by the temperature, providing an effective degree of freedom in the tailoring of the polarization.

1.3 Indirect gap polarized emission

In this section we report the results obtained from the Stokes analysis of the indirect emission in sample $i-$Ge, and a short discussion of the results obtained for $n-$Ge sample.

The spin lifetime and the carrier lifetime of electrons in the L valleys are affected by doping. Since ρ depends on both of these parameters (Eq. 1.2), an analysis of the effects of doping on the polarization of the indirect emission would be non-trivial, and it would require further experimental investigations, beyond the aim of the present thesis. For this reason we focus on the study of $i-$Ge.

Figure 1.10a) shows the polarization type of the emission lines due to phonon-assisted $L \rightarrow \Gamma$ transitions (sec. 1.1) of $i-$Ge (values of ρ are

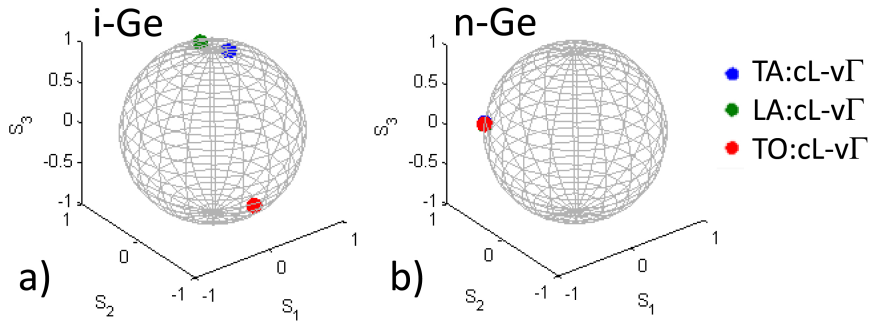

Figure 1.10: Poincaré spheres representing the polarization of the TA, LA, and TO phonon replicas, for samples $i-$Ge (a) and $n-$Ge (b). PRPL measurements were carried out at T=4K, under circular σ^+ excitation.

reported in Tab. 1.3). Measurements were carried out with excitation characterized by σ^+ polarization (opposite helicity with respect to the measurements reported in the previous sections), therefore under this conditions the north (south) pole of the Poincaré sphere corresponds to co-circular (counter-circular) polarization. The Poincaré sphere in Fig. 1.10a) shows that all the PL peaks due to phonon replicas in $i-$Ge are circularly polarized. Despite the small polarization degrees of the indirect emission lines (Tab. 1.3), the detection of a finite polarization from the $L \rightarrow \Gamma$ emission is a surprising result. This is the evidence that the oriented spins withstand not only the $\Gamma \rightarrow L$ transfer, as observed in recent photoemission measurements at RT [46], but also the long stay in the L valley before recombination. According to Eq. 1.2, indeed, $\rho \neq 0$ is the indication that the spin lifetime τ_s of the photoexcited carriers is at least of the same order of magnitude of the carrier lifetime τ. In the literature, $\tau \sim 500\ \mu$s is reported for electrons in

Table 1.3: Polarization degree for the phonon-replicas of the indirect emission for samples $i-$Ge and $n-$Ge, at T=4K.

phonon-replica	ρ for $i-$Ge	ρ for $n-$Ge
TA	- 4%	3%
LA	- 3%	3%
TO	+ 1%	12%

the L valleys in intrinsic Ge at RT [32]. At lower temperatures τ increases, due to the reduction of thermally activated processes providing fast non-radiative recombination. As a result, the detection of circularly polarized emission from the indirect transition indicates that $\tau_s \gtrsim \tau(4\text{K}) > 500\ \mu$s.

In Figure 1.11 we compare our findings with the main results reported in the literature. The solid line is the theoretical prediction of the spin lifetime of electrons in the L valleys taking into account the depolarization effects due to electron-phonon scattering, as a function of the temperature. When the temperature decreases, τ_s is expected to increase slowly from RT to T$\sim$100 K, while below T$\sim$100 K the increase becomes extremely rapid. In Fig. 1.11 we report data obtained by electrical measurements (open symbols) [24, 26, 25, 44, 13], and data from magneto-optical measurements (black circles) [23]. Most of the τ_s values measured in experiments exploiting the electrical spin injection [26, 25, 44, 13] are shorter than 1 ns, below the theoretical prediction over the entire 4 - 300 K range. On the other hand, the most recent electrical measurements (open squares)[24] and the magneto-

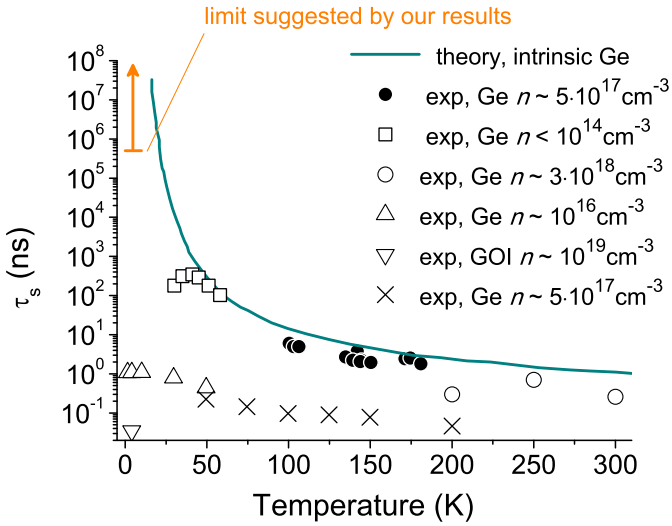

Figure 1.11: Temperature dependence of the spin lifetime of electrons in the *L* valleys of bulk Ge. The blue line is the intrinsic spin lifetime calculated in Ref. [22]. Black circles are data obtained by magneto-optical measuremets in Ref. [23] (*n* is the free carrier density of the sample at RT). All the other data were obtained by electrical measurements reported in Ref. [24] (open squares), Ref. [26] (up triangles), Ref. [25] (down triangle), Ref. [44] (open circles), and Ref. [13] (crosses). The orange arrow indicates the τ_s values suggested by our results for *i*−Ge sample at T=4 K.

optical measurements (black circles) [23] provide τ_s estimations which reproduce the predicted values with great precision. As a result, the comparison shown in Fig. 1.11 suggests that τ_s reported in Ref. [26, 25, 44, 13] is limited by a fast spin relaxation mechanism, independent on the temperature over the studied range. This effect is reasonably due to localized states at the interface between the tunnel barrier and the semiconductor, which mask the spin signal of the itinerant electrons, preventing the measurements of

their intrinsic spin lifetime [47, 25, 48]. Recent works indeed highlight the role of interface defects in the spin depolarization process [44, 49]. In this context our findings, in excellent agreement with the theoretical prediction, constitute the only evidence of the length of the intrinsic spin lifetime of electrons in the L valleys of Ge at T$<$40K, and demonstrate the long-lived electron spins in Ge. As a result, Ge presents τ_s values much longer than in III-V materials, mostly at low temperature [50, 51, 52, 1]. In fact, this study shows competitive aspects of Ge with III-V compounds in the field merging photonics and spintronics. Our results pave the way to the exploitation of the long intrinsic electron spin lifetime of Ge at low temperature, highlighting the importance of the optical means in the spintronic investigation also in IV group semiconductors.

Figure 1.10a) shows that in $i-$Ge the TA and LA phonon replicas are co-circularly polarized with respect to the excitation, while the TO replica is counter-circularly polarized. In Ref. [22] a theoretical model of the polarized emission from bulk Ge, based on the group theory is discussed. Li et al. demonstrate that the selection rules of the angular momentum depend on the phonon assisting the recombination. For each phonon, Li and co-workers calculate the ratio of intensities between the co-circular and the counter-circular components of the indirect emission [53]. Under σ^- excitation Li and co-workers find that $I_{\sigma^-} : I_{\sigma^+}$ =3:1 for the LA, 1:3 for the TO, and 1:0 for the TA assisted transition. As a consequence, the LA and TA phonon replicas would be co-circularly polarized, and the TO phonon replica counter-circularly polarized, in full agreement with our experimental findings.

We now consider the comparison between the polarization of the TA and LA phonon replicas and the one of the direct emission of $i-$Ge. As

shown in sec. 1.2, the polarization of the direct emission is counter-circular with respect to the excitation [Fig. 1.9a)]. TA and LA phonon replicas, instead, are characterized by co-circular polarization [which in Fig. 1.10a) is represented by the north pole of the Poincaré sphere, because the excitation is σ^+ polarized]. As already mentioned, co-circular polarization is provided by 'high-energy' electrons. All these results thus indicate that 'high energy' electrons dominate the population of the *L* valleys, while 'low energy' electrons dominate in the Γ valley, in excellent agreement with the carrier dynamics outlined in sec. 1.2.1.

In Figure 1.10b) we report the polarization type obtained for the indirect emission lines of $n-$Ge. Let us recall that $n-$Ge is doped by As with an impurity concentration $\sim 10^{17} cm^{-3}$. For this sample, all the phonon replicas are characterized by linear polarization, which can be seen as the sum of two circularly polarized components with opposite helicity. Consequently, in $n-$Ge the spin up and spin down populations are balanced with each other in the *L* states. The ρ values estimated by the Stokes analysis are quite high (Tab. 1.3), highlighting the strength of the effect of *n* doping on the polarization of the indirect emission. As a result, these findings confirm the reliability of the results reported for $i-$Ge, despite the small ρ values.

1.4 High energy structures

In Fig. 1.3, sec. 1.1, we reported the PL spectra obtained in the 0.8 - 1.1 eV range for all the samples of Tab. 1.1 at 4 K. Besides the intense direct emission, discussed in sec. 1.2, a further structure can be observed at energy $\sim$1.05 eV, i. e. $\sim$70 meV above the direct emission peak. In sample

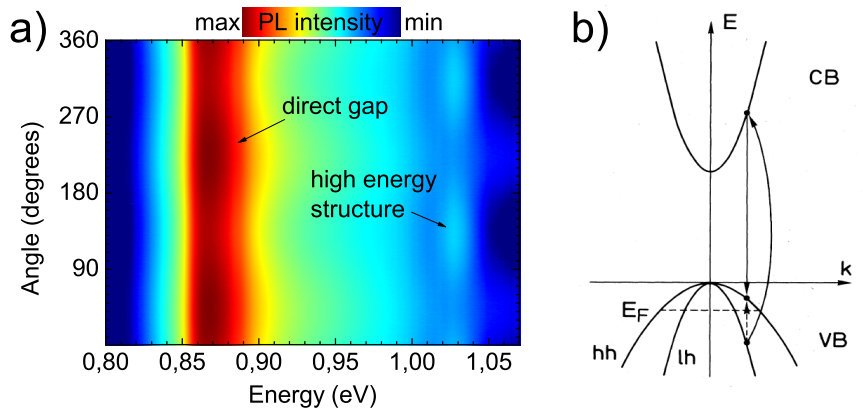

Figure 1.12: a) Colour-coded map of the PL emission from p^+-Ge at 4K, at energies between 0.8 and 1.1eV. b) Sketch of the intervalence-band Raman scattering process as reported in Ref. [54, 55].

p^+-Ge, the intensity of the signal allowed us to perform Stokes analysis. In the following we analyze the polarization of the signal, and provide a comparison with literature data in order to tentatively attribute its origin. The measured intensity modulation vs θ is reported in Fig. 1.12. The peak intensity shows minima at $\theta = 45°, 225°$ and maxima at $\theta = 135°, 315°$, which is the signature of circular polarization with opposite helicity with respect to the σ^- excitation. In the sample $i-$Ge, instead, the low intensity of the signal prevented us to study the polarization, nevertheless the peak position of the structure is almost independent on temperature (Fig. 1.4), which is the same behavior observed for the structure in sample p^+-Ge.

A similar feature has been reported in the literature by Wagner and Cardona in Ref. [54], and by Tanaka et al. in Ref. [55]. Wagner and Cardona studied heavily p-doped Ge, while Tanaka analysed n- and p-doped

Ge with an impurity concentration $< 10^{17} cm^{-3}$. The two papers agree in attributing the structure to intervalence-band Raman scattering. The process is sketched in Fig. 1.12b): a photoexcited electron from the LH band to the CB recombines radiatively reaching a HH state. Since LH and HH states are characterized by different projections of the angular momentum J along the direction of light propagation (App. A.3), the helicity of the emitted photon must be opposite with respect to the one of the absorbed photon. The process involves carriers with $k \neq 0$, therefore the energy of the scattered photon is higher than E_0 and it is almost independent on temperature [55]. The polarization analysis [Fig. 1.12a)] of the emission of p^+-Ge sample is in agreement with the observations reported in the literature, and the independence of the detected features upon temperature allow us to ascribe the $\sim$1.05 eV structure to intervalence-band Raman scattering.

Part II

Ge/SiGe multiple quantum wells

Chapter 2

Spin lifetimes of confined carriers

In this chapter we exploit the PRPL technique to study the spin properties of holes and electrons in Ge quantum wells (QWs), demonstrating optical spin injection in Ge nanostructures. Similarly to the bulk case, in Ge QWs the PL emission from direct and indirect transitions can be detected. Moreover, in QWs strain and confinement effects act on the electronic levels removing the degeneracy between the HH and LH bands at the top of the VB (App. C). Consequently, the emission due to direct recombination on the HH states is separated from the emission due to direct recombination on the LH states in the PL spectrum of the studied heterostructures. The polarization analysis of the different spectral peaks due to direct transitions allowed us to outline the spin dynamics of holes in the VB, while the study of the polarization of the indirect emission provided information on the the spin dynamics of electrons in the *L* valley of the CB.

The undoped and strained QWs exhibit a high degree of spin polarization, yielding large ρ values of circular polarization for both direct gap PL

emissions involving HH and LH states. From the measured polarization degree of these two PL peaks, we evaluate the spin relaxation time of holes showing that HHs are characterized by a fast depolarization (τ_s <0.5 ps), while the spin lifetime of LHs in QWs is longer than 0.5 ps.

Also the indirect gap PL peaks are circularly polarized. As we already discussed in the previous chapter, measuring a non-vanishing circular polarization from the *L* valley luminescence is possible only if $\tau_s \gtrsim \tau_L$ (see Eq. 1.2) (where τ_L is the indirect gap recombination lifetime). Therefore, in order to have high polarization degrees one needs long τ_s and/or short τ_L. In undoped bulk group IV semiconductors and common type-II SiGe heterostructures recombination lifetimes of hundreds of ns and longer are reported [56, 31]. In Ge QWs, instead, τ_L is of the order of a few ns, and τ_s in the ns range is sufficient to provide polarized emission. In sec. 2.3 we demonstrate a wide temperature range at which the condition of $\tau_s \gtrsim \tau_L$ is met.

2.1 PRPL of Ge/SiGe MQWs

PRPL measurements on Ge QWs were carried out at T=4K using the same experimental configuration exploited for the study of bulk Ge discussed in chapter 1. The σ^- polarized 1.165 eV laser was focused to a spot size having a $\sim$100 μm diameter, resulting in an excitation power density in the range of 0.9 - 3kW/cm^2. The emitted light was probed by an InGaAs detector with cutoff energy 0.75 eV.

We analyzed a Ge/$Si_{0.15}Ge_{0.85}$ multiple quantum well (MQW) grown on a graded buffer layer [57] (App. C). The active region consists of 100 peri-

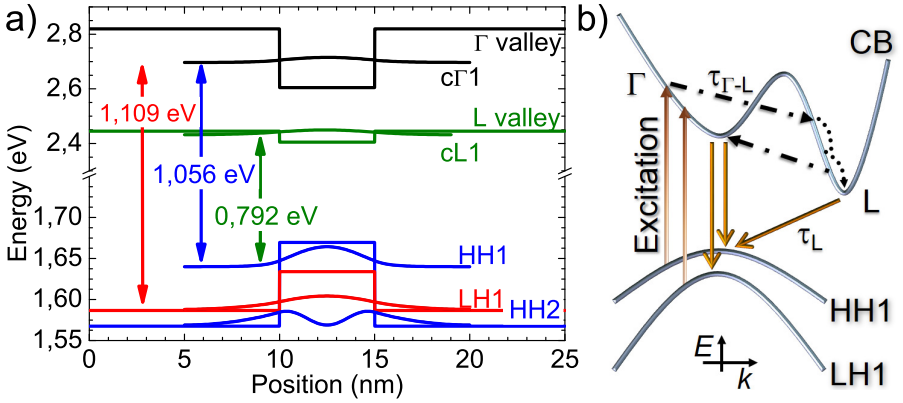

Figure 2.1: a) Result of the 8-band $\mathbf{k}\cdot\mathbf{p}$ calculation of energy levels and wavefunction squared amplitudes for a $Si_{0.15}Ge_{0.85}$/Ge/$Si_{0.15}Ge_{0.85}$ quantum well. b) Sketch of the luminescence process. Immediately after direct gap excitation, electrons can thermalize towards the edge of the Γ valley and recombine radiatively. For Γ valley electrons, however, the most effective relaxation process is the scattering to the low-energy L valleys, which lasts $\tau_{\Gamma-L} < 1$ps. Electrons in the L valleys can recombine radiatively with a characteristic time τ_L.

ods of strain compensated 5 nm wide Ge QWs and 10 nm thick $Si_{0.15}Ge_{0.85}$ barriers. The main peculiarity of this structure is the type I alignment of both the direct and the indirect gap (Fig. 2.1a) [58]. Thanks to this characteristic, the Ge layers show a *quasi*-direct gap optical behavior [59], ensuring a good absorption efficiency. The energy levels of the confined states were calculated using an 8-band $\mathbf{k}\cdot\mathbf{p}$ model [60, 61]. Figure 2.1a) shows the energies obtained along the growth direction, and the squared amplitude of the corresponding electronic wavefunctions. The confined states are labeled by the quantum number n. In the valence band HHn and LHn refer to heavy and light-hole states at the Γ point, respectively. cΓn and cLn indicate the

conduction states at the Γ and the *L* points, respectively. The transition energies between confined states are also reported. $\mathbf{k}\cdot\mathbf{p}$ calculations were carried out assuming the nominal thickness of the QWs.

Using a 1.165 eV laser the carrier excitation is almost resonant with the direct gap transition in the Ge layers [Fig. 2.1a)] [62], and electrons are photoexcited to the Γ valley of the QWs. As already mentioned, in Ge QWs biaxial compressive strain and confinement remove the degeneracy between HH and LH at the Brillouin zone center. The top of the valence band is thus HH-like, and the weight of photoexcited electrons from HH and LH bands changes with respect to the bulk case [63]. Discussing the PRPL study of bulk Ge (chapter 1) we used the term 'high energy' to indicate the electrons excited from both the HH and the LH bands; in the following we will distinguish them, and outline the spin dynamics originating from the separation of these two bands. Strain and confinement act also on the SO band, so that in Ge QWs the energy of the trasition between the SO band and the Γ states in CB is much larger than the excitation energy, therefore 'low energy' electrons can not be photoexcited in these nanostructures.

Figure 2.1b) illustrates the physical processes taking place under our experimental conditions. The relaxation processes of the photoexcited electrons in Ge QWs are the same described in chapter 1 for bulk Ge, except for the ones concerning the *X* states. The cX-vΓ gap, actually, is characterized by a type II alignement [61], thus electrons in the *X* states of the CB are not confined into the Ge layer. Photocreated electrons in the Γ valley of the QWs are scattered to *L* valleys on a sub-picosecond timescale ($\tau_{\Gamma-L} \approx 0.5$ps) [20, 64, 43]. In this short time, few electrons can recombine radiatively from the Γ states of the CB with holes in the HH or LH states

of the VB. Assuming a time constant of $\tau_{\Gamma,r} \sim$ 1ns for direct gap radiative recombination [65, 66, 67], we can estimate that during the ultrashort dwell time of photoexcited electrons in the Γ valley about $\tau_{\Gamma-L}/\tau_{\Gamma,r} \sim 10^{-3}$ of their population experience radiative recombination rather than ultrafast transfer to the L valleys. The lifetime of electrons in the L valleys (τ_L) is governed by radiative and non-radiative recombination processes, and it is in the order of a few ns, depending on the QW thickness [68].

2.2 Direct gap emission: hole spin lifetime

Figure 2.2a) shows a contour plot of the PL intensity at T=4 K following σ^- excitation as a function of the rotation angle of the polarization analyzer. The lower panel shows the resulting PL spectra at θ=135° (pure σ^+, counter-circular component) and θ=45° (pure σ^-, co-circular component).

The measured emission peaks can be rationalized by tight-binding [59] or $\mathbf{k}\cdot\mathbf{p}$ calculations [summarized in Fig. 2.1a)]. The spectral feature around $\sim$1.02 eV is due to the cΓ1-HH1 transition and the feature at $\sim$1.07 eV is attributed to the cΓ1-LH1 excitonic recombination. The second one is superimposed onto the broad high energy tail of the main cΓ1-HH1 peak. The low-energy PL doublet, at $\sim$0.8 eV, is associated to transitions across the indirect band-gap: the high energy part is ascribed to the no-phonon (NP) emission due to the cL1-HH1 recombination of confined carriers, while the low energy part of the doublet is the longitudinal acoustic (LA) phonon-assisted optical transition [59].

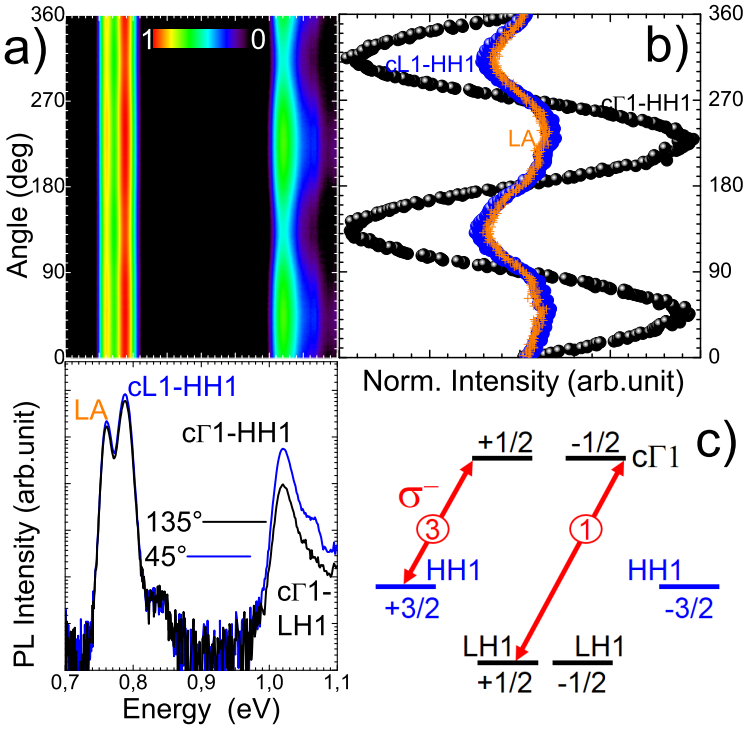

Figure 2.2: a) Colour-coded contour plot of the PL intensity vs the analyzer angle for the Ge/$Si_{0.15}Ge_{0.85}$ MQW sample at 4 K and under σ^- circularly polarized excitation. In the lower panel: spectra resolved for analyzer angles of 135° (black line) and 45° (blue line). Their intensity difference indicates the peak polarization. b) Modulation of the normalized peak intensity of the cΓ1-HH1, cL1-HH1 and phonon replica emissions. c) Optical selection rules of the σ^- excitation. Dipole allowed transitions of HH ($m_j = 3/2$) are three times larger than of LH ($m_j = 1/2$) at Γ. The HH and LH energy levels are split by confinement and strain.

Figure 2.2b) shows the intensity modulation of the PL due to the cΓ1-HH1 transition (black dots), to the NP cL1-HH1 transition (blue dots) and to the phonon replica (orange crosses) of the cL1-HH1 transition. This figure reveals a sinusoidal behavior with period π, characteristic of circularly polarized emission with the same helicity of the excitation. Such observation is corroborated by the Stokes analysis (App. A.2), yielding a polarization degree $\rho \sim -37\%$ for the cΓ1-HH1 PL peak. This polarization is characterized by opposite helicity and larger ρ with respect to the polarization measured for the direct emission of intrinsic bulk Ge, at the same temperature (chapter 1). The change of circularity and the enhancement of polarization degree gained in the PL of the QWs is due to the separation of the HH and LH bands, and to the increase of the transition energies, which prevents the photoexcitation of electrons from the SO states (sec. 2.1). These conditions increase the weight of electrons photoexcited from the HH states during the absorption process with respect to the bulk case. Under σ^- excitation, electrons from the HH states populate the cΓ1(+1/2) state in the CB [Fig. 2.2c)], providing a large contribution of the cΓ1(+1/2)→HH1(+3/2) recombination channel, which ensures the dominance of the co-circular component of the polarization in the cΓ1-HH1 emission.

The polarization analysis of the direct gap emission sheds light on the spin relaxation of holes. In our excitation conditions, electrons are injected to cΓ1(+1/2) conduction states starting from HH1(+3/2) states, as well as to cΓ1(-1/2) conduction states starting from LH1(+1/2) states [Fig 2.2c)]. Only the HH1-cΓ1 and the LH1-cΓ1 transitions are indeed activated. According to theoretical predictions for Ge QWs [63] and III-V

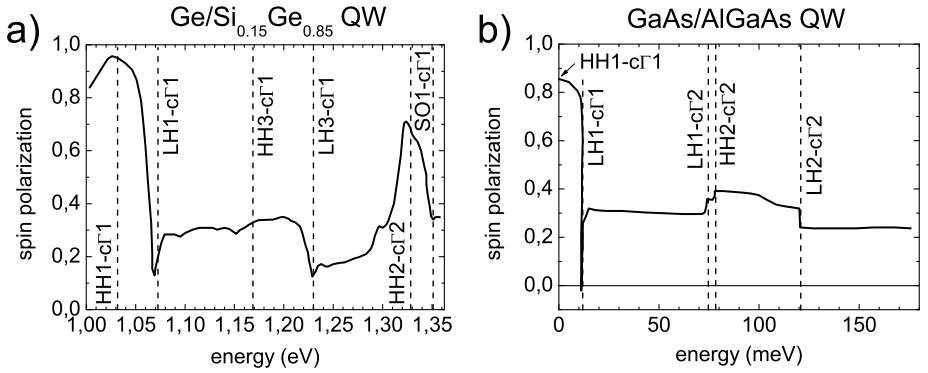

Figure 2.3: Spin polarization of the conduction electrons optically excited by σ^+ polarized light obtained as a function of the excitation energy a) by tight binding calculations for a 48 monoatomic layers ($\sim$10 nm wide) $Ge/Si_{0.15}Ge_{0.85}$ QW in Ref. [63], and b) by $\mathbf{k}\cdot\mathbf{p}$ calculations for a 12 nm wide undoped GaAs/AlGaAs QW in Ref. [69]. In panel b) zero energy is set at the HH1-cΓ1 transition energy. The threshold energies for the relevant interband transitions are indicated by vertical labels. Results in panel a) (b) take (do not take) into account excitonic effects.

QWs [69], shown in Fig. 2.3, the overall electron polarization right after injection is expected to be $P_S \approx$28-34% for excitation energy just above the LH1-cΓ1 transition[1]. Since the calculations were carried out assuming σ^+ excitation, in our experimental conditions P_S has to be considered with negative sign. Under the assumption of complete heavy holes depolarization, electrons can recombine with either HH1(+3/2) or HH1(-3/2) holes emitting

[1]The 3:1 ratio between the oscillator strengths of the HH1-cΓ1 and of the LH1-cΓ1 transitions reported in Fig 2.2c) is valid only exactly at the Γ point. If $k \neq 0$ states are involved in the absorption process, the spin polarization of the photoexcited electrons right after injection is determined not only by the transition probability, but also by the joint density of states of the dipole allowed transitions [70].

co-circular or counter-circular polarized light, respectively. Now, if electron spin depolarization was negligible, the circular polarization degree for the cΓ1-HH1 emission would be $\rho \approx 0.96 \cdot P_S$, according to Ref. [63]. The consistency of this conclusion with our experimental finding of -37% validates the presence of equal numbers of heavy holes in the two sublevels, despite the fact that only HH1(+3/2) holes are created upon σ^- excitation [Fig. 2.2c)]. Most importantly, the mechanisms leading to equalization of the HH1(+3/2) and HH1(-3/2) populations take place on a timescale τ_{hh} faster than that of the electron scattering to L valleys ($\tau_{\Gamma-L} \approx 0.5$ ps, as already mentioned).

In order to understand the spin dynamics of holes we analyze the polarization of the cΓ1-LH1 PL emission [at $\sim$1.07 eV in Fig. 2.2a)]. Since this feature is superimposed to the high energy tail of the cΓ1-HH1 peak, we can estimate its polarization degree by subtracting the exponential Boltzmann-like tail of the cΓ1-HH1 transition from the spectra obtained at analyzer angles of 45° and 135° [71]. By doing so, we obtain a co-circular polarization as high as $-85\% \pm 17\%$ at this spectral region. This large measured value indicates that photoexcited light holes LH1(+1/2) do not lose their spin orientation within 0.5 ps. Holes in the LH1(+1/2) state can either recombine radiatively with cΓ1(-1/2) electrons or relax into lower energy HH1(-3/2) states via parity-preserving scattering events [69]. This relaxation process counterbalances the population of photoexcited holes in HH1(+3/2) states, providing the overall spin depolarization of the heavy holes. The higher energy of the confined LH band inhibits inward scattering from HH, and the consequent spin relaxation of LHs. From the large measured ρ of the cΓ1-LH1 emission we infer that the depolarization process of LHs (τ_{lh}) in

this structure is longer than $\tau_{\Gamma-L}$.

A study of the hole spin dynamics in similar systems have been reported by Lange et al. [72]. Lange and co-workers performed pump and probe measurements at T= 10 K, and obtained for heavy holes a spin relaxation time in the picosecond range, which is in agreement with our results. Besides this, our finding of τ_{lh} >0.5 ps suggests that the depolarization of LHs in Ge QWs is slower than the spin relaxation observed for holes in bulk Ge [20, 21]. This result compares well with the reduced mixing of the spin states in the nanostructures after the removal of the degeneracy of HH and LH states at Γ, claimed in Ref. [72] to explain the long τ_{hh}.

2.3 Indirect gap emission: spin lifetime of L valley electrons

At lower energies respect to the direct emission, the PL spectrum of Ge QWs displays the features of the indirect emission (lower panel of Fig. 2.2a): the no-phonon (NP) cL1-HH1 peak at ∼0.79 eV and the LA phonon-assisted replica at ∼0.76 eV. The Stokes analysis of the PL intensity modulation of the cL1-HH1 peaks shows that the polarized component of the indirect transitions at 4 K has a nearly complete σ^- character, as shown by Fig. 2.4a). The NP peak reveals a polarization degree of about -8%, and similarly the LA peak displays $\sim -6\%$. In sec. 1.3 we discussed the behavior of the polarization of phonon-assisted transitions in intrinsic bulk Ge, and reported the calculated ratio of intensities between left and right handed circularly polarized PL for each phonon-mediated transition [53], that we summarize here: $I_{\sigma^-} : I_{\sigma_+} = 3 : 1$ for LA phonon replica, 1:3 for TO

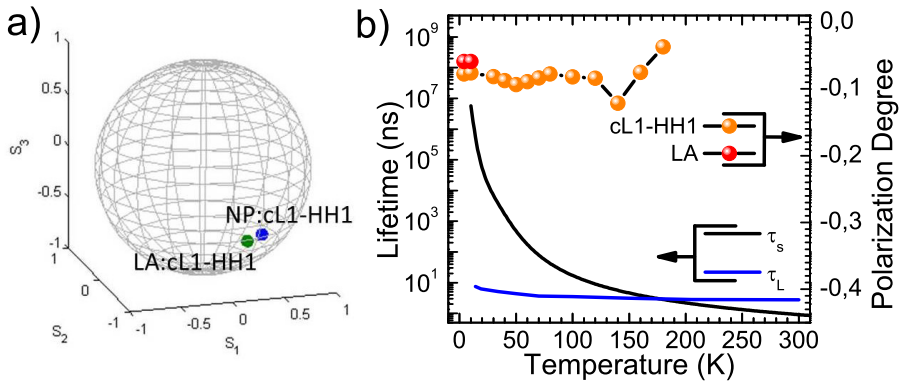

Figure 2.4: a) Poincaré sphere of the cL1-HH1 NP emission and its LA-phonon replica. b) *dots*: Measured temperature dependence of the circular ρ at the PL peak of the NP cL1-HH1 emission (orange dots). Results of the LA phonon-assisted emission (red dots) are shown at T<20 K where it is well resolved from the cL1-HH1 NP peak. *Black line*: Modeled temperature dependence of the electron spin lifetime due to electron-phonon interaction [22]. *Blue line*: Measured recombination lifetime in a ∼5 nm wide Ge/SiGe QW (after [68]).

phonon replica, and 1:0 for the TA phonon replica (assuming σ^- excitation). The helicity of the LA-phonon replica obtained in our measurements agrees with the theoretical prediction and the observations on bulk Ge. Moreover, the slight difference in measured polarization degrees of the NP ($\sim -8\%$) and LA replica ($\sim -6\%$) can be explained by the proximity of the weak TA transition to the NP emission region and of the weak TO transition to the LA region.

We now focus on the degree of polarization. We mentioned above that the initial electron polarization at the Γ valley is $P_S \approx -30\%$. The energy proximity of the Γ and the L valleys ($\Delta_{\Gamma-L}$ ∼250 meV, Fig. 2.1a) and the ultrafast transfer between the two are key features in keeping the

photoexcited electrons spin-polarized when reaching the L valleys. After these considerations, and taking into account the predicted LA intensity $I^{LA}_{\sigma^-}/I^{LA}_{\sigma_+} = 3$ one should expect at most $\rho_0 \approx -15\%$ for the cL1-HH1 emission. The smaller measured average value ($\sim -6\%$) can be attributed to two spin-relaxation mechanisms. The first is due to electron-hole exchange interaction of confined exciton states. This mechanism plays an important role at liquid-helium temperature and in intrinsic QWs [73]. The second relaxation process is attributed to the Elliott-Yafet mechanism via intervalley electron scattering by shortwave phonon modes [74, 8]. As explained below, this mechanism pertains to higher temperatures.

To extract the spin relaxation of electrons, we performed a Stokes analysis of both NP and LA emissions as a function of the lattice temperature (App. A.2). Figure 2.4b) shows that below 150 K the measured polarization of the indirect band-gap luminescence in Ge/SiGe MQWs is nearly temperature independent. [2] This observation is a clear indication that the optically oriented spins withstand the ultrafast transfer to the L valleys and the dwell time of electrons in the L valleys before recombination. Recent PL decay measurements of the indirect recombination provided the lifetime of electrons in the L valleys of similar Ge QWs, as a function of the QW thickness [68]. We estimate the electron lifetime, τ_L, in 5 nm QWs by the interpolation of the data of samples with 3.8 nm and 7.3 nm QWs. As shown by the blue curve of Fig. 2.4b), the resulting τ_L is $\sim$8 ns across the whole temperature range (14 - 300 K).

[2] By increasing the temperature the band gap shrinks and above 150 K the indirect gap emission starts to leak out of the spectral range of our apparatus, preventing any significant conclusion.

The spin relaxation analysis reported in Ref.[22] helps us to complete the picture. Li et al. studied the effect of electron-phonon scattering on the spin depolarization in intrinsic Ge [22]. In Fig. 2.4b), the sharply decreasing (black) curve shows the resulting spin relaxation time. Around 150 K, $\tau_s \approx$5 ns is comparable with the recombination lifetime τ_L. Taking into account the dependence of the circular polarization on these timescales, $\rho = \rho_0/(1+\tau_L/\tau_s)$ (Eq. 1.2), we can explain the decrease of the measured circular polarization above T=150 K. The theory shows that spin relaxation is governed by *intervalley* electron-phonon scattering in a wide temperature range (T>30 K) [19]. This dominating mechanism involves shortwave phonon modes whose wavevector connects centers of different *L* valleys (i.e., phonon modes near the *X* point). Dominant contributions result from phonons characterized by ≈30 meV energy [22]. The temperature dependence of this spin relaxation mechanism is governed by the Bose-Einstein distribution of these phonon modes. At T $<$ 20 K the population of *X* point phonon modes is negligible and, as a result, the *intravalley* spin relaxation rate exceeds the *intervalley* rate [22]. Our experimental findings demonstrate that τ_s has to be longer or at least in the order of 5 ns far below T = 150 K. This calls for a direct experimental measurement in pure Ge QWs in the low temperature regime, which will be addressed in chapter 4 by Electron Spin Resonance.

Chapter 3

Tailoring the optical spin polarization

In this chapter we describe a way to tune the optical spin polarization of photoexcited electrons in the CB of strain compensated Ge/SiGe MQWs. We performed PRPL measurements on samples characterized by the same barrier and QW composition, but with different layer thickness. Since confinement affects the energy of the electronic levels, using a fixed energy laser excitation we could get control on the activation of different transitions changing the QW width. Particularly, we could either excite electrons only from HH states, or from both HH and LH states.

The spin polarization of electrons in the CB is determined by the initial states in the VB, whose contribution depends on the selection rules of the angular momentum [Fig. 2.2c)] and on the joint density of the excited states (as shown in Fig. 2.3). The activation of the absorption from the LH subband has a strong influence on the electron spin distribution, depending on the

energy distance between the excitation and the LH excitonic absorption [63]. Our results demonstrate that when the excitation is almost resonant with the transitions from HH or LH subbands the resulting polarization of the cΓ1-HH1 emission is co-circular or counter-circular, respectively. Consequently, tuning the transition energies with respect to the excitation allows us to control the helicity of the polarization of the cΓ1-HH1 emission. The inversion of helicity after excitation from LH states has been already observed in III-V bulk materials and QWs [75, 76, 77], but it is not predicted in Ge QWs [63].

In the case of selective excitation from HH, the cΓ1-HH1 emission is characterized by $\rho \sim -70\%$. This high polarization degree is found to be independent of excitation power density (D) and temperature below T=50 K, indicating a good fidelity of the spin orientation.

Furthermore, the study of the PL polarization vs temperature shows that thermally activated depolarization mechanisms are effective in reducing the polarization degree approaching RT. The PRPL measurements carried out as a function of D reveal the importance of spin relaxation mechanisms related to the carrier concentration.

3.1 Structural and optical properties

We studied a stack of 200 Ge/$Si_{0.34}Ge_{0.66}$ quantum wells, grown on a relaxed graded buffer layer, whose final composition is $Si_{0.2}Ge_{0.8}$ (App. C). Since the growth rate is actually non-uniform across the 4 inches wafer [59], various samples with equal composition but different thickness are available from a single growth run. The layer thicknesses and the Ge content of QWs

Table 3.1: Structural parameters of the analysed samples, obtained by high-resolution X-ray diffraction measurements.

Sample	well thickness (nm)	Ge content in well	Ge content in barrier
7977-10	$\sim$7	1	0.66$\pm$0.01
7977-8	$\sim$14	1	0.66$\pm$0.01
7977-4	$\sim$19	1	0.66$\pm$0.01

and barriers of the analyzed samples were determined by high resolution X-ray diffraction [1, 2], and are reported in Table 3.1. As shown in Fig. 3.1c), Transmission Electron Microscopy (TEM) images [2] of the samples evidence the high structural quality.

Figure 3.1a) reports the results of the calculation of the electronic structure of a 20nm-wide Ge/$Si_{0.34}Ge_{0.66}$ QW, carried out with an 8-band $\mathbf{k}\cdot\mathbf{p}$ model [61, 60]. Despite the lower Ge content in the barriers, the band alignment is the same as the one reported in the previous chapter for Ge/$Si_{0.15}Ge_{0.85}$ QWs [Fig. 2.1a)]. The direct gap and the fundamental indirect gap are characterized by type I alignement, so that electrons in both the Γ and L valleys of the CB are confined in the QWs. The energy profile of the X states, in contrast, makes electrons reside in the barriers rather than in the QW layers.

[1] Work done by the group of doctor G. Isella at the L-NESS Center of Como (Italy)

[2] Work done by doctor C. Deneke and co-workers at the Laboratório Nacional de Nanotecnologia of Campinas (Brazil)

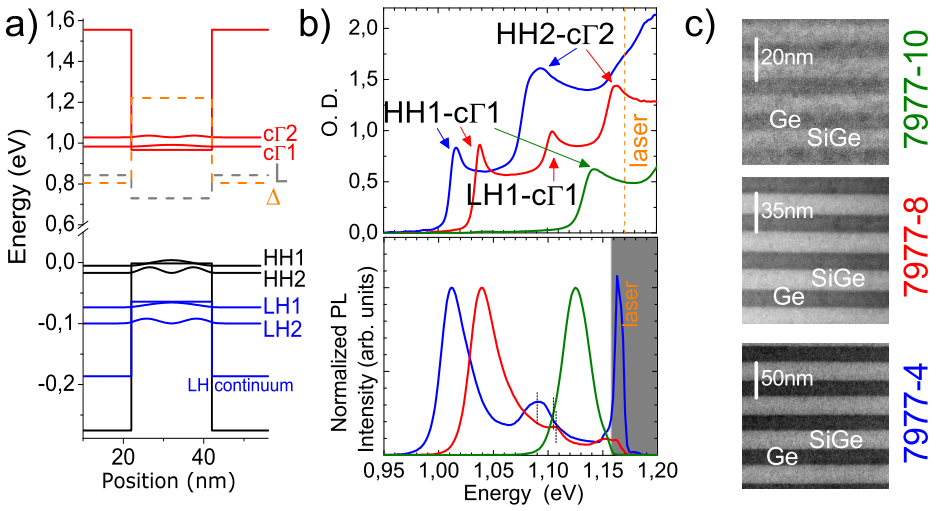

Figure 3.1: a) Band alignement, electronic levels and squared amplitudes of the electron wavefunctions of the first two confined states in a 20 nm-wide Ge/$Si_{0.34}Ge_{0.66}$ QW. Calculations were carried out with an 8-band $\mathbf{k}\cdot\mathbf{p}$ model [61, 60]. b) absorption spectra at T=5 K (upper panel) and PL spectra at T=4 K (lower panel) of sample 7977-10 (green), 7977-8 (red), and 7977-4 (blue). The dashed line in the upper panel indicates the excitation energy for the PL measurements. c) TEM images of the three samples.

In the upper panel of Fig. 3.1b) we report the low temperature absorption spectra for all the samples. The attribution of the excitonic peaks to the dipole-allowed transitions is done on the basis of the results of the $\mathbf{k}\cdot\mathbf{p}$ calculations. The spectra are dominated by the direct excitonic transitions from HH and LH states in the VB to the Γ states of the CB [59]. From these spectra we know which HH and LH states are excited in a PL experiment, after absorption of 1.165 eV light. From now on, we will refer to the energy distance between a transition and the excitation as excess energy.

In the lower panel of Fig. 3.1b) we report the PL spectra measured at T=4 K. In all the spectra, the most intense peak is the cΓ1-HH1 excitonic recombination. The identification of the structures is done through the comparison of the PL with the absorption spectra in the upper panel.

3.2 Polarization of the cΓn-HHn emissions vs QW thickness: tailoring the optical spin polarization

We analyzed the polarization of the cΓn-HHn PL peaks by PRPL measurements, carried out with the same experimental setup and configuration used for the study reported in the previous chapter (described in App. A.1).

In Fig. 3.2 we show the data obtained at T=4 K for the three samples. On the left side of the figure, the colour-coded contour-plots of the PL spectra vs analyzer angle, along with the PL spectrum at $\theta = 0^\circ$ (white line) for each sample are reported. On the right-hand side, the intensity modulation of the cΓ1-HH1 and cΓ2-HH2 PL peaks is given.

In Fig. 3.2a), the cΓ1-HH1 excitonic peak of sample 7977-10 (at 1.125 eV) exhibits co-circular polarization with respect to the excitation. The absorption spectrum in Fig. 3.1b) shows that the HH1-cΓ1 absorption peak has just ∼40 meV excess energy, and only the HH1-cΓ1 excitonic transition is activated by the laser light. After excitation by σ^- polarized light, electrons excited from the HH1 subband populate the cΓ1(+1/2) state [Fig. 2.2c)], providing co-circular emission if the spin relaxation is slow enough to preserve the oriented spins during the recombination process.

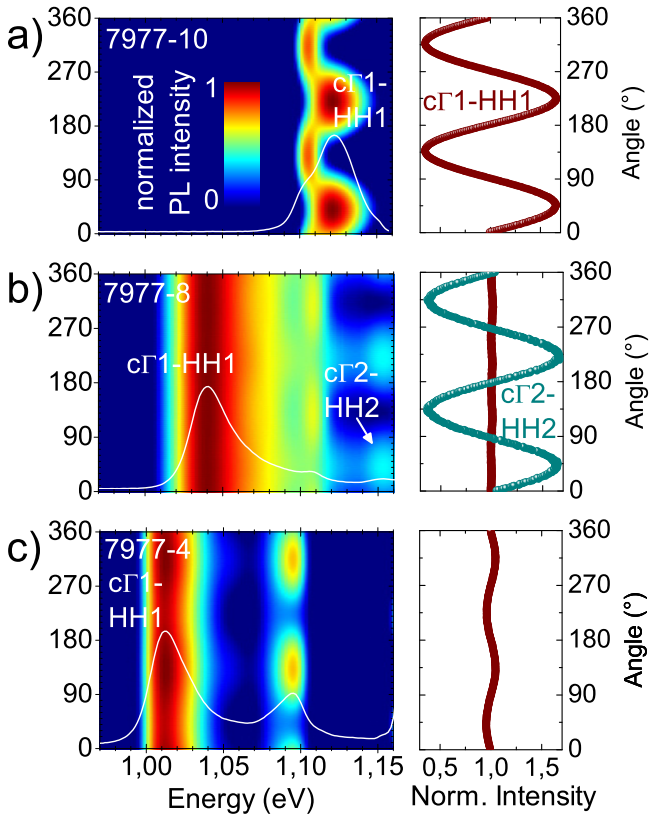

Figure 3.2: a) Left panel: colour-coded contour-plot of the PL spectra of sample 7977-10 vs angle (App. A.2); the PL spectrum at T=4 K and $\theta = 0^\circ$ (white line) is superimposed to the contour-plot. Right panel: modulation of the peak intensity of the cΓ1-HH1 emission normalized to its mean value. Panels b) and c) report the same data for samples 7977-8 and 7977-4, respectively.

Fig. 2.3a) of the previous chapter shows that, for similar systems, the selective excitation of HH states in the VB provides high electron spin polarization right after the absorption. In sample 7977-10, the cΓ1-HH1 emission is characterized by a high polarization degree ($\rho \sim -70\%$) which reflects the almost resonant condition, and indicates as well that the depolarization is negligible.

It should be noted that the polarization analysis highlights the presence of a weaker feature at 1.105 eV. This structure, present at similar energy in all samples, is characterized by counter-circular polarization and its energy position is almost temperature independent [as shown in Fig. 3.3a), b),c) of the following section]. Moreover, its excess energy ($\sim$60 meV) compares well with the energy distance between the HH1 and the LH1 electronic levels [Fig. 3.1a)]. All these considerations allow us to attribute it to electronic Raman scattering (ERS) [78], observed also in bulk Ge, and already discussed in this thesis in sec. 1.4.

In sample 7977-8 the larger QW thickness, with respect to sample 7977-10, causes lower confinement energies. Fig. 3.1b) shows that under 1.165 eV excitation (dashed line) the LH1-cΓ1 and HH2-cΓ2 transitions are activated, in addition to the HH1-cΓ1 transition. Plots of the intensity modulation of the cΓ1-HH1 and the cΓ2-HH2 PL peaks are shown in Fig. 3.2b). In the case of the HH2-cΓ2 transition (1.153 eV), the excess energy of the excitation is comparable with the excess energy of the HH1-cΓ1 transition in sample 7977-10. As a consequence, only electrons from the HH2 states populate the cΓ2 level, resulting in the co-circular polarization and the high ρ ($\sim -68\%$) of the cΓ2-HH2 PL emission. On the other hand, electrons taking part in the cΓ1-HH1 PL emission (1.040 eV) are excited from the

HH1 and the LH1 subbands, so that both cΓ1(+1/2) and cΓ1(-1/2) states are populated, and two components with opposite polarization [Fig. 2.2c)] contribute to the radiative emission. The measured polarization is almost zero, and this evidences a balance between the co-circular and the counter-circular contributions. Such a small polarization degree is only possible if the +3/2 and the -3/2 HH1 states are almost equally occupied. This fact indicates a ultrafast depolarization of the heavy holes, in agreement with the results reported in sec. 2.2 on similar structures.

In sample 7977-4 the confinement energies are further reduced due to the larger QW width, and the weight of carriers coming from the LH1 subband increases. The cΓ1-HH1 PL peak in Fig. 3.2c) (1.012 eV) shows counter-circular polarization, with low ρ value ($\sim +8\%$), highlighting the dominance of the cΓ1$(-1/2)\rightarrow$HH1$(-3/2)$ recombination channel over the cΓ1(+1/2)$\rightarrow$HH1(+3/2) channel. Similarly to the case of sample 7977-8, this result and the excitation conditions [Fig. 3.1b)] make it reasonable to assume complete heavy hole depolarization. As a consequence, the counter-circular polarization is accounted for by the electron spin orientation. This result thus demonstrates that in sample 7977-4 the spin orientation of the photoexcited electrons is opposite respect to the spin polarization reported so far in the QWs analyzed in this chapter and in the previous one.

The change of the electron spin polarization above the LH threshold has been already observed in III-V QWs [77], where it has been attributed to the warping of the LH band [79], which can provide a larger joint density of states for the LH1-cΓ1 transition. In Ge/$Si_{0.15}Ge_{0.85}$ QWs the presence of a band warping is still debated, since expected data are not available and theory predicts it or not according to the parametrization used

in the tight-binding calculation of the band structure [63, 80]. Although we cannot completely rule out that mechanisms such as excitation from the LH continuum can play any role, the benchmark of our findings against III-V literature data favours the hypothesis of a warping of the LH subband. In our experimental conditions, the transition between the continuum of the LHs and the cΓ1 level is almost resonant with the excitation [Fig. 3.1a)], therefore electrons excited from those VB states are generated very close to the band edge of the first confined level in the Γ valley. These electrons can immediately bind with confined holes and recombine radiatively, without need of energy relaxation. For this reason, even though their numbers are low, this mechanism can potentially contribute a lot to the PL signal. In order to avoid excitation from the LH continuum a lowerexcitation energy and a larger band offset, i.e. lower Ge content in the barriers would be needed. Finally, for sample 7977-4, we note that the analysis of the polarization of the cΓ2-HH2 emission (at about 1.1 eV) is prevented by the close energy proximity to the electron Raman scattering (ERS) signal.

3.3 Temperature dependence of the direct emission polarization

In this section we discuss the effects of the temperature on the polarization of the cΓ1-HH1 and cΓ2-HH2 emission lines. Figure 3.3a), b), c) report the contour plots of the PL spectra as a function of the temperature for the three samples in the 4 - 300 K range. The dependece of the peak energies of the PL structures as a function of the temperature allow us to clearly distinguish the PL emissions due to interband transitions from the ERS

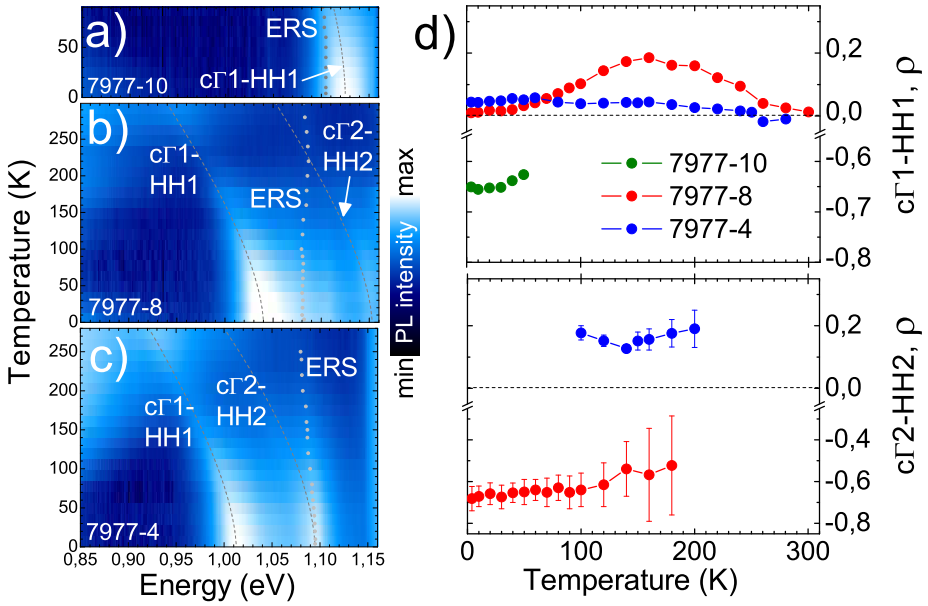

Figure 3.3: a), b), c) Colour-coded contour-plots of the PL spectra vs temperature for samples 7977-10, 7977-8, and 7977-4 respectively (Spectra are reported in App. D). The dashed lines are the values of the peak energy for the transitions between confined states, calculated using the Varshni's law (Eq. 1.1). The gray dots indicate the peak positions of the PL features attributed to the ERS signal. d) Polarization degree of the excitonic emissions of samples 7977-10 (green), 7977-8 (red), and 7977-4 (blue). The ρ values of the cΓ1-HH1 (cΓ2-HH2) emission are reported in the upper (lower) panel. Positive (negative) values refer to counter-circular (co-circular) photons, under σ^- excitation.

signals. The energy of the transitions between confined states decreases when the temperature increases, as expected from the Varshni's law [37] (Eq. 1.1). The energy of the PL features attributed to ERS, instead, is almost constant, changing by only few meV.

In Fig. 3.3d) we summarize the measured degrees of polarization of the cΓ1-HH1 and cΓ2-HH2 PL peaks of the samples. These PL structures show circular polarization over the whole studied temperature range. For the cΓ1-HH1 PL peaks the estimation of ρ was obtained performing a Stokes analysis (error $\leq 0.5\%$), while for the cΓ2-HH2 PL peaks the low intensity and the energy proximity with the ERS signal required spectra deconvolution in order to get the proper luminescence polarization of the interband emission. Since the detected PL structures are all characterized by circular polarization, we could calculate the polarization degree of the cΓ2-HH2 PL using the formula (App. A.2):

$$\rho = \frac{I_{\sigma_+} - I_{\sigma_-}}{I_{\sigma_+} + I_{\sigma_-}} = \frac{I_{135^\circ} - I_{45^\circ}}{I_{135^\circ} + I_{45^\circ}} \tag{3.1}$$

To obtain the corrected ρ, the values of I_{135° and I_{45° are calculated removing from the cΓ2-HH2 peak the overlapping contribution of the ERS feature, in the PL spectra at $\theta = 135^\circ$, 45°. The error on ρ increases when the temperature rises, as a result of the thermal quenching of the signal.

For sample 7977-10 we focus on data below T=60 K since at higher temperatures the PL emission overlaps with the intense ERS signal, preventing us to draw accurate conclusions. For T<60K, the cΓ1-HH1 emission is co-circularly polarized, and the ρ value is nearly constant ($\sim -65\%$). At T=4 K only electrons from the HH subband are excited to the CB, giving rise to a high degree of spin orientation [Fig. 2.3a)]. Moreover, in this

temperature range the change of the excess energy is negligible, because the shift of the transition energy due to the Varshni's law is small (few meV), explaining the nearly constant value of ρ. The same applies to the cΓ2-HH2 emission in sample 7977-8, which is characterized by a similar ρ value and by an analogous excess energy. ρ values of this emission are measured up to 180 K, because above this temperature the transition is thermally quenched. The monotonic decrease of ρ points toward thermally activated depolarization mechanisms. Electrons excited from the LH2 level indeed do not play any role, since the energy of the LH2-cΓ2 transition is larger than the excitation energy up to RT. On the other hand, when the temperature increases spin relaxation is expected due to phenomena such as electron-phonon scattering [22, 38], carrier-carrier scattering [45], and possibly backscattering from L to Γ valley [43].

The cΓ1-HH1 PL emission of sample 7977-8 is counter-circularly polarized up to RT, and it displays a bell-like shape, with a maximum of $\rho = +20\%$ at about 160 K. As mentioned before, at T=4 K its polarization is almost zero, evidence of a balance between the two contributions with opposite helicity. The dominance of the counter-circular contribution at higher temperatures resembles the polarization behavior of the direct emission in bulk Ge (sec. 1.2.1). As a consequence, we guess that the enhancement of the counter-circular polarization is due to the photoexcitation of electrons from the LH1 states. When the temperature rises this mechanism is boosted due to band-gap shrinkage. Moreover, the decrease of ρ at T>160 K highlights the activation of the already mentioned depolarization mechanisms.

In sample 7977-4 the polarization of the cΓ1-HH1 and the cΓ2-HH2

PL emissions are almost temperature independent. The polarization degree of the cΓ2-HH2 emission, $\sim +20\%$, is reported in the 100 - 200 K range, because at T$<$100 K it completely overlaps with the ERS signal, while at T$>$200 K the PL intensity goes to zero. For the cΓ1-HH1 we found $\rho \sim +5\%$: above 160 K a shallow depolarization can be recognized, which might be the signature of spin relaxation. Since sample 7977-4 presents thicker QWs with respect to the previous samples, the contribution of photoexcited electrons from the LH1 states is larger, and the LH2-cΓ2 transition is already activated at low temperature [Fig. 3.1a) and b)]. The temperature independence of ρ for cΓ1-HH1 and cΓ2-HH2 emissions thus suggests that the relative portion of electrons photoexcited from the HH1 (HH2) and LH1 (LH2) subbands does not change much when the temperature increases. Furthermore, in the 100 - 200 K range resonant excitation of electrons from the LH continuum to the bottom of the cΓ2 subband [Fig. 3.1a)] may take place, providing an additional counter-circular contribution to the cΓ2-HH2 emission, as described in the previous section.

3.4 Power dependence of the cΓ1-HH1 emission polarization

In the literature optical investigations of low-dimensional materials very often report about excitons, because confinement enhances the Coulomb interaction, and favors the exciton formation [81, 82]. For the same reason, excitonic phenomena are less important in bulk materials. In the study of Ge QWs reported so far, our interpretation relied on a single particle picture. Indeed, the exciton can form from carriers which have already undergone

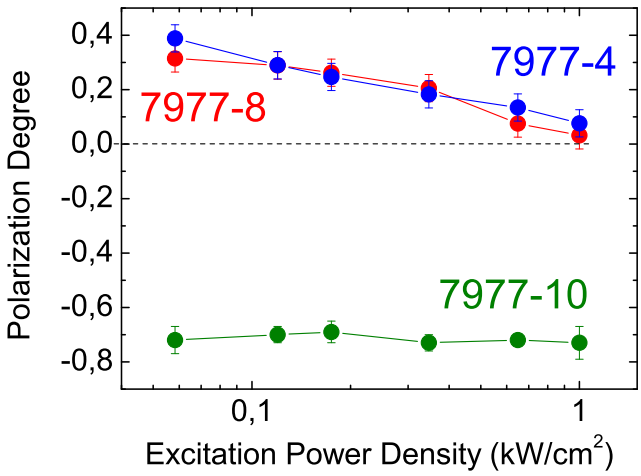

Figure 3.4: Power dependence of the polarization degree obtained for the cΓ1-HH1 emission line of samples 7977-10 (green), 7977-8 (red), and 7977-4 (blue), at T=4 K.

energy and/or spin relaxation, in which case the exciton inherits the spin properties of the carriers at the moment of their binding. Besides, once an electron-hole pair binds in exciton, the most efficient spin relaxation mechanism reported for direct excitons in QWs is provided by the electron-hole exchange interaction [8]. This mechanism is expected to increase its efficiency with the exciton concentration. In the following, we describe the dependence of the cΓ1-HH1 emission polarization on the excitation power density (D), which may highlight the role of excitons in the spin relaxation of the photoexcited carriers in Ge QWs.

Figure 3.4 displays the values of ρ obtained for the cΓ1-HH1 PL peak as a function of D, at T=4 K. In all the samples, the PL peak shows circular

polarization type over the 0.05 - 1 kW/cm^2 D range. In samples 7977-4 and 7977-8 ρ increases when D decreases, which is the evidence that a higher number of photoexcited carriers corresponds to a larger depolarization effect. This behavior compares well with the electron-hole exchange interaction [8]. Although these findings are in good agreement with the excitonic formation in Ge QWs, we cannot rule out completely that the observed depolarization is due to carrier-carrier scattering among electrons (which may provide similar effects to those detected in bulk Ge (sec. 1.2.2).

Besides, in sample 7977-10 the value of ρ is constant over the studied D range, indicating that the enhancement of D does not add any contribution to the spin relaxation. Since this sample is characterized by narrower QWs (Tab. 3.1), we might speculate that screening effects among excitons or free carriers prevent depolarization with increasing D [8].

Chapter 4

Electron Spin Resonance of conduction electrons in Ge QWs

The most accurate technique, up to now, to gather information on the spin-orbit coupling of electrons in semiconductor-based structures is the Electron Spin Resonance (ESR). Moreover, it can provide information on the spin decoherence time (T_2) and the spin relaxation time (T_1). ESR reveals the derivative signal of the spin-flip microwave absorption by electrons in a uniform magnetic field. Scanning the magnetic field at constant microwave frequency, "spectra" are obtained from which the g factor is evaluated. The latter is modified by spin-orbit interaction. Since electrons interact with the environment usually through phonons, Elliott-Yafet interaction and Dyakonov-Perel interaction [22], the oriented carriers can relax to the ground state flipping their spin. The average time for this process is called *spin relaxation time* or *spin-lattice relaxation time*. Interactions among carriers influence the phase of their spins, making them rotate around the

orientation direction. The time in which a spin looses information on its initial phase is called *spin decoherence*, *spin dephasing* or *spin-spin relaxation time*.

The detection of the ESR of conduction electrons in Ge has constituted one of the challenges of the experimental physics of the last fifty years. The main reason is the peculiar strong anisotropy of the g factor of electrons in the L valleys of the CB, which is usually not observed in the donor states. Indeed, donor electrons are the easiest ones to be addressed by ESR due to their long spin decoherence time; nevertheless in their singlet ground state the spin-orbit interaction is isotropic [16]. As summarized briefly in section 4.1.1, several researchers investigated the ESR of CB electrons in bulk Ge, but only very recent experimental observations [83] unambigously confirmed the theoretical prediction of the g factor published at the end of the 1950s [14].

Such activity constitutes the starting point for the experimental study of conduction electrons confined in Ge nanostructures. Remarkably, the Ge QWs are almost unexplored: to the best of our knowledge, only one theoretical prediction of the g factor anisotropy in these structures [84] has been reported so far in the literature. In this chapter we thus present the first experimental ESR data on conduction electrons in type I Ge QWs.

The measured g factor as a function of the QW width shows a strong evidence of the confinement effect, in good agreement with the theoretical prediction. We found that the observed lineshapes and the g values are similar to those reported in bulk Ge. Our study of the linewidth provides the first information on the spin decoherence and relaxation times of confined electrons in two-dimensional Ge-based systems.

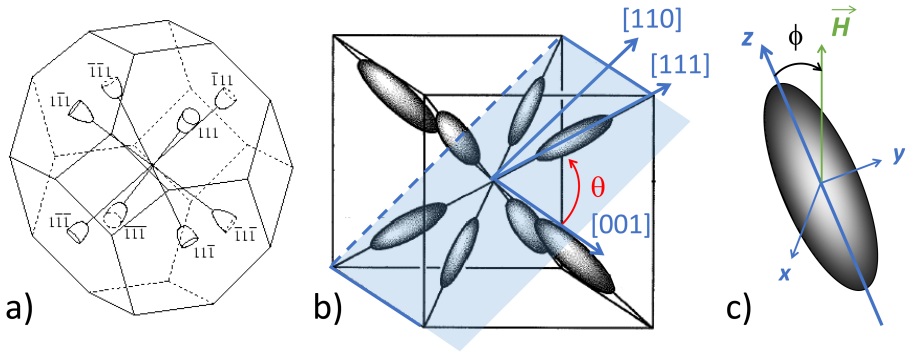

Figure 4.1: a) First Brillouin zone of bulk Ge. Ellipsoidal constant energy surfaces near the *L* minima of the CB of Ge: b) orientation of the ellipsoids respect to the crystal axes. The coloured region indicates the $(1\bar{1}0)$ plane, in which the magnetic field rotates in ESR measurements. The magnetic field orientation is indicated by the angle θ. c) Single ellipsoid: axes and angle ϕ.

4.1 *g* factor of conduction electrons

4.1.1 *g* factor in bulk Ge: a summary

In solids the *g* factor deviates from the free electron value ($g_e = 2.0023$) due to spin-orbit interaction [85]. As shown in Fig. 4.1, in Ge the fundamental minima of the CB at the *L* points of the Brillouin zone provide ellipsoidal constant energy surfaces. *g* is thus anisotropic [86], and the *g* tensor has two independent components: $g_{zz} = g_{\parallel}$ along the main axis of the ellipsoid, and $g_{xx} = g_{yy} = g_{\perp}$ along the directions perpendicular to the *z* axis [87].

In ESR measurements, the magnetic field $\vec{H}$ is rotated preferentially in the $(1\bar{1}0)$ plane from the [001] to the [110] direction in the crystal [Fig. 4.1b)] since for that rotation axis also the [111] direction is met. The

orientation of the magnetic field is indicated by the angle θ between $\vec{H}$ and the [001] direction. Fig. 4.1b) shows that the ellipsoidal surfaces of different L minima in general have different angles relative to $\vec{H}$, with one exception: for $\vec{H}$ parallel to the [100] direction, all ellipsoids include the same angle with $\vec{H}$. At a fixed θ, we can calculate for each ellipsoid the value of the angle ϕ between the direction of the magnetic field $\vec{H}$ and the z axis of the ellipsoid [Fig. 4.1c)]. For a free electron moving on a single ellipsoidal surface, the effective g value is given by:

$$g^2 = {g_\parallel}^2 cos^2\phi + {g_\perp}^2 sin^2\phi. \tag{4.1}$$

As a result of the g anisotropy, ellipsoids with different orientations with respect to $\vec{H}$ provide different g values.

The first experimental measurements of Ge in 1959 provided a g value of about 1.56 for P, As and Bi doped samples [16], but varying between 1.6 and 1.9 in Sb doped samples under strain, depending on the crystal orientation [88, 89]. The findings on Ge:Sb therefore boosted the theoretical investigation of the system, and in the same year Roth and Lax reported the results of the first calculations of the g factor for conduction electrons in bulk Ge [14]. Taking into account the spin-orbit splitting of the VB at Γ (Δ_{SO}), the interaction of the lowest conduction subband and the highest valence subband at L, and the longitudinal and transverse effective masses, Roth and Lax found: $g_\parallel \approx 0.9$ and $2.00 < g_\perp < 2.08$. Fig. 4.2a) displays the g values obtained by Roth and Lax as a function of θ.

The theoretical investigations predicted a highly anisotropic g factor, as opposed to the Si case. Calculations by Roth and Lax also highlighted

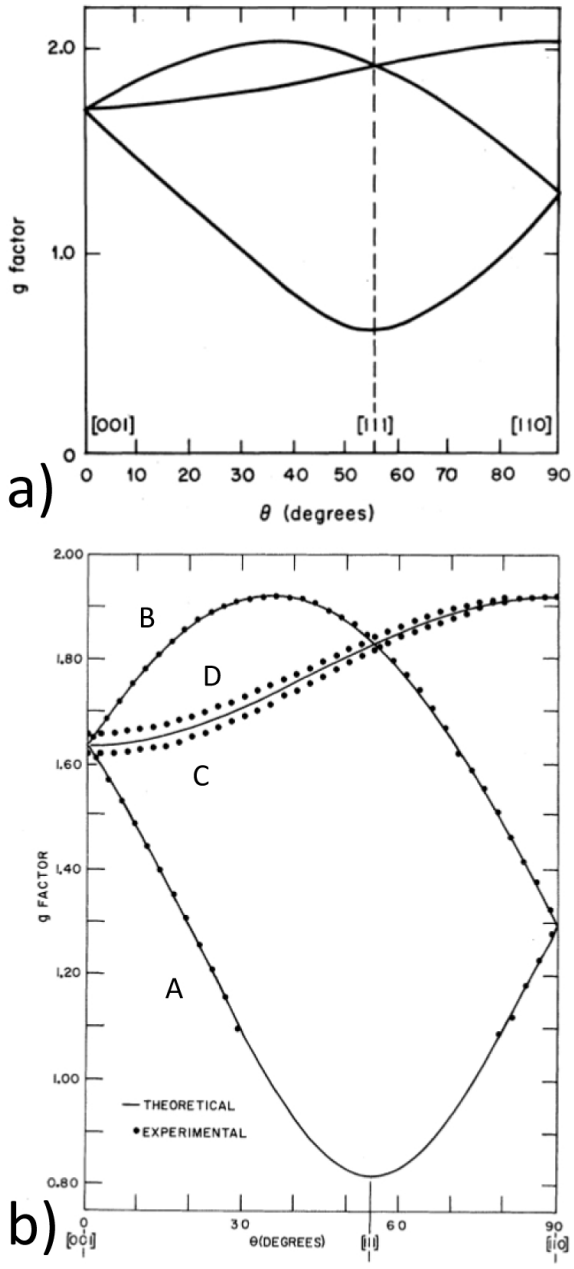

Figure 4.2: a) Theoretical prediction of the *g* factor of conduction electrons in bulk Ge from Ref. [14]. θ indicates the angle between the direction of the static magnetic field in ESR measurements and the [001] crystal axis, when the magnetic field is rotated in the $(1\bar{1}0)$ plane. b) Experimental dispersion curve from Ref. [90]. The dots are experimental data for a Ge:Sb sample (approximately 1.5° tilted respect to the holder surface on which the sample is fixed), and the solid line is the theoretical curve assuming 0° misalignement [90]. The four experimental curves are named by letters.

that the reasons of such a difference lie in the spin-orbit effect [1], and the anisotropic energy dispersion of electrons in the L valleys [87]. Actually, also the Δ valleys of the Si CB are anisotropic, but the eccentricity of the ellipsoidal surfaces is much less pronounced [91].

The results by Roth and Lax suggested that by means of Sb doping it was possible to observe the g factor anisotropy. Several ESR investigations were then carried out to deepen the understanding of Ge:Sb samples, and to clarify why the same observations were not possible with other impurities. The first relevant spectra, obtained at T$\sim$ 2 K, were reported by Pontinen and Sanders in Ref. [90]. The authors observed five lines in the ESR spectrum: one was attributed to electrons bound to the donors, and the other four, termed "new spectrum", were attributed by the authors to electrons in an impurity band. The g values extracted by the "new spectrum" are shown in Fig. 4.2b): they are in good agreement with the g factor predicted by Roth and Lax in Ref. [14] for conduction electrons [Fig. 4.2a)].

The peculiarity of the Sb in Ge consists in the small energy splitting between the singlet and the triplet state of the donor, which is $\lesssim 0.5$ meV [16, 92]. If strain is present, the singlet ground state and the excited triplet state of the donors can mix, resulting in a shift of the energy of the donor level with respect to the valleys of the CB [16]. The smaller the singlet-triplet splitting, the more likely strain mixes up the states. In the case of Sb in Ge, a strain of $\sim 10^{-5}$ along the [111] direction is sufficient to produce a new ground state of the donor above the fundamental L minimum [16, 93]. As a consequence, the donor electrons may be transfered to the lower energy

[1] In Ge the spin-orbit coupling is much larger than in Si due to the heavier atomic mass, as shown by the Δ_{SO} value: at RT $\Delta_{SO} = 0.29$ eV in Ge and 0.044 eV in Si.

L valleys, and the ESR signal of conduction electrons can be detected [94].

Mitsuma and Morigaki (Ref. [93]) applied an external compressive stress to a Ge:Sb sample, and found that the appearence of the "new" resonances depends on the direction of the applied tensile strain. Later on some researchers succeded in observing the "new spectrum" also in relaxed samples, in which the strain was probably induced locally by defects [94, 16]. In 1975, Hanle and co-workers studied surface-damaged samples (Ref. [92]), and detected the "new spectrum" only in some of them, highlighting a strong relation between the "new" resonances and the damage of the surface. The authors carried out a detailed analysis of the ESR spectrum, and confirmed the attribution of the "new" resonances to conduction electrons in the *L* valleys of the CB. The measurements provided $g_{\parallel} = 0.828 \pm 0.003$ and $g_{\perp} = 1.915 \pm 0.001$, in excellent agreement with the previous experimental and theoretical findings. Hanle and co-workers attributed the evidence of the "new spectrum" to the "surface strain" induced by mechanical damaging. Nevertheless, the authors did not report direct information on the effects produced by the surface damage, but only deduced information about strain from the ESR study. Consequently, although their interpretation is highly probable, it is still not complete.

Afterwards, no data on the *g* factor of CB electrons in Ge were reported in the literature until in 2012 Hautmann and Betz performed Faraday Rotation measurements on intrinsic and n-doped bulk Ge [83]. In this work, the authors exploited photoexcitation to populate the *L* valleys, and then studied the Faraday rotation transients, so that the attribution of the results to CB electrons is fully reliable. Hautmann and Betz reported $g_{\parallel} = 0.81 \pm 0.03$ and $g_{\perp} = 1.90 \pm 0.02$, in agreement with the ESR data, thus giving an

unambiguous confirmation to the previous studies. Faraday Rotation measurements provided g evaluations with an error of 10^{-2}, which is one order of magnitude larger than the error reported by Hanle and co-workers. As a result, the ESR technique provides so far the most accurate measurements of g.

4.1.2 g factor of conduction electrons in Ge QWs

The advent of nanostructures moved the attention of scientists to the magnetic properties of confined carriers, and to the effects of the low-dimensionality on the g factor of electrons [95, 96]. Focusing on Ge QWs, in 2003 Baron et al. reported a theoretical investigation of the Zeeman effect of electrons in the L valley, based on a $\mathbf{k}\cdot\mathbf{p}$ model [84]. Starting from the calculation of the bulk g tensor, Baron and co-workers developed the corrections to the g values for different orientations of $\vec{H}$, due to quantum confinement and strain effects. These authors reported the evaluations of g for $\vec{H}$ along the growth direction of the structure ([001] direction, *perpendicular* configuration of the magnetic field) and for $\vec{H}$ in the QW layer (parallel to the [110] direction in the crystal, *in-plane* configuration). The theoretical investigation predicts a considerable increase of the g values with respect to bulk Ge, which, to the best of our knowledge, has not been supported by experimental evidences so far.

In the following, we report the results of ESR measurements on undoped and modulation doped Ge/SiGe QWs. Modulation doping provides the spatial separation of the carriers from the impurities, due to the energy profile of the structure [97]. Because of the potential profile, donor electrons are transfered from the barriers to the QW layers. In the QW the carriers

Table 4.1: Undoped and modulation doped Ge/$Si_{0.15}Ge_{0.85}$ QWs samples studied by ESR in this work (App. C). The QW widths reported are measured by XRD, and values of $g_{\parallel}$ and $g_{\perp}$ are obtained by fitting the data (sec. 4.2).

sample	doping	well thickness (nm)	$g_{\parallel}$	$g_{\perp}$
7909-11	undoped	22.6±1.0		
8931-F8	n-type	20.4±1.0	0.907±0.005	1.915±0.004
8931-F4	n-type	17.1±0.3	0.917±0.003	1.913±0.003
8931-H5	n-type	15.8±0.2	0.923±0.003	1.909±0.004

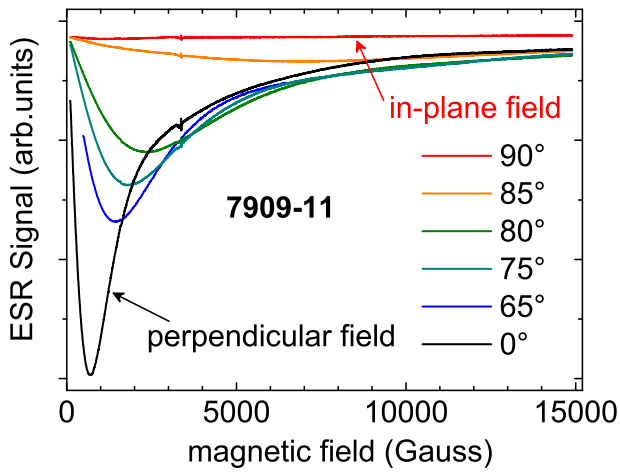

Figure 4.3: Cyclotron Resonance signal at different angles in undoped Ge QWs at T=2 K, showing the expected behavior for a 2d carrier gas. Measurements are labeled by the value of θ.

are free. Moreover, these electrons are not affected by spin depolarization mechanisms due to impurity scattering, thanks to the remote doping.

We performed ESR measurements at T=2 K on Ge/$Si_{0.15}Ge_{0.85}$ QWs, in the X band of microwave frequencies, and scanning over a magnetic field range from 80 to 15080 G. The studied samples are described in App. C, and the structural details are listed in Tab. 4.1. We used a Bruker Elexsys and a Varian machine, equipped with a liquid helium cryostat (see Appendix E). The sample was mounted on a quartz holder. According to the literature we define the angle $\theta = 0^\circ$ for a magnetic field $\vec{H}$ parallel to the growth direction z of the QW structure. Since the cleavage planes of Ge belong to the [011] family, a rotation of the sample by 90° corresponds to a rotation of $\vec{H}$ in the $(1\bar{1}0)$ plane from the growth direction [001] to the [110] direction in the crystal ($\vec{H}$ parallel to the QW plane) [Fig. 4.1b)].

In ESR measurements, the coupling of the microwaves with the circular motion of free carriers in a magnetic field provides the Cyclotron Resonance (CR) signal [98]. Figure 4.3 shows the CR observed in the undoped QWs of sample 7909-11 for different θ angles in the 0° to 90° range. The signal does not depend on the $\vec{H}$ intensity when $\vec{H}$ is directed along the QW plane (red line in Fig. 4.3), while it exhibits a pronounced dip when $\vec{H}$ is perpendicular to the QW plane (black line in Fig. 4.3). According to the Lorentz's law, the circular motion of carriers in free space takes place in a plane perpendicular to $\vec{H}$. Actually, in QWs electrons can move only in the QW plane, therefore only the perpendicular component of the magnetic field is effective. As a consequence, the observed CR presents the expected behavior of a two-dimensional (2D) carrier gas [98]. When light with energy higher than the energy gap of the QW is shed on the sample we observed

an increase of the signal intensity, indicating that the number of carriers increases under illumination. In the ESR spectra of the doped samples (Tab. 4.1), in addition to the CR signal, four well defined spin resonances are observed (Figure 4.4), as discussed in details below. These signals are light-sensitive, and their area increases under illumination; furthermore they exhibit an highly anisotropic *g* factor (Fig. 4.5), as expected from the free carrier behavior. From all the aforementioned experimental findings we conclude that the described detected signals come from a free 2D electron gas residing inside the QWs. In the undoped sample this is probabaly due to the unintentional residual doping related to the heteroepitaxial growth, which would be not large enough to provide the spin resonance signals. In the modulation doped samples, instead, this is expected due to free carriers confined in the QWs.

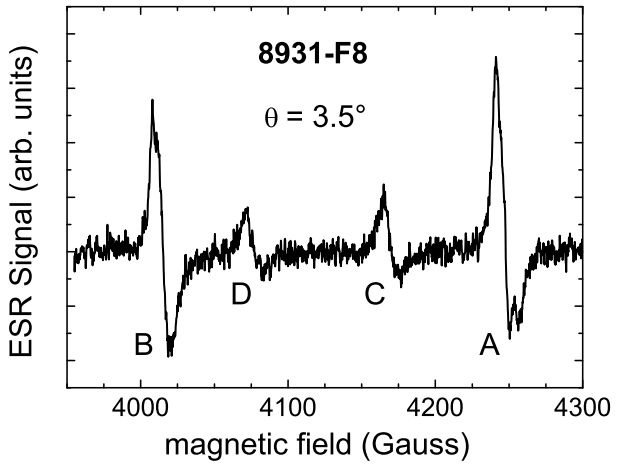

Figure 4.4: Spin resonances detected in sample 8931-F8 at T=2 K and θ =3.5°.

In the following we will focus mainly on sample 8931-F8, but similar results are found in the other doped structures, as reported in the next section. Figure 4.4 shows the spin resonances detected in sample 8931-F8 at $\theta = 3.5^\circ$, and T=2 K. The magnetic field intensity at which each resonance appeares (H_{res}) determines its g factor through the formula (App. E):

$$g = \frac{f}{H_{res}} \cdot 0.714485 \tag{4.2}$$

where f is the microwave frequency in GHz, and H_{res} the magnetic field intensity in kG. Since the signals were detected using the same f, they present different g factors. The g factor of each resonance changes with the sample orientation.

The values of g obtained for the four spin resonances as a function of θ are reported as blue triangles in Figure 4.5. The resonances C and D do not coincide, probably due to a small misalignement of the sample of $\sim 1^\circ$ [90] [2]. In Fig. 4.5 the red lines display the angular dispersion of g calculated through Eq. 4.1 using the values obtained by Baron et al. in Ref. [84] for $Si_{0.3}Ge_{0.7}$/Ge/$Si_{0.2}Ge_{0.8}$ QWs with thickness of about 20 nm, similar to that of sample 8931-F8. As metioned above, Baron and co-workers developed a $\mathbf{k}\cdot\mathbf{p}$ model and calculated an enhancement of the g value resulting from confinement effects, similar to the one predicted and observed in III-V QWs [95, 99]. Furthermore, Baron et al. suggested that the behavior of the dependence of the g factor on θ in Ge QWs would be similar to the one reported for bulk Ge. The dashed lines in Fig. 4.5 show the g factor of L electrons in bulk Ge, calculated using Eq. 4.1 with $g_{\|}$ =0.82 and $g\perp$ =1.93, which are the values assumed by Baron and co-workers in their model for

[2] tilting of the sample with respect to the holder surface

the bulk limit. The calculation of g using other sets of $g_{\parallel}$ and $g_{\perp}$ reported in the literature, always provides smaller values for bulk Ge with respect to QWs.

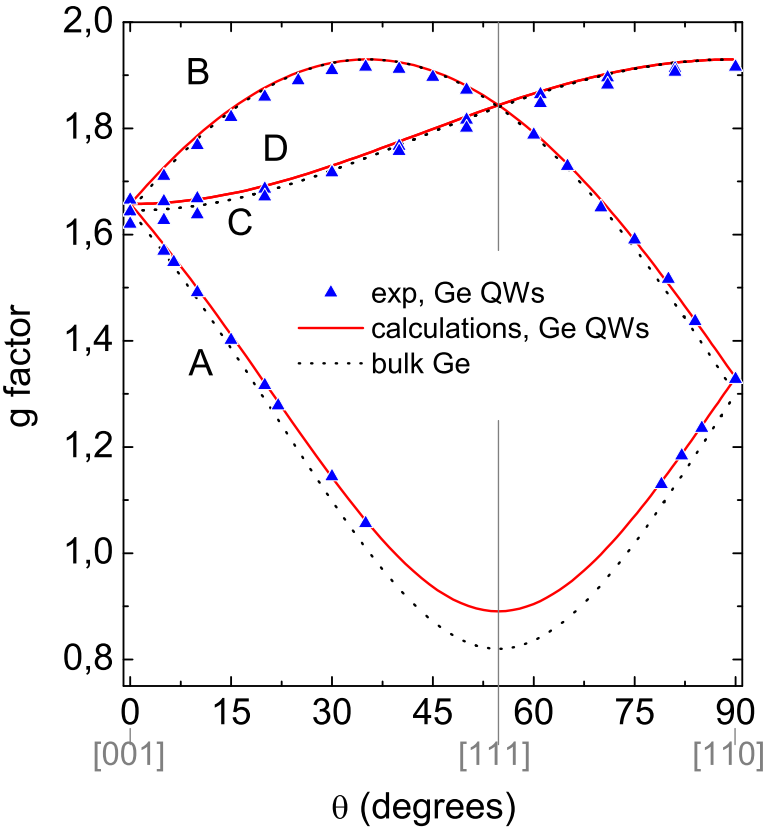

Figure 4.5: Angular dependence of the g factor measured in sample 8931-F8 (blue triangles), and calculated for bulk Ge (dotted line) and for 20 nm Ge/SiGe QWs (red line), using Eq. 4.1 and the g values in Ref [100] and Ref [84], respectively. Letters refer to the resonances of Fig. 4.4.

Our data constitute the first experimental observation of the g factor of confined electrons in Ge QWs. The measured g values will follow the calculated bulk dispersion, but they exhibit larger values with respect to bulk Ge due to the confinement effect, as shown in Fig. 4.5 and confirmed by the detailed analysis in sec. 4.2.

4.2 Confinement effects on the g factor

We studied the g factor of conduction electrons in Ge QWs as a function of the well thickness. We carried out ESR measurements on samples 8931-F8, 8931-F4 and 8931-H5, characterized by the same composition of QWs and barriers, but different layer thickness: their QW width is $\sim$20 nm, $\sim$17 nm, and $\sim$15 nm respectively. In all the samples the behavior of g well reproduces the general behavior observed in bulk Ge, as shown for sample 8931-F8 in sec. 4.1.2.

In Fig. 4.6 the measured g values for the three samples with $\vec{H}$ parallel to the [001] (θ=0°) and to the [110] direction (θ=90°) are reported as a function of the QW width. In the *in-plane* configuration (θ=90°) we consider the smaller of the two g factors (Fig. 4.5), because the larger one is expected to be constant [84]. In Fig. 4.6 the dependence of g on the well thickness calculated by Baron and co-workers in Ref. [84] is also reported. The experimental data are in good agreement with the theory. In the literature it is reported that in two dimensional systems confinement acts on the spin-orbit coupling of electrons providing an enhancement of the g factor [101, 95]. The increase of the g value when the well width decreases is thus the evidence of the effect of confinement. Fig. 4.6 also shows that the enhancement of g is different for the two angles, which follows from the reduced symmetry of the heterostructure, as explained in Ref. [84].

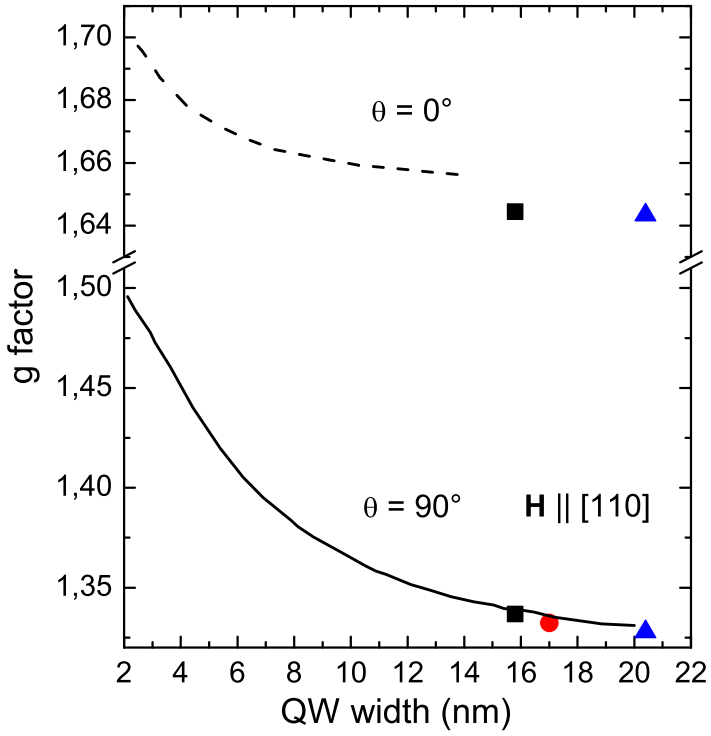

Figure 4.6: Experimental values of g in sample 8391-H5 (square), 8931-F4 (circle), and 8931-F8 (triangle) as a function of the well width, for *perpendicular* ($\theta = 0°$) and *in-plane* ($\theta = 90°$) field configurations. At *in-plane* field we did not detect a signal from sample 8931-F4. The error on g is smaller than that in the dot size determination. Calculations by Baron and co-workers in Ref. [84] are displayed by the dashed ($\theta = 0°$) and the solid lines ($\theta = 90°$).

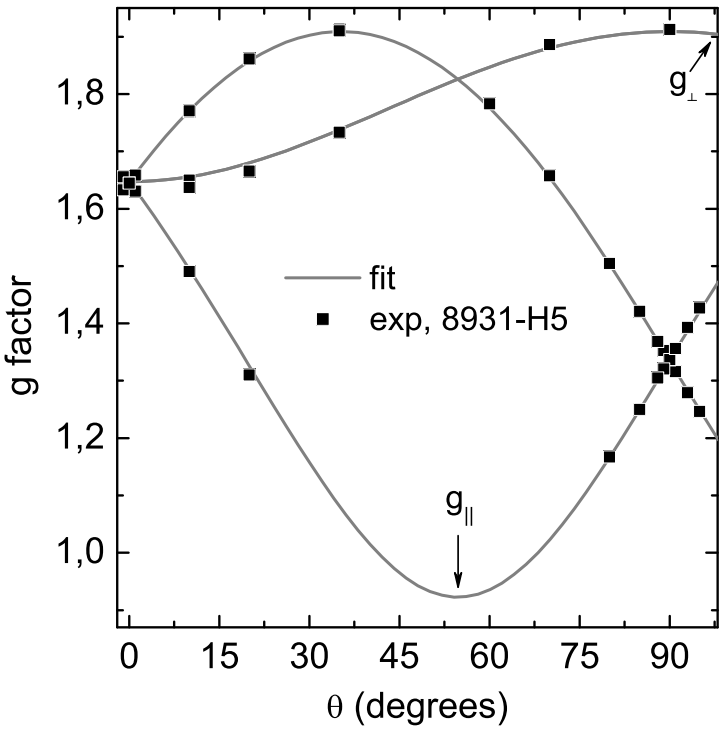

Figure 4.7: g factor measured in sample 8931-H5 (black squares) as a function of θ. Gray lines are the fits for each one of the four curves, carried out using Eq. 4.1, and assuming a perfectly oriented sample. The values corresponding to $g_{\parallel}$ and $g_{\perp}$ are indicated.

For all the samples we measured the angular dispersion of g, so that we could fit the data and extract the values of $g_{\parallel}$ and $g_{\perp}$. Figure 4.7 reports the g factor measured in sample 8931-H5 with the curves resulting from the fit. Since different curves result from different orientations of the L valleys

with respect to the magnetic field (Sec. 4.1, Fig. 4.1) each line is fitted using Eq. 4.1, with the proper values of the angle ϕ. The g values are then easily extracted from the fits: curve A at $\theta = 54.75^\circ$ provides $g_\parallel$, and curves C and D at $\theta = 90^\circ$ provide $g_\perp$.

The g values obtained for the three samples are summarized in Tab. 4.1. The value of $g_\perp$ is the same in all the samples within the error bar, and equals the bulk value in agreement with the model by Baron and co-workers [84]. On the other hand, $g_\parallel$ is strongly affected by confinement. The different behavior of the two parameters is due to the L-valley structure of the CB. In Ge the g factor is anisotropic, and $g_\parallel$ is the only component influenced by the SO interaction of the conduction states with the upper valence band. Since confinement acts on this interaction, only $g_\parallel$ is affected by the reduced dimensionality of the structure [84].

4.3 Spin decoherence and spin relaxation time

The detection of the spin resonance of conduction electrons allows us to gather information on the spin decoherence time (T_2). Spin coherence affects the linewidth of the resonance signal according to [102]:

$$T_2 = \frac{\hbar}{g\mu_B} \frac{2}{\Delta B^0_{1/2}} \tag{4.3}$$

where $\hbar$ is the reduced Planck constant, g is the g factor of the detected resonance, μ_B the Bohr magneton, and $\Delta B^0_{1/2}$ the homogeneous linewidth of the absorption signal (that can be calculated from the peak-to-peak width of the resonance, see Appendix E). As a result of inhomogeneous broadening

effects [102] the lineshape becomes Gaussian, and in this case only the *ensemble* spin decoherence time (T_2^*) can be obtained.

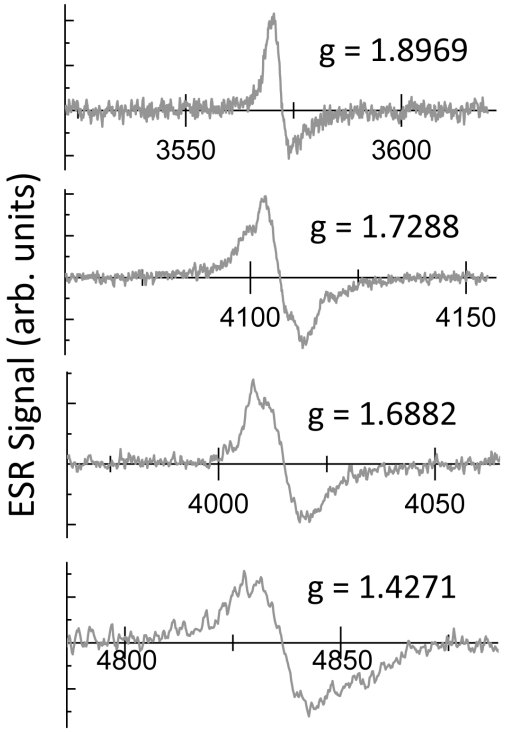

Figure 4.8: Spin resonance signals of conduction electrons in sample 8931-F8 corresponding to the strong resonances of Fig. 4.4 at different orientations. Each resonance is labeled by the g value.

Figure 4.8 shows four of the measured spin resonances obtained at different angles θ, and for different g values. The peak-to-peak width increases when g decreases, which is the same behavior reported by Hanle et al. for bulk Ge:Sb in Ref. [92]. The lineshape is also anisotropic, and shows complex features (see for instance the spin resonance at $g = 1.7288$) indicating that the signal originates from multiple contributions. It is reasonable that the presence of contributions with slightly different g factors can be attributed to the interface quality: well width fluctuations in the sample [59], and interface smoothing due to Si and Ge interdiffusion. These effects might result in confinement fluctuations due to the different effective thicknesses, affecting the g value (as demonstrated in the previous section). As a consequence, in our samples the determination of the homogeneous linewidth of the spin resonance is prevented, although the peak-to-peak width of the overall detected signal can at least provide a somewhat overestimated value of the $\Delta B^0_{1/2}$. Using Eq. 4.3, we obtain a lower limit of T_2^*, that we name T_2^{low}.

The obtained T_2^{low} times are reported in Figure 4.9: they range from few nanoseconds to tens of nanoseconds depending on the orientation and on the g factor. In Fig. 4.9, the dashed lines (guides for the eyes) highlight the trends obtained for curves B, C, and D (Fig. 4.5). According to Eq. 4.3, the calculated values depend on the inverse of the product of g and $\Delta B^0_{1/2}$: longer times are found for the spin resonances characterized by larger g (Fig. 4.8). For the resonances of curve A only three data are reported (black circles) because the measure of the peak-to-peak width was hampered by the low intensity of the signal, due to the increase of the linewidth. We note that T_2^{low} is systematically of the order or larger than T_2^* values reported for

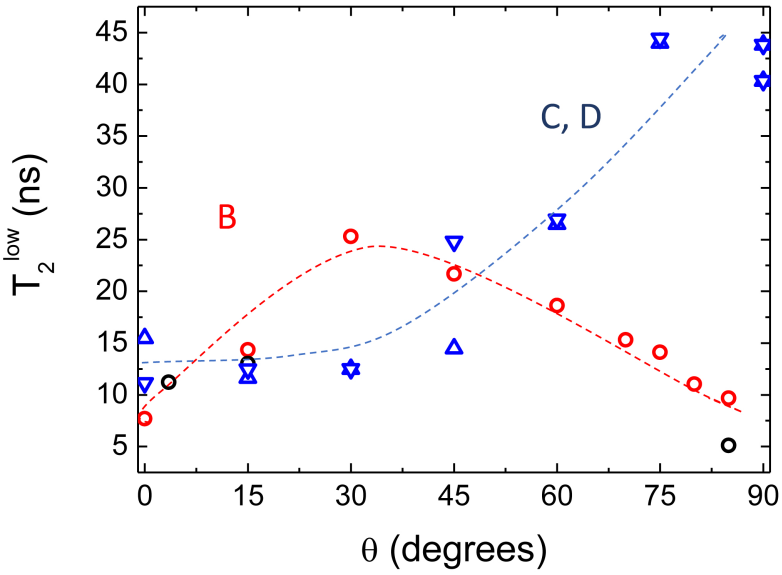

Figure 4.9: Lower limits of the ensemble spin decoherence time as a function of θ, estimated from the spin resonances in sample 8931-F8 using Eq. 4.3. The red circles are obtained from the signals of curve B (Fig. 4.5), black circles from curve A, and blue triangles from curves C and D. The dashed lines are guides for the eyes.

bulk material in Ref. [83], possibly suggesting that confinement reduces the spin decoherence effects in Ge QWs respect to bulk Ge.

In addition to the information about T_2, the ESR technique can provide an evaluation of the spin relaxation time (T_1), when the spin resonance is measured in saturation regime (App. E). In our experimental investigation we were not able to observe any saturation effect, which is an indication of rapid spin relaxation. Nevertheless, if the T_2 value was known, we could

provide an overestimation of T_1 through the formula [102]:

$$T_1 \ll \frac{1}{H_1^2 (g\mu_B/\hbar)^2 T_2} \tag{4.4}$$

where H_1 is the amplitude of the microwave magnetic field inside the sample. Since we estimated only T_2^{low}, we calculated a further overestimation of T_1 substituting T_2 with T_2^{low} in Eq. 4.4. The resulting times are of the order of the hundreds of ns. We do expect that a more accurate estimation of the spin relaxation time in Ge QWs can be obtained by a refining of the ESR measurements, possibly supported by other complementary techniques.

In the following we compare data concerning T_1 with the findings obtained by the PRPL study of Ge QWs reported in sec. 2.3. PRPL measurements of the indirect gap emission provided circular polarization, showing that in the low temperature regime the spin depolarization is slower than the radiative recombination. The latter is known to be in the nanosecond range [68]. As a consequence, the ESR estimate of T_1 is in full agreement with the observation of the circular polarization of the indirect gap emission by PRPL. Spin relaxation times obtained by the two different techniques, ESR and PRPL, are anyway expected to be comparable because the dominant spin relaxation process for electrons in the L states is the same in the two investigations. At $T < 30$ K the most efficient spin depolarization mechanism is the *intravalley* electron-phonon scattering involving long-wavelength (low-k) acoustic phonons [22]. Finally, we note that in the low temperature regime the intrinsic spin lifetime of conduction electrons although predicted to be very long (of the order of μs) may be reduced by other mechanisms such as interaction with impurities and electron-hole exchange interaction, which is expected to be more sizable in QWs [53].

Conclusions

In the last three years the spin properties of conduction electrons in Ge stimulated a lot of interest. The first theoretical prediction, and the first electrical and magneto-optical measurements of the intrinsic spin lifetime appeared in the literature. In these years I carried out an all-optical investigation of the carrier spin in bulk Ge and in Ge heterostructures. The Ge band structure presents an absolute minimum at the L point of the Brillouin zone, which at room temperature in only 140 meV below the minimum at the Γ point. Therefore, the optical properties of Ge are dominated by the direct optical transitions [28], and the radiative recombination through the direct and the indirect gap can be observed in the same photoluminescence spectrum. These peculiar properties are reflected also in the optical spectra of Ge-based quantum well (QW) structures. The decay time of the direct emission is limited by the ultrafast transfer of electrons to the side valleys [45], resulting to be orders of magnitude shorter respect to the one of the indirect gap recombination [32]. Such different decay times offer an efficient tool to decouple the spin dynamics of photoexcited holes and electrons, unlike the direct gap materials. The polarization of the direct emission provides information on the fast spin relaxation of holes, while

the polarization of the indirect emission can be exploited to estimate the spin lifetime of electrons.

Polarization resolved photoluminescence (PRPL) measurements of bulk Ge showed evidence that the polarization from both direct and indirect gap emission is circular. Indeed, this is the proof that a non-equilibrium spin distribution is created in the conduction band (CB) upon absorption of circularly polarized light. The comparison between the data and the results of a Monte Carlo simulation allowed us to push forward the understanding of the spin physics of Ge-based systems respect to the state of the art knowledge. A detailed picture of the carrier and spin relaxation mechanisms was outlined. Experimental data were explained assuming that in Ge the photoexcitation of electrons from the valence band with circularly polarized light creates a spin distribution in the Γ valley, which is affected also by the carrier dynamics in the side valleys. As a result, the thermalization in the X valleys, overlooked so far in the literature, controls the proportional weight of the spin up and spin down electrons in the direct gap emission. Since the ratio between the two can be tailored by temperature, free carrier concentration and excitation power, our findings demonstrated that these are effective tools to govern the spin population of the Γ valley, and consequently the helicity and the degree of polarization of the direct gap emission. Interestingly, at low temperature the effect of doping on the polarization is huge, suggesting the possibility to develop an optical technique to measure the impurity concentration in bulk Ge. The main feature of a similar tool would be the ability to address doping levels commonly not accessible by conventional techniques.

In intrinsic bulk Ge the indirect gap emission showed circular polariza-

tion, suggesting the evidence of electron spin lifetime longer than 100 μs, which is 5 orders of magnitude larger than previous literature data at low temperature (T$<$30 K).

These promising results of the PRPL study of bulk Ge paved the way for the investigation of the spin properties of confined carriers in Ge-based systems, not yet explored in the literature. PRPL measurements of Ge QWs demonstrated optical spin injection and detection in Ge-based confined systems, providing the evidence of an efficient and robust polarization of the oriented electrons. The PRPL study of Ge QWs with different layer thickness showed that the characteristic degrees of freedom of confinement can be used to get almost full control on the polarization of the lowest energy direct emission, through band gap engineering. Indeed, strain and confinement remove the degeneration between heavy holes (HH) and light holes (LH) states at the top of the valence band, opening up the possibility to photoexcite selectively electrons from the HH band, or from both HH and LH bands, which contribute to opposite spin states of electrons in the CB. Moreover, the splitting between HH and LH subbands allowed us to gather information on the spin dynamics of holes. The experimental evidence of the enhancement of the spin lifetime of LH respect to bulk Ge after the removal of the degeneration with HH states at the top of the valence band is reported. This is of interest in the direction of hole spintronics, addressed by theoreticians also in nanostructures of group IV semiconductors [103].

The indirect emission is characterized by circular polarization also in Ge QWs. In the confined systems, a higher polarization degree was observed respect to the bulk material. This result further confirms that confinement can improve the spin properties of Ge. The comparison between our data and

the theoretical prediction in bulk Ge [22] provided an indirect estimation of the spin lifetime of electrons in the *L* valley of the CB: in Ge QWs electron spin lifetime results to be around 5 ns at T = 150 K.

In order to study the spin-orbit coupling of conduction electrons in Ge QWs, I carried out Electron Spin Resonance (ESR) measurements. In addition, the ESR technique provides information on the spin relaxation and spin decoherence times of electrons at T=2 K.

Our findings constitute, to the best of our knowledge, the first ESR data of conduction electrons confined in Ge nanostructures. ESR measurements demonstrate that in Ge QWs the *g* factor is characterized by an anisotropic dispersion similar to the one observed in the bulk material [90]. Data show that the *g* factor increases in the confined system respect to the bulk as a consequence of the confinement. This provides the experimental demonstration of the effect of confinement on the spin-orbit coupling of conduction electrons in a Ge-based system, confirmed by the theoretical prediction in Ref.[84].

The analysis of the spin resonance line offers a rough estimation of a lower limit of the spin decoherence time (in the order of few tens of ns), and of an upper limit of the spin relaxation time, which is suggested to be shorter than hundreds of ns. This time range compares well with the signature of spin orientation observed by PRPL measurements for 5 ns living electrons in the *L* states of the CB.

In conclusion, this work constitutes the first study of the carrier spins in high Ge content confined structures based on original experimental measurements performed on Ge QWs, and relying on the detailed understanding of the spin properties of bulk Ge.

Appendices

Appendix A

Polarization Resolved Photoluminescence

We describe here the experimental technique for the study of the Polarization Resolved Photoluminescence (PRPL). First we provide a description of the experimental setup used for the measurements carried out in the thesis. Second, we discuss the Stokes analysis of the polarization of the emitted light. Third, since in this thesis the PRPL technique is used to address the optical orientation and the dynamics of carrier spins, we discuss the relationship existing between the spin state of photoexcited carriers and the luminescence polarization. We thus define the spin polarization of the oriented carriers and the polarization degree of the luminescence.

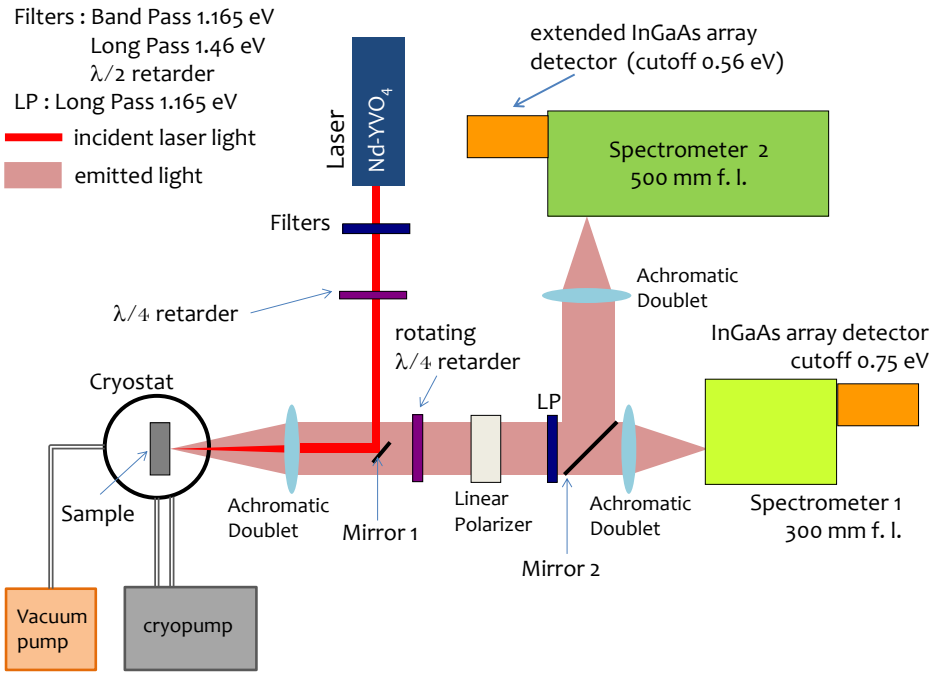

Figure A.1: Sketch of the experimental setup used for PRPL measurements.

A.1 Apparatus

Figure A.1 shows a schematic drawing of the experimental setup used in polarization resolved photoluminescence measurements.

In excitation we used a solid state Nd-YVO_4 laser operating in continuous-wave, at 1.165 eV. The power range goes from few mW to $\sim$500 mW. The source is characterized by a good stability (the power change is $\sim$2% in an hour), which is very important in order to study the light polarization

by observing the intensity modulation of the emission as a function of the retarder angle (sec. A.2).

Filters are set in order to provide completely circular polarization of the light incident on the sample. The retarder waveplate after filters works as a $\lambda/4$ retarder at 1.165 eV. Mirror 1 is a circular 3 mm diameter silver mirror, mounted on a 5 cm diameter gimball support so that most of the emitted light from the sample can reach the detection optics. An acromatic doublet with 100 mm focal length, focalizes the laser on the sample surface on a spot of about 40 μm diameter. The distance of the doublet from the sample is controlled by a micrometric screw.

The sample is mounted in a cold finger cryostat. The effect of the windows on the polarization has been verified to be negligible for the purposes of the present study. The cryostat is connected to a closed liquid helium circuit (Oxford instruments), and the vacuum inside the cryostat is obtained by a set of vacuum pumps (Pfeiffer CUBE).

The light emitted from the sample is collimated by an achromatic doublet in a 2.5 cm diameter beam. The rotating $\lambda/4$ retarder (Bernhard Halle Nachfl. RAC 6.4.25L analyzer) works the 0.5 eV - 1.77 eV range, and its rotation is governed by a remote control. The linear polarizer (Codixx colorPol IR1300BC5) is characterized by a contrast [1] larger than 10^7 in the 900-1350 nm range, and its orientation is matched in order to have maximum efficiency of the grating inside the spectrometers. The achromatic doublet (150 mm focal length) focuses the emitted light on the entrance

[1]The contrast is the ratio between the intensities of the transmitted beams when the polarizer axis is parallel or transverse with respect to the polarization axis of a linearly polarized beam.

slit of spectrometer 1 or 2. Mirror 2 can be removed for using the 300 mm spectrometer with the 0.75 eV cutoff InGaAs detector.

Spectrometer 1 is equipped by a 600 lines/mm grating and an InGaAs Andor i-Dus array detector with cutoff energy at 0.75 eV, providing an energy resolution of the PL peaks is 6 meV. Spectrometer 2 is equipped by two gratings with 75 lines/mm (blaze at $\lambda = 1700$ nm) and 35 lines/mm (blaze at $\lambda = 2300$ nm), and the switch from one grating to the other is governed by remote control. In the thesis we mainly used the 75 lines/mm granting, providing an energy resolution of 0.5 meV in the PL spectra. Spectrometer 2 is supplied by an InGaAs Andor i-Dus array detector with cutoff energy at 0.56 eV. Both InGaAs detectors are thermoelectrically cooled.

A.2 Polarimetry (Stokes analysis)

We consider a monochromatic optical beam propagating along the z direction and having the following components at $z = 0$:

$$\begin{aligned} E_x(t) &= E_{0x}\cos(\omega t + \delta_x) \\ E_y(t) &= E_{0y}\cos(\omega t + \delta_y) \end{aligned} \tag{A.1}$$

where t represents the time, ω the angular frequency, and E_{0x}, E_{0y} are the maximum amplitudes. The Stokes polarization parameters, S_i with $i = 0, 3$, are measurable observables that completely characterize the polarization state of an optical field. By representing the optical amplitudes in terms of:

$$\begin{aligned} E_x(t) &= E_x\, e^{i\omega t} \\ E_y(t) &= E_y\, e^{i\omega t} \end{aligned} \tag{A.2}$$

where:

$$\begin{aligned} E_x(t) &= E_{0x}\, e^{i\delta_x} \\ E_y(t) &= E_{0y}\, e^{i\delta_y} \end{aligned} \tag{A.3}$$

it can be shown that the Stokes parameters are given by [104]:

$$\begin{aligned} S_0 &= E_x E_x^* + E_y E_y^* \\ S_1 &= E_x E_x^* - E_y E_y^* \\ S_2 &= E_x E_y^* + E_y E_x^* \\ S_3 &= i(E_x E_y^* - E_y E_x^*) \end{aligned} \tag{A.4}$$

here the asterisk is the complex conjugate, $i = \sqrt{-1}$, and

$$S_0^2 = S_1^2 + S_2^2 + S_3^2 \tag{A.5}$$

holds for completely polarized light.

The first Stokes parameter, S_0, represents the total intensity of the optical field, while S_1, S_2 and S_3 determine the degree of linear horizontal (or vertical) polarization, linear $+45^\circ$ (or -45°) polarization and right (or left) circular polarization, respectively.

Partially polarized light can be considered as a superposition of unpolarized and completely polarized light. We can thus define the degree of polarization, ρ, as:

$$\rho = \frac{I_{polarized}}{I_{total}} = \frac{\sqrt{S_1^2 + S_2^2 + S_3^2}}{S_0} \tag{A.6}$$

where $0 \leq \rho \leq 1$, and I_{total} and $I_{polarized}$ are the total intensity and the intensity of the polarized component, respectively. When the polarization type is circular Eq. A.6 coincides with Eq. A.12, that we use if the intensity of the PL peak is low. In our work, in case of circular polarization, we use positive (negative) ρ when the polarimetric analysis provides $S_3 > 0$ ($S_3 < 0$). The error on the estimated ρ is ≤ 0.5 in all the measurements. The Stokes parameters can be written as the following vector:

$$\begin{pmatrix} S_0 \\ S_1 \\ S_2 \\ S_3 \end{pmatrix} = (1-\rho) \begin{pmatrix} S_0 \\ 0 \\ 0 \\ 0 \end{pmatrix} + \rho \begin{pmatrix} S_0 \\ S_1 \\ S_2 \\ S_3 \end{pmatrix} \tag{A.7}$$

We can therefore consider the normalized Stokes vector:

$$\begin{pmatrix} S'_0 \\ S'_1 \\ S'_2 \\ S'_3 \end{pmatrix} \equiv \begin{pmatrix} S_0 \\ S_1 \\ S_2 \\ S_3 \end{pmatrix} = \begin{pmatrix} 1 \\ S_1/\rho S_0 \\ S_2/\rho S_0 \\ S_3/\rho S_0 \end{pmatrix} \tag{A.8}$$

as a representation of the polarized component of the light. For the sake of simplicity we have dropped the primes in the normalized Stokes parameter notation. The normalized Stokes vector defines a point on a surface of a sphere of unit radius: the so called Poincaré sphere, where $(x,y,z) = (S_1,S_2,S_3)$ [Fig. A.2c)]. The Poincaré sphere is a convenient graphical method to visualize the light polarization: a linear polarization state is localized on the equator of the sphere, whereas right and left circu-

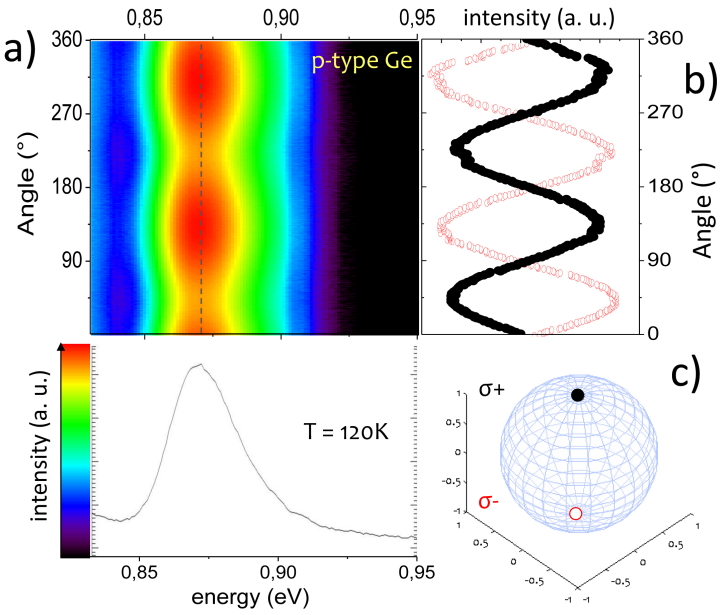

Figure A.2: Stokes analysis of the polarization of the direct gap emission in p^+-Ge sample at $T = 120$ K. a) the lower panel shows the PL spectrum at retarder angle$= 135°$; the upper panel shows a colour-coded contour plot of the PL spectra as a function of the retarder angle. b) PL peak intensity vs retarder angle: black dots are the intensities of the PL peak along the dashed line in panel a). The sinusoidal behavior is feature of σ^+ circular polarization. On the contrary, red open dots feature circular polarization with opposite (σ^-) helicity. c) Poincaré sphere: the black (red open) dot represents circular σ^+ (σ^-) polarization.

lar polarizations are at the north and south poles respectively. Elliptically polarized states are represented everywhere else on the surface.

In this work we carried out a modified classical measurement of the Stokes polarization parameters, by allowing the photoluminescence of the analyzed sample to pass through an optical retarder and a linear polarizer (sec. A.1). The retarder rotates at an angular frequency ω whereas the polarizer is kept fixed. A multiple-channel detector, chopped with the

rotating optical element, is coupled to a spectrometer and then used to determine the amplitude at a time t of the various spectral components of the emerging light beam. A Fourier analysis of the peak amplitude modulation, $I(\omega t)$, provides the Stokes parameters via the determination of the Fourier coefficients [104, 105]. In practice, the Stokes parameters can be found by a least square fit of $I(\omega t)$ with a sum of trigonometric functions. The fitting function F_{fit} has the following shape [105]

$$F_{fit}(\theta) = \frac{1}{2}\left[A - B\,sin(\pi\theta/90) + C\,cos(\pi\theta/45) + D\,sin(\pi\theta/45)\right]. \quad \text{(A.9)}$$

The Stokes parameters are then calculated from the values of F_{fit} parameters

$$\begin{aligned} S_0 &= A - C \\ S_1 &= 2C \\ S_2 &= 2D \\ S_3 &= B \end{aligned} \quad \text{(A.10)}$$

Since the PL of the investigated sample is always partially polarized, we employed the normalized Stokes parameters described above in order to construct the Poincaré sphere of the experiment. An example of full polarimetric analysis for the photoluminescence data is reported in Figure A.2.

The capability of obtaining optical orientation of electrons and hole spins has been furthermore tested by comparing luminescence data for excitation with both circular polarizations. We have thus devised a specific measurement run in which the polarization of the excitation was changed from left-handed, σ^-, to right-handed, σ^+. We report the data obtained by the measurements on the Ge quantum well sample 8351-F7 (whose study is reported in chapter 2). The PL spectra reported in Figure A.3 a) and

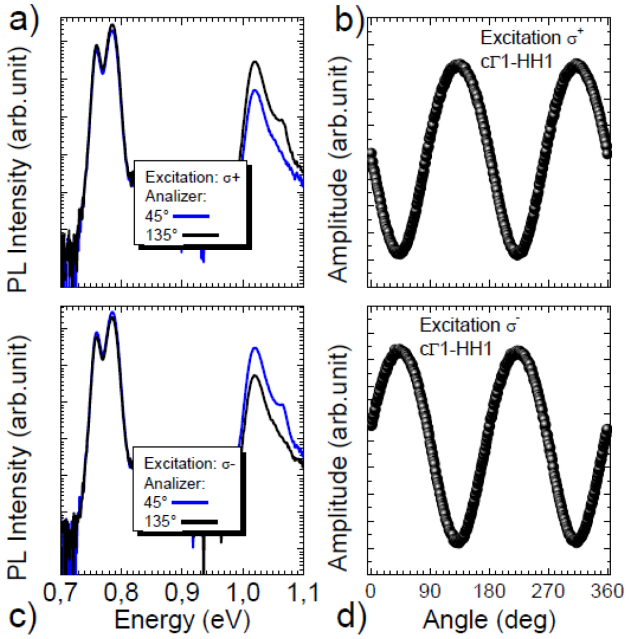

Figure A.3: a)-c) 4 K PL spectra of the Ge/SiGe MQW sample under right-handed, σ^+, a), and left-handed, σ^-, c) circularly polarized excitation at 1.165 eV. Spectra are resolved for analyzer (retarder) angles of 45° (blue line) and 135° (black line). The cΓ1-HH1 PL peak is found at ∼1.025 eV. b) and d) are the cΓ1-HH1 peak amplitude modulations reported on the same scale for a direct comparison. A mirror-like behavior of the modulations can be seen.

c) demonstrate the exchange between the two polarizations, as expected in case of optical injection of carrier spins. This results is also elucidated by the peak amplitude modulations shown in Figure A.3 b) and d) for the cΓ1-HH1 emission. It should be noted that in panel b) and d) the scale of the amplitude modulations is the same, pointing out a sinusoidal shape with a perfect mirror-like behavior under σ^- and σ^+ excitations.

A.3 Physical principles

In semiconductors the transfer of the angular momentum of absorbed circularly polarized light to the photoexcited carriers generates a nonequilibrium spin polarization. This phenomenon is known as *optical orientation*. Fig. A.4 shows the selection rules governing the exchange of angular momentum between electrons and photons for the electronic states at the Γ point of bulk Ge (the sketch is valid also for the direct gap III-V and II-VI compounds). The Bloch states are labeled by the projection m_j of the total angular momentum J on the direction of the light propagation z. σ^+ and σ^- represent the right and left handed helicity of the exciting light. The absorption of σ^+ (σ^-) polarized light corresponds to a difference of $+1$ (-1) between the m_j values of the final and of the initial state. As a result, photoexcited electrons from the light hole (LH) and heavy hole (HH) states populate opposite spin states in the conduction band. Interband transitions between different states are characterized by different rates: in Fig. A.4 each transition is labeled by its relative probability (circled number). E_g is the direct energy gap, and Δ_{SO} is the energy difference between the top of the valence band and the split-off (SO) band.

In the following, we discuss the spin polarization of electrons, and the polarization degree of the photoluminescence, referring to the paper by Zutic et al. (Ref [3]). For sake of simplicity we consider transitions between states at $k = 0$ (Fig. A.4) [2]. Calling n_+ and n_- the concentration of electrons polarized parallel ($m_j = 1/2$) and antiparallel ($m_j = -1/2$) to the direction

[2] At $k \neq 0$ the same selection rules on the spin states are valid, but the oscillator strength of the transitions is different

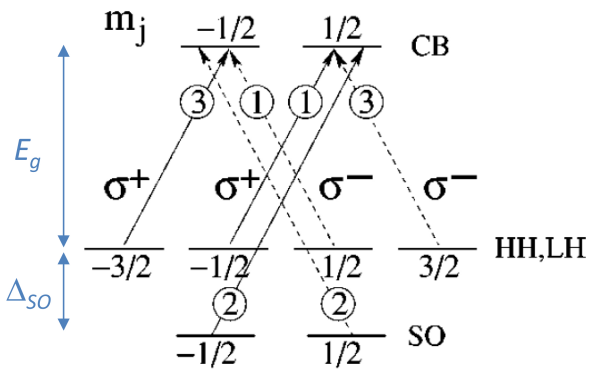

Figure A.4: Selection rules for the interband transitions between the m_j sublevels at the Γ point of the Brillouin zone of Ge, for σ^+ and σ^- (right and left handed helicity) circularly polarized light. The circled numbers indicate the relative transition intensities that apply for both excitations and radiative recombinations. The absorption transitions are depicted by the arrows.

of light propagation, we define the spin polarization as:

$$P_S = (n_+ - n_-)/(n_+ + n_-) \tag{A.11}$$

The spin polarization of the excited electrons depends on the photon energy $\hbar\omega$.

(1) $E_g < \hbar\omega < E_g + \Delta_{SO}$. In this case only the LH and HH subbands contribute. As a result, assuming σ^+ excitation, $n_+ : n_- = 3 : 1$ and from Eq. A.11 follows $P_S = -1/2$. The spin polarization of carriers generated by photoexcitation is thus antiparallel with respect to the direction of light propagation, because the transition probability is higher for transitions involving HH states than for those involving LH states. It is worth noticing that assuming σ^- excitation $n_+ : n_- = 1 : 3$ and $P_S = +1/2$.

The circular polarization degree of the luminescence is defined as

$$\rho = \frac{I_{\sigma_+} - I_{\sigma_-}}{I_{\sigma_+} + I_{\sigma_-}} \tag{A.12}$$

where $I_{\sigma_\pm}$ is the radiation intensity with helicity $\sigma^\pm$. In order to calculate ρ we have to consider both the population of the spin states right after the absorption and the selection rules (Fig. A.4). Holes are initially polarized too, but they lose spin orientation on a shorter timescale with respect to electrons [21]. Therefore we assume hole spins to be completely depolarized during the recombination, i.e. the spin states at the top of the valence band are equally occupied. Consequently, $I_{\sigma_\pm}$ depends only on the population of the spin states in the conduction band and on the relative probability of the transitions providing $\sigma^\pm$ emission. Fig. A.4 shows the transitions providing $\sigma^\pm$ emission for electrons in the c$\Gamma(\pm 1/2)$ state. $I_{\sigma_\pm}$ is proportional to the sum of the cΓ(-1/2) and cΓ(+1/2) contributions to the $\sigma^\pm$ emission: $I_{\sigma_+} \propto 1 \cdot n_+ + 3 \cdot n_-$ and $I_{\sigma_-} \propto 3 \cdot n_+ + 1 \cdot n_-$. From Eq. A.12 the following polarization degree of the σ_+ photoluminescence is obtained

$$\rho_0 = \frac{(n_+ + 3n_-) - (3n_+ + n_-)}{(n_+ + 3n_-) + (3n_+ + n_-)} = \frac{-1}{2}\frac{(n_+ - n_-)}{(n_+ + n_-)} = -\frac{P_S}{2} = \frac{1}{4} \tag{A.13}$$

where the index 0 indicates that we neglected spin depolarization mechanisms.

(2) $\hbar\omega > E_g + \Delta_{SO}$. In this case the excitation involves transitions also from the SO band. Summing up the numbers of spin up and spin down electrons created upon absorption of $\sigma^\pm$ light it results that $n_+ = n_-$. Therefore the net spin polarization of the oriented electrons is null, i.e. $P_S = \rho_0 = 0$. This underlines the vital role of spin-orbit coupling for optical

orientation. Indeed, a removal of the degeneration of different spin states together with a proper energy of the exciting photons is needed to provide optical orientation. Furthermore, the structure of the spin states in the valence band (Fig. A.4) suggests that P_S can substantially increase after a removal of the HH/LH degeneracy [39], and using $\hbar\omega \gtrsim E_g$. In chapter 3 we reported the observation of this effect in Ge QWs. In Ge QWs the electronic levels are affected by compressive strain and confinement providing the removal of the degeneration between HH and LH states. The top of the valence band is thus HH like. The study of the polarization of radiative recombination through the direct optical gap of Ge QWs shows that the almost resonant excitation results in very high polarization degrees (around 0.7 at low temperature).

While photoexcitation with circularly polarized light creates spin-polarized electrons, the nonequilibrium spin polarization decays due to spin relaxation. In continuous-wave experiments, the steady-state degree of spin polarization (ρ) depends on the balance between the spin excitation and decay. In a homogeneously doped semiconductor, the balance between electron-hole recombination and optical pair creation is given by [106]

$$r\,(n\,p - n_0\,p_0) = G \tag{A.14}$$

where r is the recombination rate, n and p the electron and hole densities, n_0 and p_0 corresponding to the equilibrium values, and G is the electron-hole photoexcitation rate (the absorption rate). Similarly, the balance between spin relaxation and spin generation is expressed by [107]

$$r\,s\,p + s/\tau_s = P_S(t=0)\,G \tag{A.15}$$

where $s = n_+ - n_-$ is the electron spin density, τ_s the electron spin lifetime,

and $P_S(t=0)$ is the spin polarization at the moment of photoexcitation (Eq. A.11). We remember that holes are considered unpolarized. The first term in Eq. A.15 describes the decay of the spin density due to carrier recombination, while the second term describes the intrinsic spin relaxation.

Merging Eq. A.14 and Eq. A.15, the steady-state electron polarization can be obtained

$$P_S = P_S(t=0)\,\frac{1 - n_0\,p_0/n\,p}{1 + 1/\tau_s\,r\,p} \tag{A.16}$$

In low excitation conditions, in a $p-$doped sample $p \approx p_0$, and $n \gg n_0$, therefore $n_0 p_0/np \approx 0$ and thus

$$P_S = \frac{P_S(t=0)}{1 + \tau/\tau_s} \tag{A.17}$$

where $\tau = 1/rp_0$ is the electron lifetime [106]. The steady-state polarization is thus lower than the initial polarization $P_S(t=0)$ by an amount depending on the ratio τ/τ_s.

In an $n-$doped sample, on the contrary, $n \approx n_0$ and $p \gg p_0$, Eqs. A.14 and A.16 give

$$P_S = \frac{P_S(t=0)}{1 + n_0/G\tau_s} \tag{A.18}$$

In this case the steady-state polarization depends on the electron spin lifetime τ_s only, and not on the hole lifetime $\tau = 1/rn_0$.

In conclusion, in continuous-wave photoluminescece experiments, under circularly polarized excitation, the steady-state spin polarization P_S of the photoexcited electrons depends on the electron spin lifetime τ_s. The longer

τ_s, the larger P_S. On one hand, for very short τ_s, $P_S = 0$. On the other hand, for very long τ_s, P_S is limited to the initial value $P_S(t = 0)$. However, $P_S(t = 0)$ can be tailored in semiconductors by the change in the electronic levels due to strain and confinement, as discussed above. The degree of circular polarization of the radiative recombination ρ is proportional to P_S (as shown in a specific case), therefore ρ depends on τ_s similarly to P_S. Noteworthy, when the photoexcitation involves states at $k \neq 0$ the behavior of P_S as a function of the excitation energy $\hbar\omega$ is more complex. Detailed calculations of P_S vs $\hbar\omega$ in bulk Ge are reported in Ref. [70].

Appendix B

Direct emission polarization vs excitation power in bulk Ge

In Section 1.2.2 we discussed the dependence of the direct emission polarization on the excitation power density (D) in bulk Ge. Here we report the intensity modulation of the direct gap PL peak obtained performing PRPL on $i-$Ge, $n-$Ge,and $p^{+}-$Ge at T=50 K, 120 K, 160 K, as a function of D. The plots report the peak intensity normalized to its mean value, therefore the amplitude of the ordinate range is an indication of the polarization degree (which can be used for comparison). In order to better recognize the polarization type we show the Poincaré spheres resulting from the Stokes analysis of the data (App. A.2), for each sample and temperature. The polarization degree obtained by Stokes analysis is plotted as a function of the excitation power density (filtering of the exciting laser): full power (100%) corresponds to 1 $\mathrm{kW/cm^2}$. The power density was changed by gray filters. The plots of the intensity modulation are labeled by the attenuation.

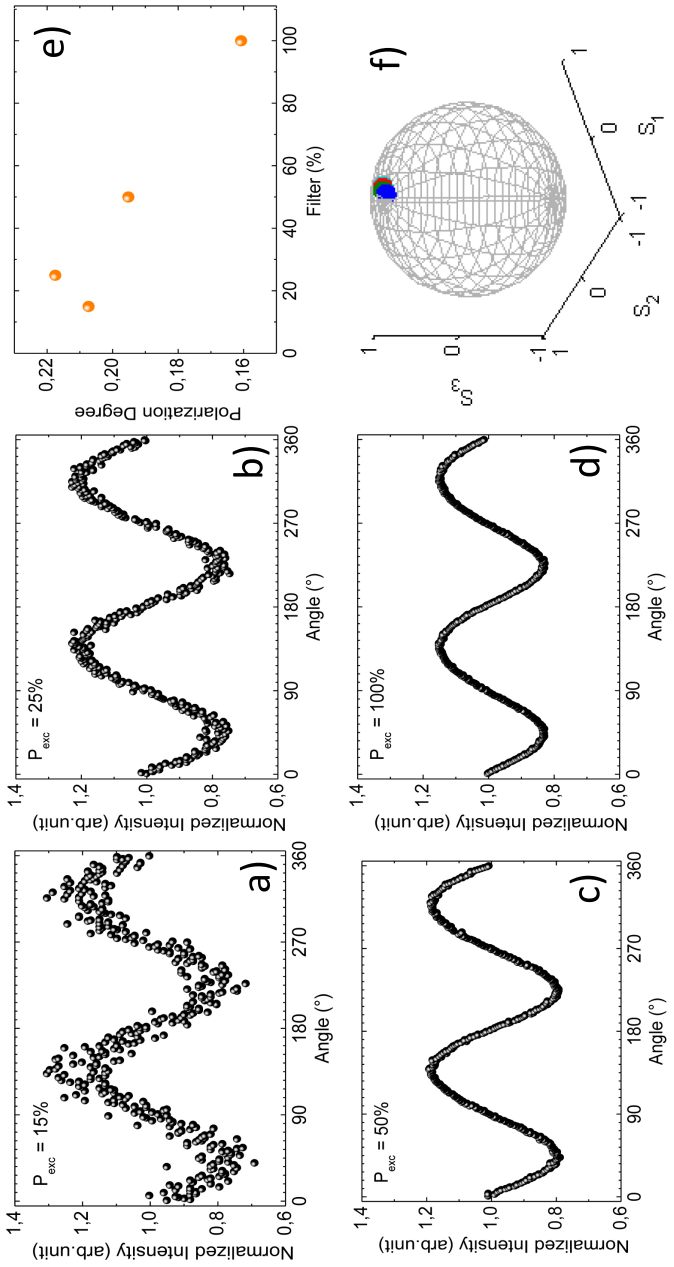

Figure B.1: (a)-(d) Modulation of the normalized intensity of the direct gap PL peak from $i-$Ge at T=50 K. (e) Polarization degrees calculated by the Stokes analysis on the data reported in (a)-(d), as a function of the excitation power (attenuation). (f) Poincaré sphere of the polarization type for the data reported in (a)-(d).

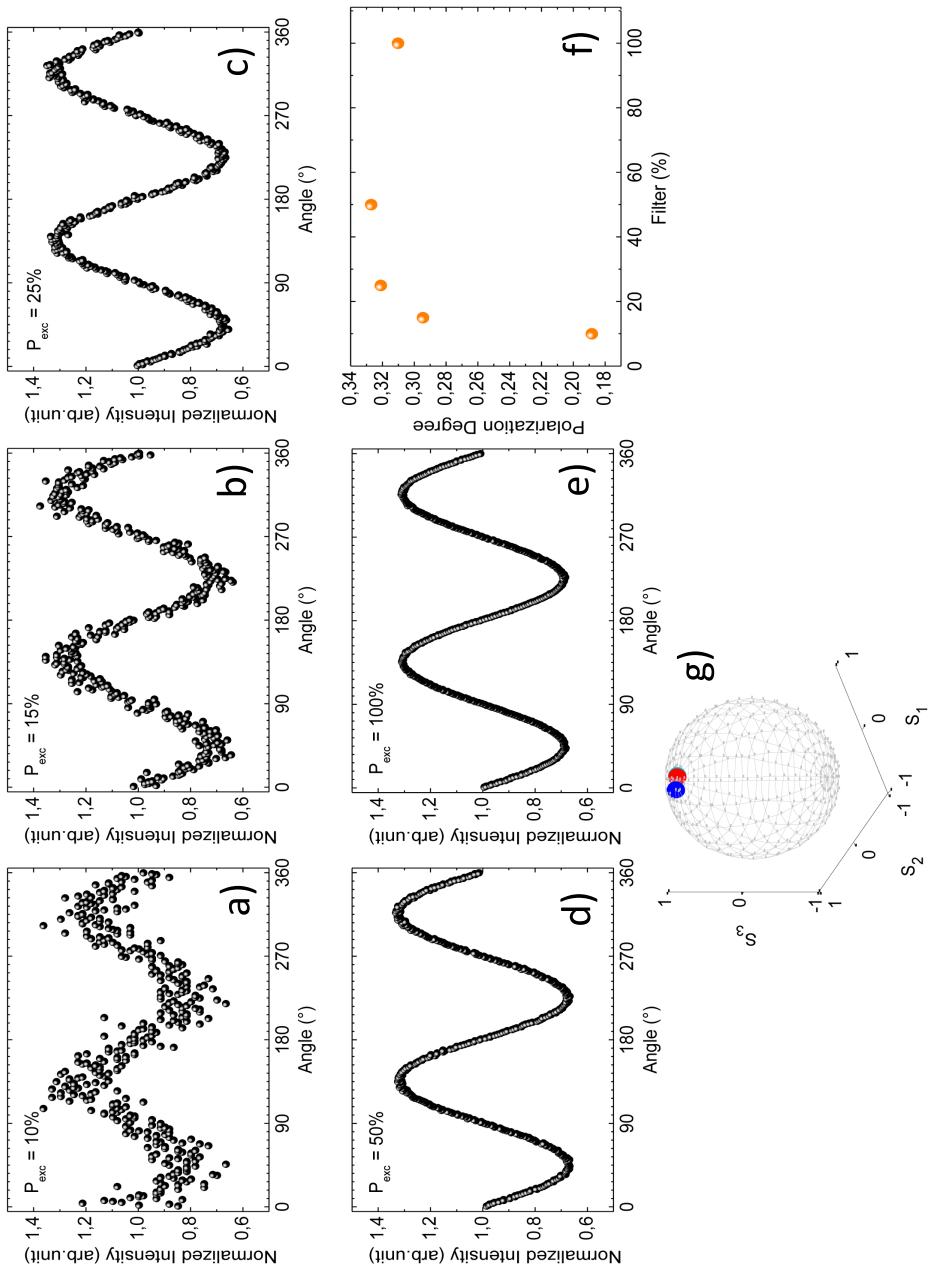

Figure B.2: (a)-(e) Modulation of the normalized intensity of the direct gap PL peak from $i-$Ge at T=120 K. (f) Polarization degrees calculated by the Stokes analysis on the data reported in (a)-(e), as a function of the excitation power (attenuation). The value of ρ at 10% attenuation is affected by the low signal-to-noise ratio. (g) Poincaré sphere of the polarization type for the data reported in (a)-(e).

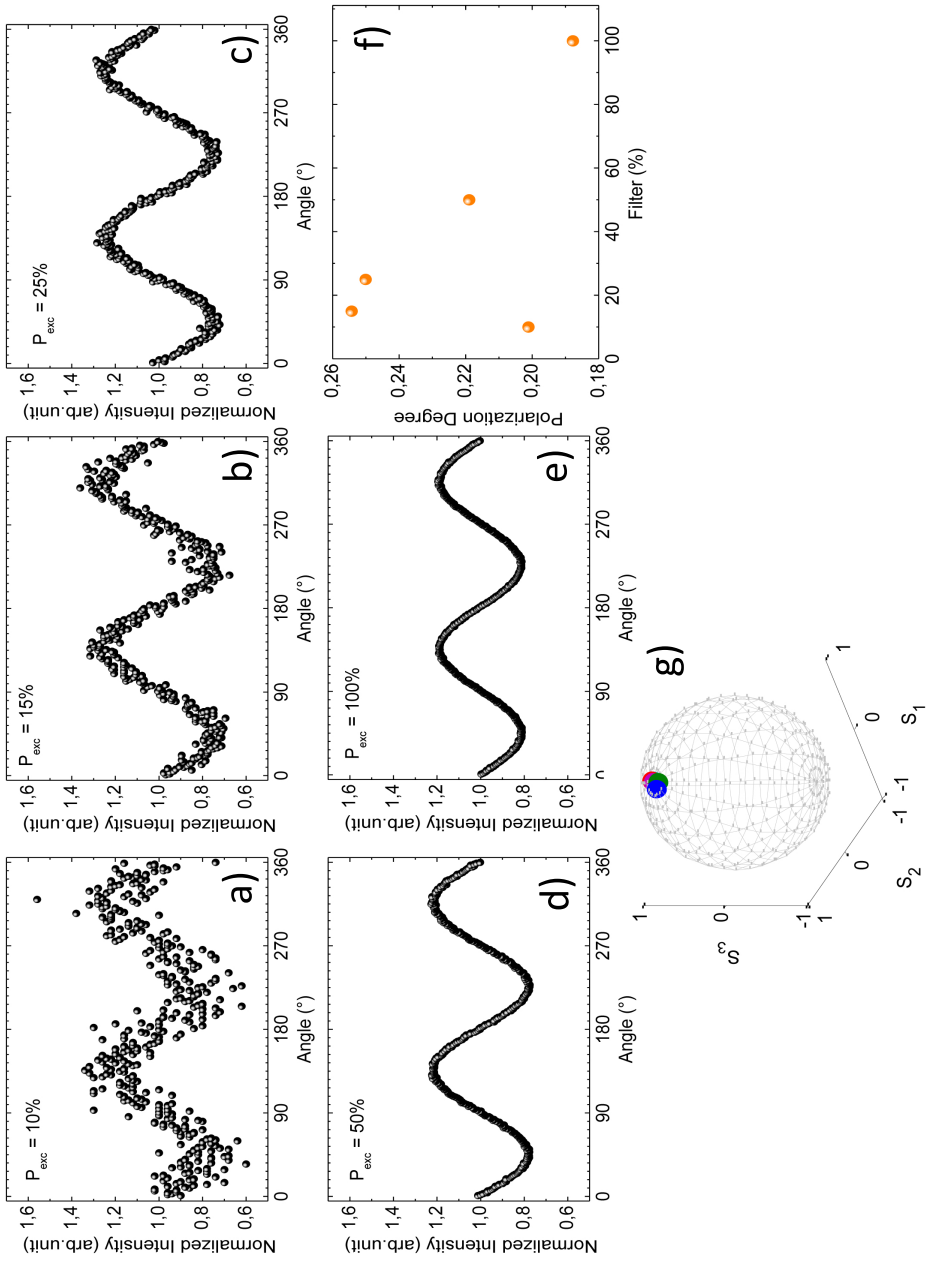

Figure B.3: (a)-(e) Modulation of the normalized intensity of the direct gap PL peak from $i-$Ge at T=160 K. (f) Polarization degrees calculated by the Stokes analysis on the data reported in (a)-(e), as a function of the excitation power (attenuation). The value of ρ at 10% attenuation is affected by the low signal-to-noise ratio. (g) Poincaré sphere of the polarization type for the data reported in (a)-(e).

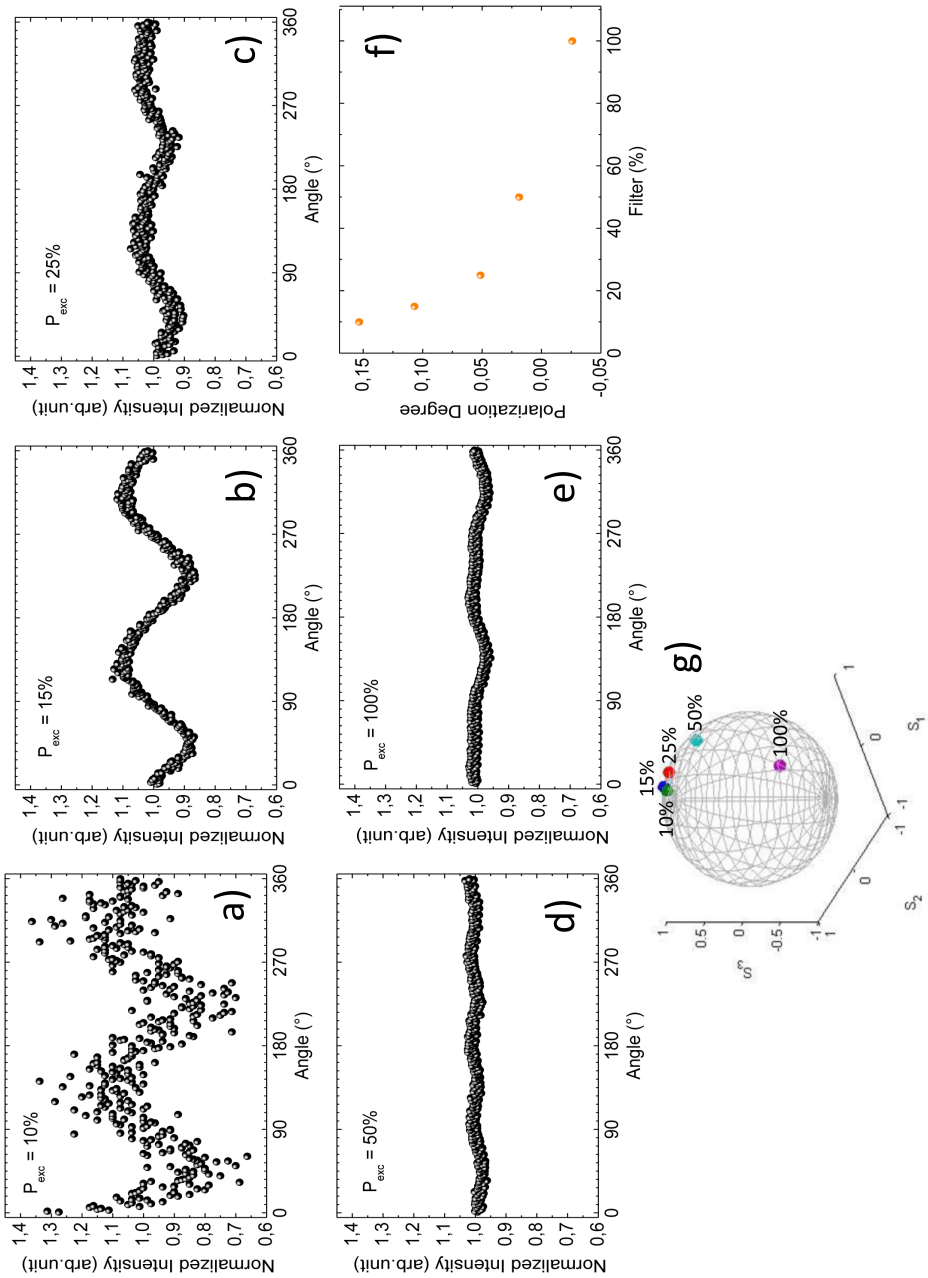

Figure B.4: (a)-(e) Modulation of the normalized intensity of the direct gap PL peak from $n-$Ge at T=50 K. (f) Polarization degrees calculated by the Stokes analysis on the data reported in (a)-(e), as a function of the excitation power (attenuation). (g) Poincaré sphere of the polarization type for the data reported in (a)-(e).

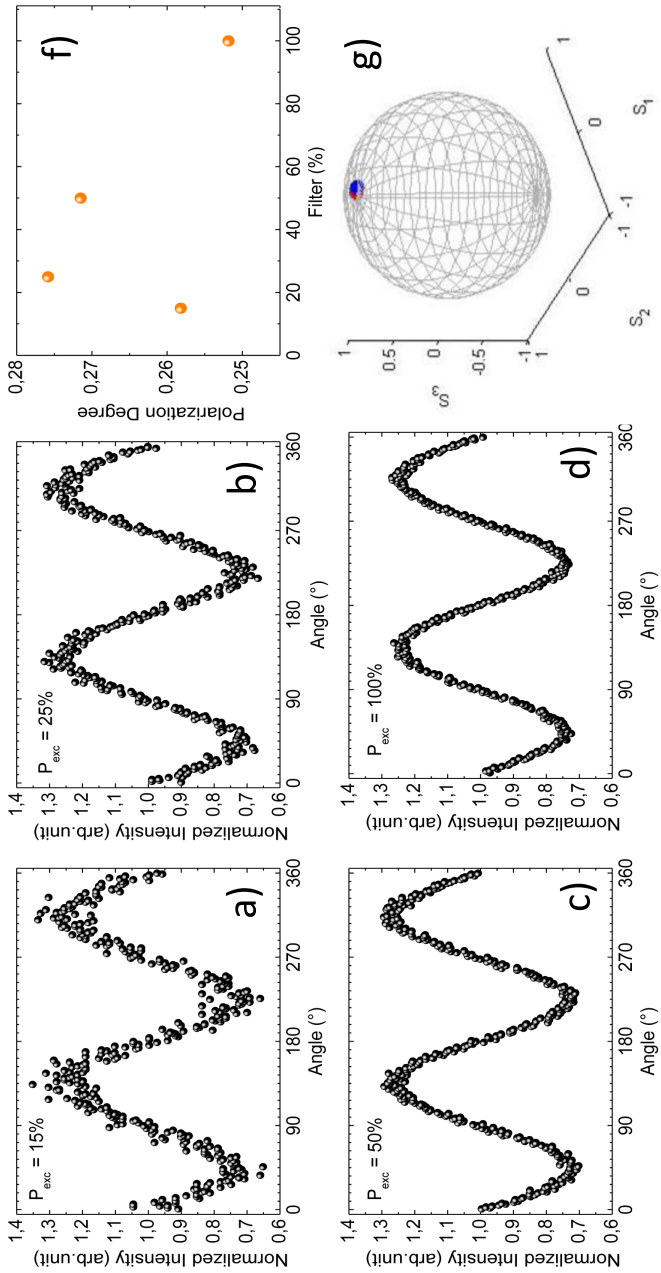

Figure B.5: (a)-(d) Modulation of the normalized intensity of the direct gap PL peak from $n-$Ge at T=120 K. (e) Polarization degrees calculated by the Stokes analysis on the data reported in (a)-(d), as a function of the excitation power (attenuation). (f) Poincaré sphere of the polarization type for the data reported in (a)-(d).

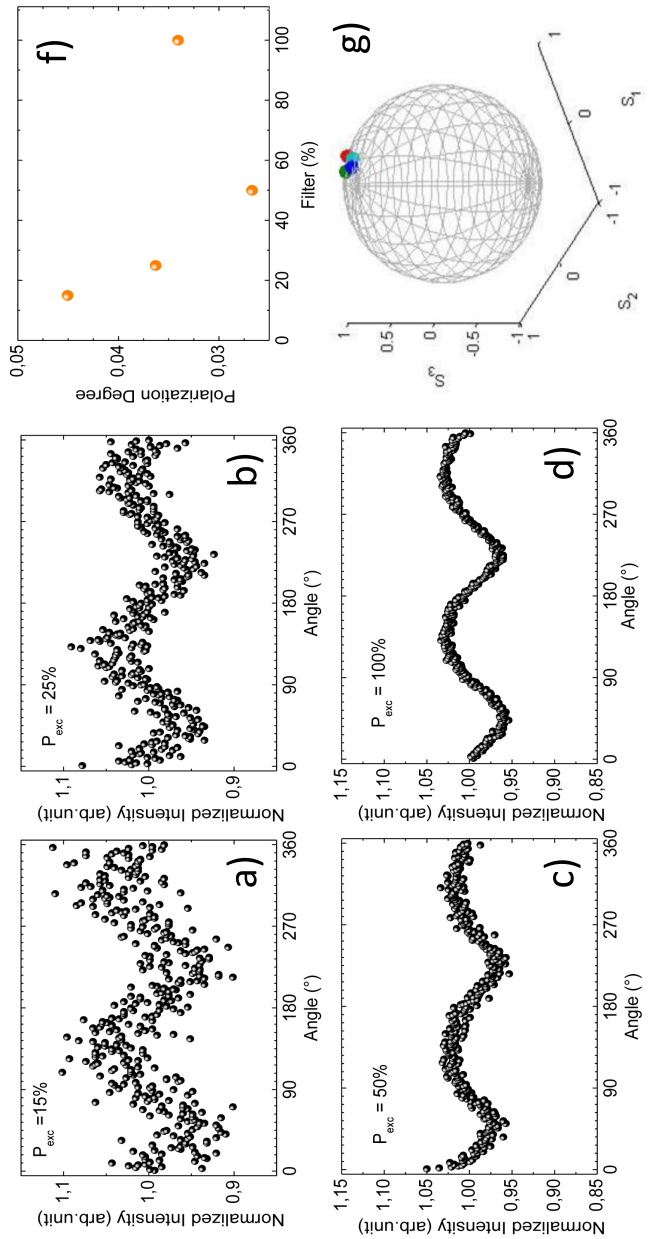

Figure B.6: (a)-(d) Modulation of the normalized intensity of the direct gap PL peak from $n-$Ge at T=160 K. (e) Polarization degrees calculated by the Stokes analysis on the data reported in (a)-(d), as a function of the excitation power (attenuation). (f) Poincaré sphere of the polarization type for the data reported in (a)-(d).

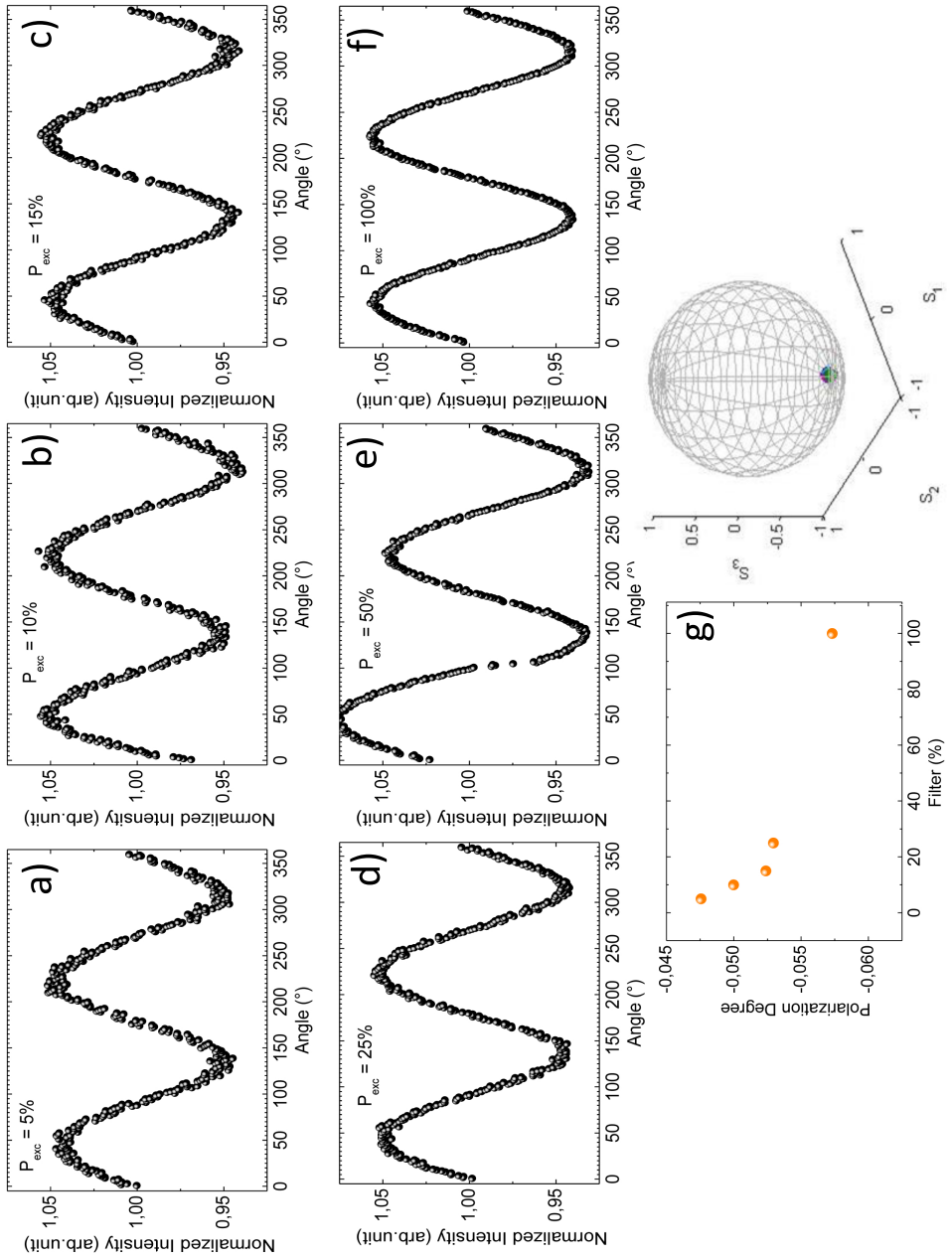

Figure B.7: (a)-(f) Modulation of the normalized intensity of the direct gap PL peak from p^+-Ge at T=50 K. (g) Polarization degrees calculated by the Stokes analysis on the data reported in (a)-(f), as a function of the excitation power (attenuation). In panel (e) the high intensity at low θ values is due to low stability of the laser power. (h) Poincaré sphere of the polarization type for the data reported in (a)-(f).

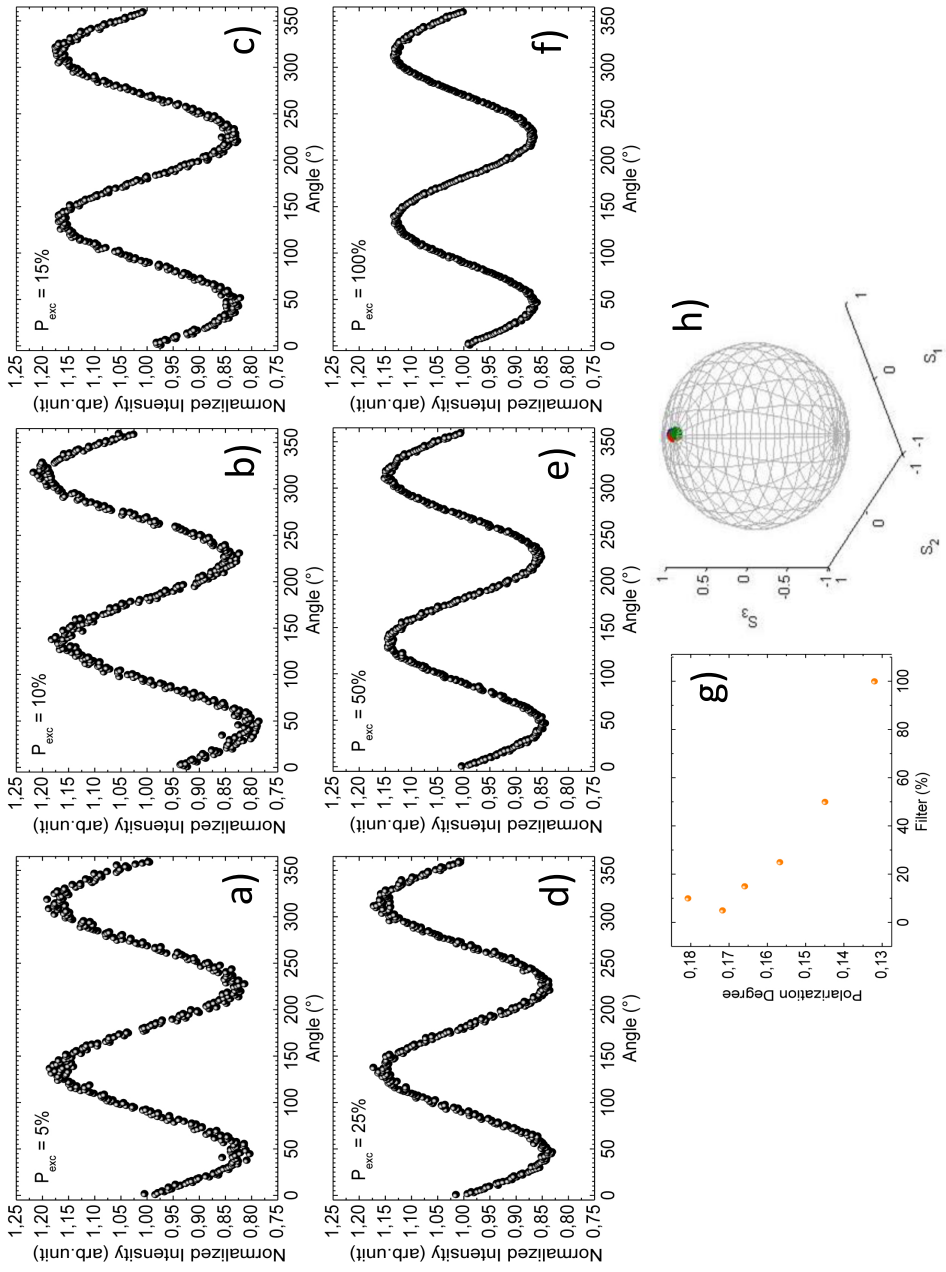

Figure B.8: (a)-(f) Modulation of the normalized intensity of the direct gap PL peak from p^+-Ge at T=120 K. (g) Polarization degrees calculated by the Stokes analysis on the data reported in (a)-(f), as a function of the excitation power (attenuation). (h) Poincaré sphere of the polarization type for the data reported in (a)-(f).

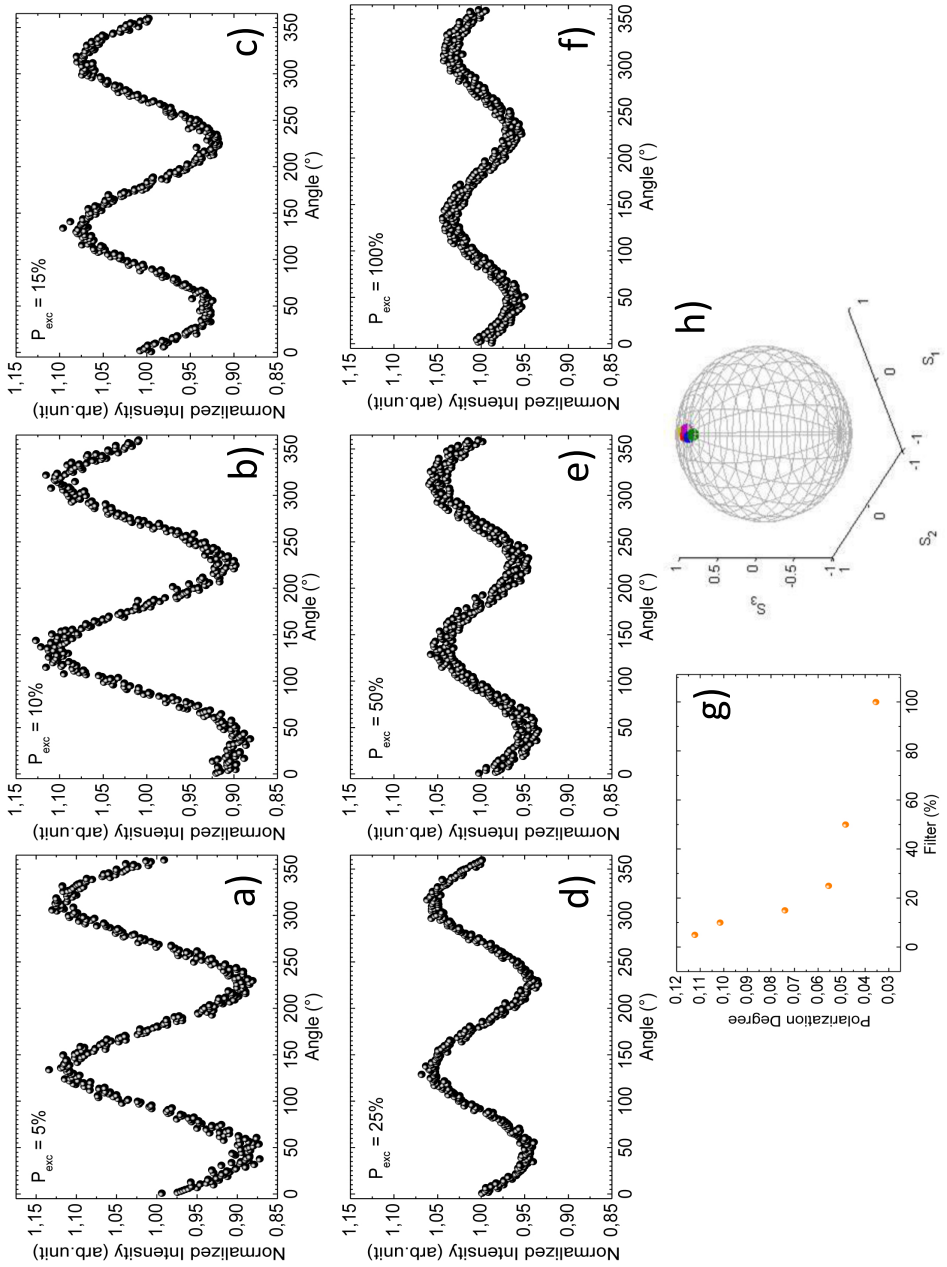

Figure B.9: (a)-(f) Modulation of the normalized intensity of the direct gap PL peak from p^+-Ge at T=160 K. (g) Polarization degrees calculated by the Stokes analysis on the data reported in (a)-(f), as a function of the excitation power (attenuation). (h) Poincaré sphere of the polarization type for the data reported in (a)-(f).

Appendix C

Ge/SiGe Multiple Quantum Wells

In this appendix we describe the Ge/SiGe quantum wells (QWs) samples analyzed in this thesis. All the samples were grown by low energy plasma enhanced chemical vapour deposition (LEPECVD) [57], an epitaxial growth technique characterized very high growth rates that can reach 10 nm/s. Such a high rate can be exploited for the epitaxial growth of the relaxed SiGe alloy buffer layers on Si [108].

In the following we outline the sample structure providing composition, thickness and strain of the epitaxial layers. We then discuss the electronic structure of the QWs, showing the band alignment. Finally we describe the modulation doped QWs.

C.1 Sample structure

The samples studied in this work were grown by LEPECVD on 100 mm Si(100) substrates with a resistivity of 1-10 Ωcm. In Figure C.1a) the general structure of our QW samples is sketched. Nominal values of Ge concentration and thickness of the layers in the different samples are listed in Table C.1.

In all the samples, the first part of the structure is a buffer layer graded from Si to $Si_{1-x}Ge_x$ capped with 2 μm of constant composition SiGe alloy with the same Ge concentration as the final part of the graded layer [Fig. C.1a)]. This forms the fully relaxed virtual substrate (VS) for the nanostructured part of the samples, which consists of a strain-balanced structure formed by pure Ge QWs and $Si_{1-y}Ge_y$ barriers with $y < x$.

In the VS the Ge molar fraction increases linearly from 0 to the final value x. The composition gradient is about 7% per micron, and the thickness of the graded layer is around 10-15 μm. Strain relaxation takes place in the whole VS, and the misfit dislocations extend through the whole layer increasing the dislocation interaction. As a result, the threading dislocation density in the final constant composition buffer is of the order of $10^5 - 10^7 cm^{-2}$, much lower than the one characterizing constant composition SiGe films directly deposited on Si [109].

Due to the dependence of SiGe lattice parameter on composition, the layer thicknesses were designed to balance the compressive strain in the wells with the tensile strain in the barriers. For this reason, the mean composition of the nanostructured region is chosen equal to the final composition

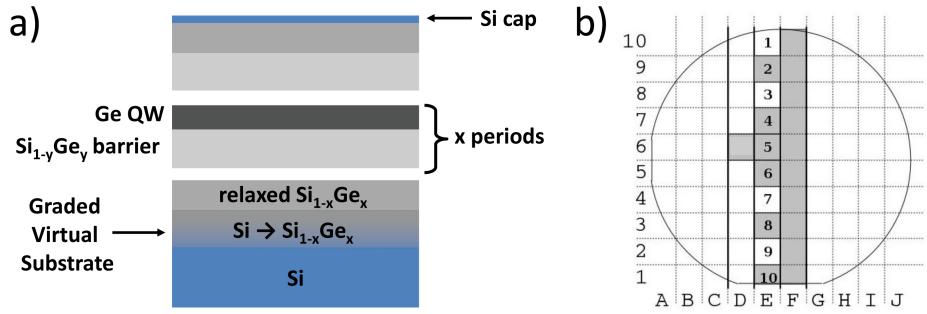

Figure C.1: a) Structure of a Ge QW sample. The cap layers are present in all the samples but 8351 sample. b) Subdivision of the wafer and labeling.

Table C.1: Structural parameters of the samples studied in the thesis. From the left to the right: sample name, number of QW-barrier periods, final Ge concentration of the VS, nominal Ge content in barrier, nominal thickness of QW and barrier, nominal doping.

sample	periods	VS	barrier (y)	d_{well}	$d_{barrier}$	doping
8351	100	0.90	0.85	3 nm	6 nm	-
7977	200	0.80	0.70	11 nm	19 nm	-
7909	200	0.90	0.85	10 nm	21 nm	-
8931	500	0.90	0.85	10 nm	21 nm	n type

of the VS:

$$x_{VS} = \frac{x_{well} \cdot d_{well} + y \cdot d_{barrier}}{d_{well} + d_{barrier}} \tag{C.1}$$

where x_{well}, y are the Ge molar fraction and d_{well}, $d_{barrier}$ the thickness of wells and barriers, respectively. Most of the samples were grown on a nominal $Si_{0.10}Ge_{0.90}$ relaxed VS, and present nominal $Si_{0.15}Ge_{0.85}$ barriers (Tab. C.1).

The growth rate is non uniform across the wafer due to inhomogeneities in the plasma intensity. As a result, from a single wafer samples are available with different well and barrier thicknesses but equal alloy compositions. The thickness of QW and barrier layers of the studied samples from each wafer were measured by X-ray diffraction, as reported in the chapters 3 and 4. Fig. C.1b) can be used to identify the position on the wafer of the samples studied in the various chapters. Samples from the same wafer but with different QW width were analyzed in the thesis to address the confinement effect on the spin properties of Ge QW in sec. 3.2 and 4.2.

C.2 Electronic band structure

Figure C.2 shows the results of tight binding calculations providing the complete band alignment and electronic states at the L and at Γ point of a 10 nm wide Ge/$Si_{0.15}Ge_{0.85}$ QW pseudomorphically grown on a relaxed $Si_{0.10}Ge_{0.90}$ substrate [59]. One of the most important features is that both the direct and the indirect gap present a type-I alignement [59], indeed both the L and Γ minima of the conduction band present lower energy in the QW than in the barrier layer. On the contrary, the energy of the X minimum of the conduction band (not shown in figure) is higher in the QW

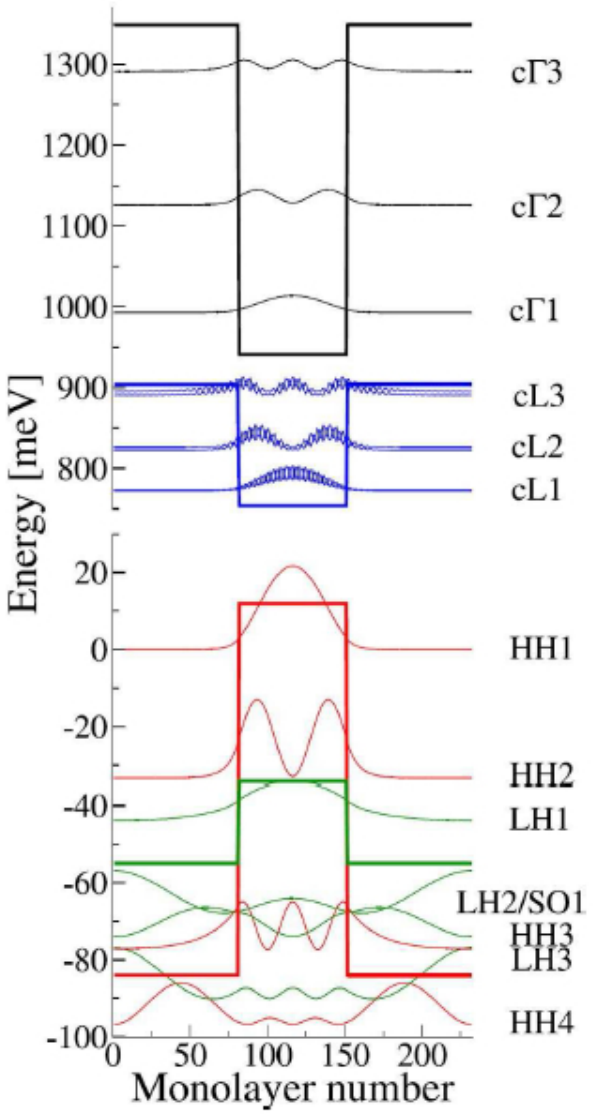

Figure C.2: Conduction and valence band edge profiles and the square amplitude of wave functions of the electron and hole confined states in Ge/$Si_{0.15}Ge_{0.85}$ QW pseudomorphically grown on relaxed $Si_{0.10}Ge_{0.90}$ substrate, obtained by tight binding calculations [59].

with respect to the barrier (negative band offset, type II alignment). The electronic structure of Ge/$Si_{0.3}Ge_{0.7}$ QWs grown on a relaxed $Si_{0.2}Ge_{0.8}$ substrate is similar to the one in Fig. C.2, with higher band offsets for both the *L* and Γ minima of the conduction band (see Fig. 3.1 of chapter 3).

In Fig. C.2 the conduction band offset at the Γ point is about 400 meV and this is expected due to the huge difference between the Ge and Si direct gap. At the *L* point, instead, the band offset is about 150 meV.

In the valence band, the heavy hole (HH) and the light hole (LH) states are not degenerate due to confinement in the well, and to strain effects in both the well and the barrier. The top of valence band has a HH character in the well, because of the compressive strain, and a LH character in the barrier, because of the tensile strain, thus there is a character inversion between the two layers. This affects the band offsets of HH and LH bands: the valence band offset is $\sim$100 meV for heavy-holes and only $\sim$20 meV for light holes.

Fig. C.2 reports also the energy of the confined states in conduction band at the Γ point (cΓn) and at the *L* point (cLn), and , in valence band, the energy of heavy hole (HHn) and light hole confined states (LHn) at the Γ point. The square amplitude of the wave functions of the electron and hole confined states is also shown. The wave function of the first state (n = 1) is almost completely confined inside the QWs especially for the cΓ1 and the HH1 states: the wavefunction penetration into the barriers increases with increasing the quantum number n.

C.3 Modulation doping

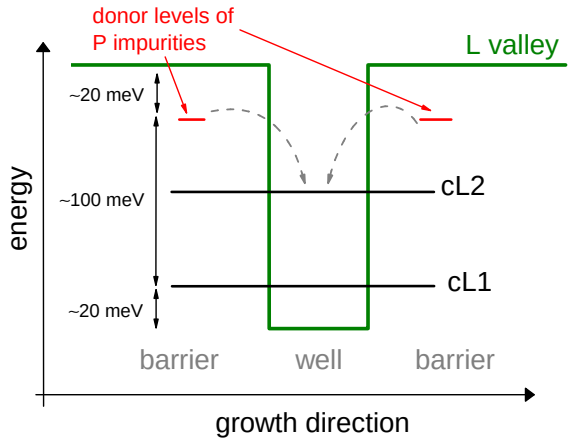

Figure C.3: Sketch of the conduction band energy profile and electronic levels in a 10 nm modulation n-doped Ge/$Si_{0.15}Ge_{0.85}$ QW at the *L* point of the Brillouin zone.

Sample 8931, used for the ESR study discussed in chapter 4, is a modulation doped sample [110]. Modulation n-doped QWs were obtained by depositing one monolayer of P atoms in all the $Si_{0.15}Ge_{0.85}$ barrier layers, at half of the barrier thickness.

P atoms are shallow donors in SiGe alloys, with ionization energies ranging from 13 meV in Ge to 45 meV in Si [16, 111]. Due to the low confinement energy of the first confined *L* state (Fig. C.2) the donor level in the barrier has an energy higher than the cL1 and cL2 states in the QW layer (Fig. C.3) favoring donor electron transfer to the confined *L* states of the QW.

The electrons transferred in the QW layer stay in the fundamental *L* minimum of the conduction band, since the valence band is completely occupied, and constitute a two-dimensional electron gas. We did observe experimental evidence of the two-dimensional electron gas in the cyclotron resonance signal (sec. 4.1.2) measured by ESR. For further details con modulation doping and its effects on the band energy profile see Ref. [110].

Appendix D

Temperature dependence of the PL spectrum of Ge QWs

In this appendix we report the PL spectra of Ge QWs samples analyzed in chapter 3 at different temperatures in the 4 - 300 K range. The colour-coded maps shown in Fig. 3.3 were obtained with the raw data displayed below.

D.1 Sample 7977-10

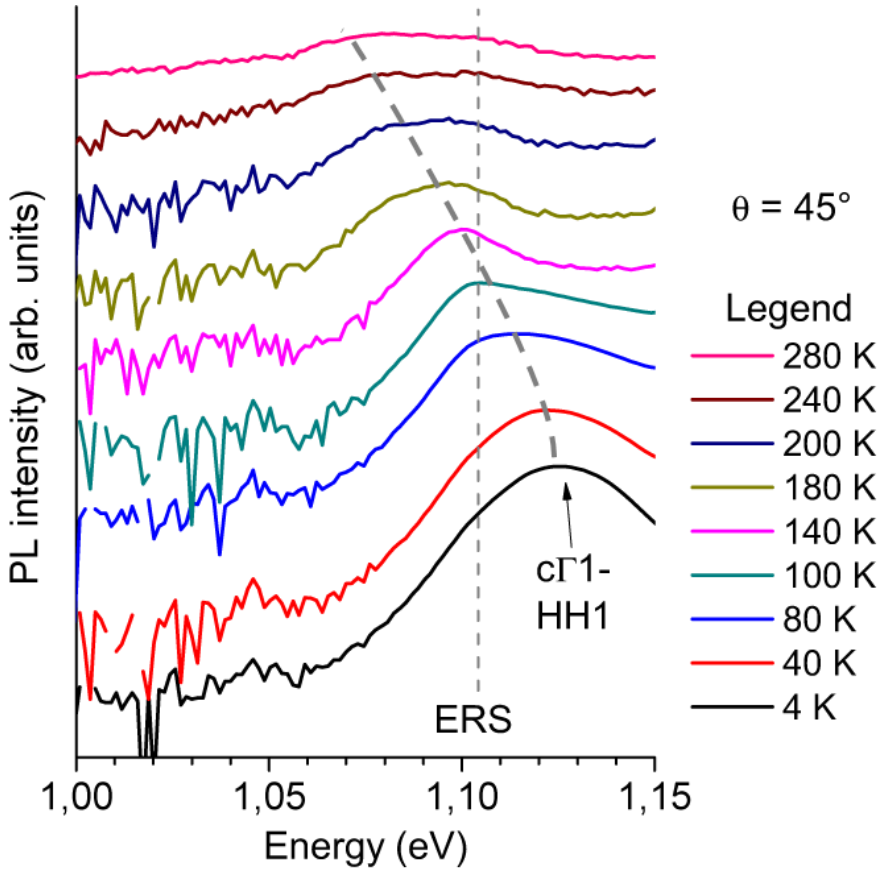

Figure D.1: PL spectra of sample 7977-10 at $\theta = 45°$ and at different temperatures in the 4 - 280 K range. The dashed lines are guides for the eyes. When the temperature increases the cΓ1-HH1 PL peak shifts to lower energies, according to the Varshni's law (Eq. 1.1), while the energy of the Electron Raman Scattering (ERS) signal (sec. 3.2) is almost constant.

D.2 Sample 7977-8

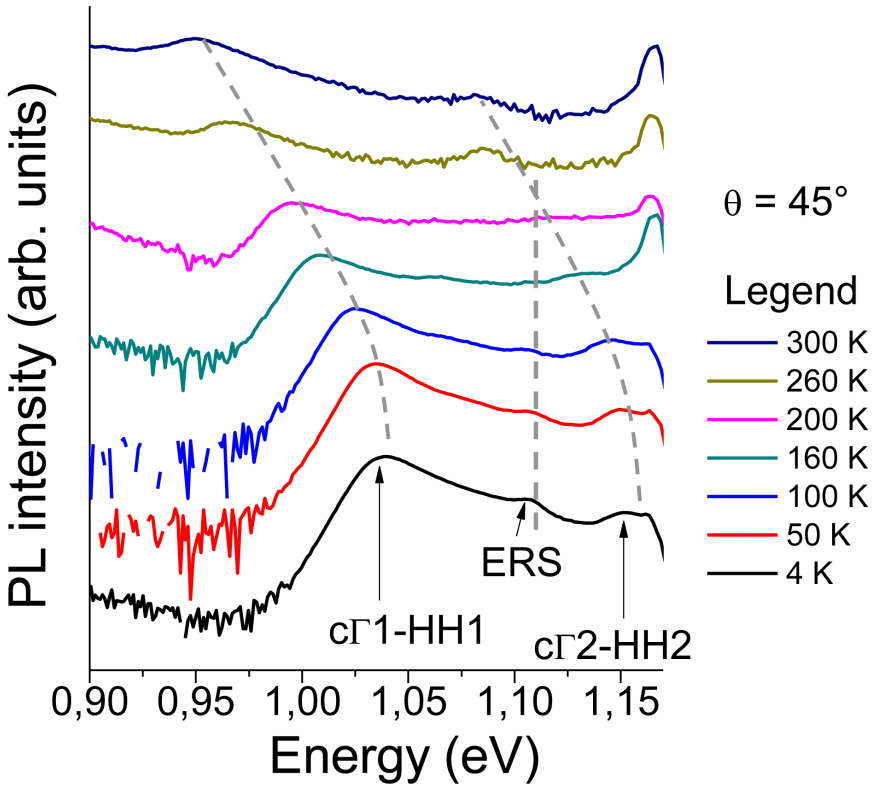

Figure D.2: PL spectra of sample 7977-8 at $\theta = 45°$ and at different temperatures in the 4 - 300 K range. The dashed lines are guides for the eyes. When the temperature increases the cΓ1-HH1 and the cΓ2-HH2 PL peaks shift to lower energies, according to the Varshni's law (Eq. 1.1), while the energy of the Electron Raman Scattering (ERS) signal (sec. 3.2) is almost constant. The peak around 1.165 eV at high temperatures is due to the laser straylight.

D.3 Sample 7977-4

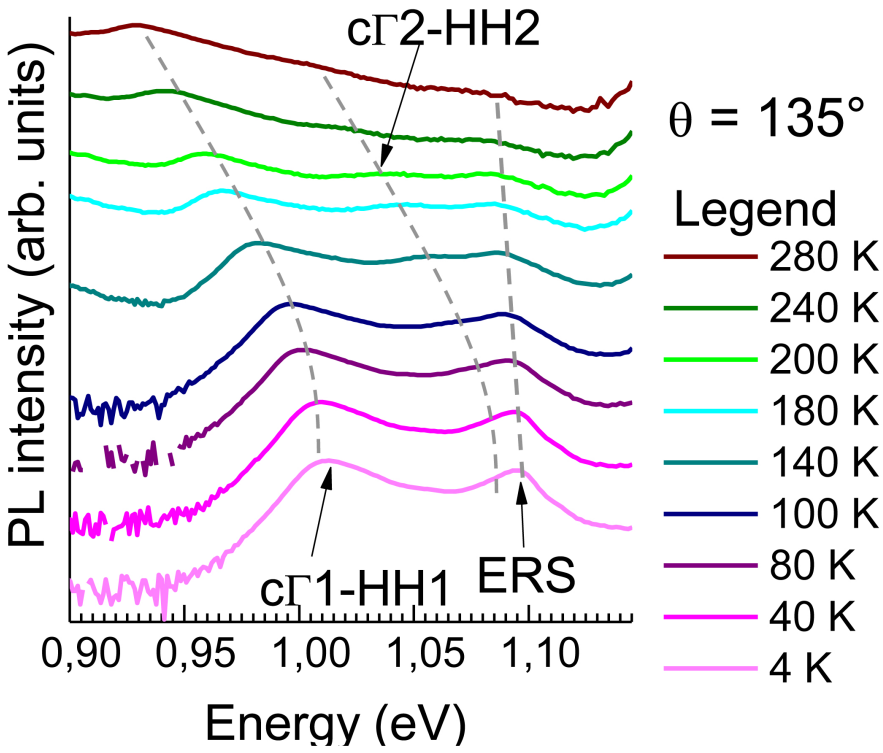

Figure D.3: PL spectra of sample 7977-4 at $\theta = 135°$ and at different temperatures in the 4 - 280 K range. The dashed lines are guides for the eyes. When the temperature increases the cΓ1-HH1 and the cΓ2-HH2 PL peaks shift to lower energies, according to the Varshni's law (Eq. 1.1), while the energy of the Electron Raman Scattering (ERS) signal (sec. 3.2) is almost constant.

Appendix E

Electron Spin Resonance

We provide here a brief description of the Electron Spin Resonance (ESR) technique, showing the experimental setup used for the measurements reported in chapter 4. In the following, we discuss origin and characteristics of the cyclotron resonance and the spin resonance signals. Further details about the technique and the analysis of the spin resonance can be found in Ref. [102].

E.1 Apparatus

The ESR measurements were carried out using a Bruker Elexsys 580 machine, and a Varian machine, similar to the former. For sake of simplicity we will describe only the first one. In Figure E.1 a sketch of the apparatus is reported. The microwave source is a Gunn diode, working at 9.4 GHz frequency. The microwave power is $\sim$200 mW; in our experiments the attenuation was usually set at 20 dB (2 mW).

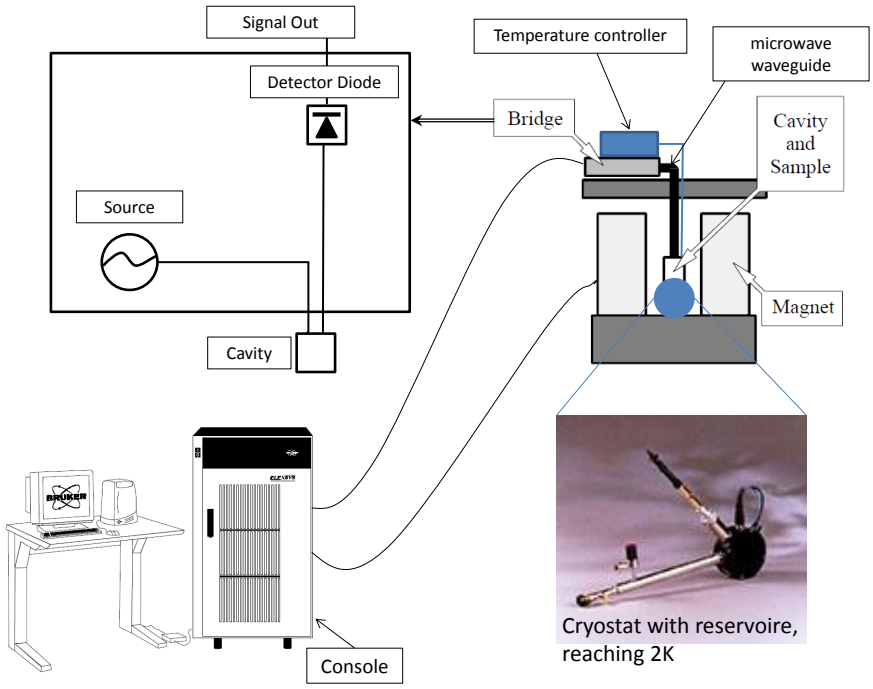

Figure E.1: Sketch of the experimental apparatus used for ESR measurements.

We used a rectangular cavity with dimensions about 20 mm$\times$30mm$\times$40mm, and we used in two illumination modes. The cavity presents an optical access on one side, which allowed us to perform measurements under illumination by a laser light. In case of illumination with white light, the light entered the cavity through the quartz holder on which the sample was mounted. The sample orientation was controlled by means of a goniometer. Since the cavity impedance depends on the microwave absorption of the sample, the matching between the cavity and the waveguide of the

microwaves is adjusted before each measurement. In our measurements the quality factor was $\sim$1300.

The detector is a Shottky barrier diode, whose optimum working condition is obtained when the diode current is around 200 μA.

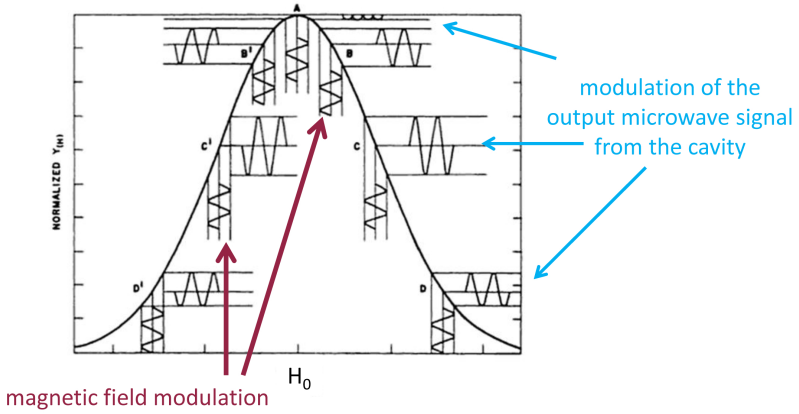

Figure E.2: Sketch of a spin resonance absorption peak as a function of the magnetic filed, together with the oscillating component of the magnetic field and the corresponding output signal from the cavity.

The magnetic field in the cavity is uniform, with an intensity that can be scanned from few tens of G to 15000 G. In ESR experiments a phase sensitive detection is used, obtained by adding an oscillating component to the uniform magnetic field scanned over a ΔH range, and by a lock-in detection system coupled with the magnetic field modulation [102]. As a result of the phase sensitive detection, the spectra show the first derivative of the spin resonance absorption signal (Fig. E.2), i.e. the commonly called "spin resonance". The amplitude of the field modulation is chosen to be lower or of the order of the peak-to-peak linewidth (in G) of the spin

resonance of interest, in order to avoid artifacts in the lineshape.

We used a helium flow Oxford instruments cryostat, equipped with a reservoir (shown in Fig. E.1).

E.2 Spin Resonance

The resonant absorption of electromagnetic radiation by unpaired electrons in a magnetic field provides the spin resonance signal [85]. Unpaired electrons in semiconductors can be found in partially filled bands, localized at isolated defects or impurities, or in broken bonds. According to the Zeeman effect two degenerate spin up and spin down states are splitted in energy by an applied uniform magnetic field. In a semiconductor the electronic spin states may be further splitted by the hyperfine interaction with nuclei and other effects [85]. In the following, we consider the simple case of a two spin state system.

Figure E.3a) reports a sketch of the spin-flip absorption of a microwave, taking place when the microwave energy hf matches with the Zeeman splitting between the spin up and spin down states. In ESR measurements hf is fixed, while the magnetic field H is scanned over a ΔH range [Fig. E.3]. In resonant condition:

$$hf = \left(+\frac{1}{2}g\mu_B\mu H\right) - \left(-\frac{1}{2}g\mu_B\mu H\right) = g\mu_B\mu H \equiv g\mu_B\mu H_0 \qquad \text{(E.1)}$$

where g is the g factor, μ_B the Bohr magneton, and thus H_0 is defined as the magnetic field providing the resonance condition. The absorption signal [Fig. E.3b)] as a function of the magnetic field is assumed to be a Lorentian curve (see details at end of this section), whose peak position is found at

H_0. The area of the absorption signal is usually proportional to the number of unpaired spins in the sample [102].

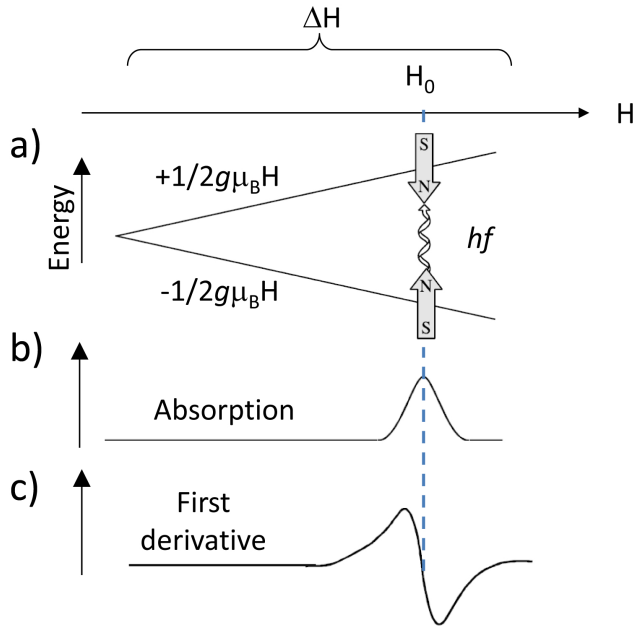

Figure E.3: Panel a): Zeeman splitting of two spin up and spin down states as a function of the magnetic field. Panel b): absorption signal of an electromagnetic wave with energy hf taking place at resonance condition with the Zeeman splitting. Panel c): first derivative of the absorption signal, observed in ESR measurements with phase sensitive detection.

The Lorentzian derivative lineshape [Fig. E.3c), Fig. E.4] has the normalized form [102]:

$$Y'(H) = \frac{16\, y'_m\, [(H - H_0)/0.5\,\Delta H_{pp}]}{\left\{3 + [(H - H_0)/0.5\,\Delta H_{pp}]^2\right\}^2} \tag{E.2}$$

where y'_m is the maximum peak intensity, and ΔH_{pp} is the peak-to-peak linewidth of the spin resonance. The spin resonance signal provides many information on the spin properties of carriers, particularly we discuss in the following the g factor, the spin decoherence time (T_2), and the spin relaxation time (T_1). The estimation of these parameters for conduction electrons in Ge QWs is discussed in chapter 4.

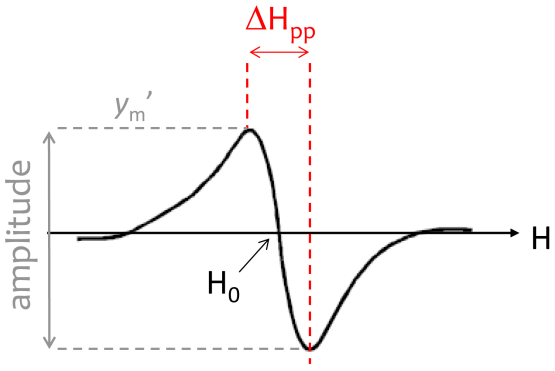

Figure E.4: Example of lorentian spin resonance.

In the spin resonance line, the H_0 value can be identified as the magnetic field at which the curve changes sign and curvature (Fig. E.4). The g factor is then easily obtained by Eq. E.1, once the microwave frequency is known:

$$g = \frac{hf}{\mu_B \mu H_0} \tag{E.3}$$

ESR measurements can provide g estimations with great accuracy. Knowing f (in GHz) and H_0 (in kG) with $1/10^5$ accuracy, the g value can be estimated with an accuracy of $1/10^4$.

In thermal equilibrium the spin up ($\uparrow$) and the spin down ($\downarrow$) states splitted by the Zeeman effect present two different populations $N_\uparrow$ and $N_\downarrow$, respectively. Assuming that the spin up state is the one at higher energy, then $N_\uparrow < N_\downarrow$. The microwave absorption perturbs this equilibrium increasing $N_\uparrow$, and reducing the difference between the two populations. Besides, the spin system is coupled to the lattice of the semiconductor, and there is always a finite probability for an energy transfer during which the spin relaxes from its higher energy ($\uparrow$) state to the lower energy ($\downarrow$) state. The relaxation processes restore the energy level populations to their thermal equilibrium values, and are characterized by the *spin-lattice* relaxation time, i.e. T_1. As a result, the population difference between the two spin states is governed by the relation between the microwave power and T_1 [102]. For high microwave powers and/or long T_1 the spin system saturates the microwave absorption, providing a new thermal equilibrium between the two spin states and causing the population difference to disappear. This condition is called *saturation regime*.

In saturation regime the linewidth of the spin resonance increases, and the amplitude (Fig. E.4) of the signal decreases. In order to estimate T_1, the value of the linewidth of the absorption peak is needed, both in and out of the saturation regime. T_1 can then be calculated by [102]:

$$T_1 = \frac{\left(\frac{\Delta H_{1/2}}{\Delta H^0_{1/2}}\right)^2 - 1}{\left(\frac{g\mu_B H_1}{\hbar}\right)^2 T_2} \tag{E.4}$$

where $\Delta H_{1/2}$ ($\Delta H^0_{1/2}$) is the measured linewidth in (out of) saturation regime, and H_1 the amplitude of the magnetic field of the microwave inside the

sample. For a lorentzian curve, $\Delta H_{1/2}$ can be estimated from the peak-to-peak linewidth of the spin resonance line: $\Delta H_{1/2} = \sqrt{3}\Delta H_{pp}$ (Fig. E.4).

Another spin depolarization mechanism is provided by the magnetic dipole interactions among spin oriented carriers. These interactions affect the spin phase, making the spin precessing around the external magnetic field. In contrast to the spin-lattice relaxation, there is no transfer of energy from or to the spin system. Therefore, this spin-spin relaxation (spin decoherence) is usually faster than the former. One possible spin-spin relaxation mechanism arises from the local field inhomogeneities resulting from the surrounding dipoles, leading to a distribution of precession frequencies. Since the individual magnetic moments precess with different frequencies, the overall magnetization decays. Usually this relaxation process is assumed to occur exponentially with a time constant T_2 [102].

The spin decoherence time influences the linewidth of the spin resonance, and can be calculated from the homogeneous (lorentzian) linewidth through the formula [102]:

$$T_2 = \frac{\hbar}{g\mu_B}\frac{2}{\mu\Delta H^0_{1/2}}. \tag{E.5}$$

Often the homogeneous linewidth is masked by effects providing a gaussian broadening. For instance, inhomogeneities in the crystal provide regions with different effective magnetic fields, which correspond to a random distribution of the g factor around an average value. In case of gaussian lineshape the measured $\Delta H_{1/2}$ is usually larger than $\Delta H^0_{1/2}$, and the *ensemble* spin decoherence time (T_2^*) can be estimated [3], which is $\leq T_2$.

E.3 Cyclotron Resonance

In chapter 4 we discussed the cyclotron resonance (CR) signal due to the two-dimensional electron gas in Ge MQW samples. The CR is due to the coupling between the circular motion of carriers in uniform magnetic field and the microwaves. Since in our ESR measurements the microwave frequency f is fixed, then the resonance condition is set when the frequency of the circular motion of free carriers equals f. According to the Lorentz's law, electrons moving in a uniform magnetic field experience a force $\vec{F}$ given by:

$$\vec{F} = e\vec{v} \times \mu\vec{H} \tag{E.6}$$

where e is the electron charge, $\vec{v}$ its velocity, μ the magnetic permeability of the environment, and $\vec{H}$ the magnetic field. Setting the Lorentz's force equal to the centripetal force, we obtain the cyclotron frequency of the circular motion:

$$f_c = \frac{e\mu H_\perp}{2\pi m^*} \tag{E.7}$$

where m^* is the carrier effective mass, and $H_\perp$ the magnetic field component perpendicular to $\vec{v}$. As a result of these simple assumptions, one can expect that scanning the magnetic field over a wide range, the CR absorption signal would provide a peak at the value of $\vec{H}$ validating the resonance condition. Indeed, in ESR spectra the CR absorption signal consists of a dip, whose position depends on the cyclotron frequency. The intensity of the dip is related to the carrier concentration, and the dip width to the carrier mobility [98]. A detailed discussion of the CR in semiconductors can be found in Ref. [98]; in particular for bulk Ge see Ref. [112]. In the following, we focus on the behavior of the CR signal in two-dimensional (2D) structures.

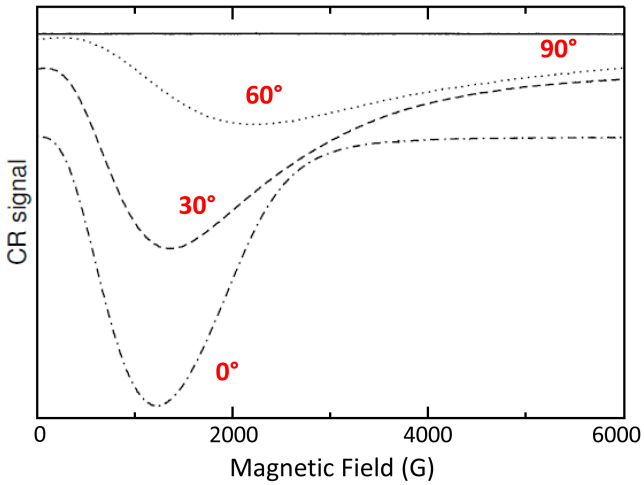

Figure E.5: CR spectra of a two-dimensional electron gas in Si/SiGe QWs, at various orientations [113]. The spectra are labeled by the values of θ. As θ increases, the minimum of this signal moves towards higher magnetic fields and the dip becomes shallower.

In quantum wells (QWs) carriers are confined in one direction, thus they can move only in-plane. For this reason, only the component of $\vec{H}$ perpendicular to the well plane is effective. As a result, the cyclotron frequency depends on the QW orientation with respect to $\vec{H}$:

$$f_c = \frac{e\mu H \cos\theta}{2\pi m^*} \tag{E.8}$$

where θ is the angle between $\vec{H}$ and the normal direction to the well plane.

As an example, Figure E.5 reports the CR signal of a two-dimensional electron gas measured in Si/SiGe QWs for different orientations of the external $\vec{H}$ [113]. The dip shifts to larger values of the magnetic field with

$(\cos\theta)^{-1}$, which is characteristic for a two dimensional system, according to Eq. E.8. Also the dip intensity depends on the angle. For in-plane field ($\theta = 90^\circ$) the signal is flat, indicating that no cyclotron resonance takes place because of the carrier confinement in the direction perpendicular to $\vec{H}$. On the contrary, for $\vec{H}$ perpendicular to the QW plane ($\theta = 0^\circ$) the resonance signal is maximum (Eq. E.8).

Bibliography

[1] R. R. Parsons. *Phys. Rev. Lett.*, **23**:1152, 1969.

[2] R.C. Miller and D. A. Kleinman. *J. Lumin.*, **30**:520, 1985.

[3] I. Zutič et al. *Rev. Mod. Phys.*, **76**:323, 2004.

[4] E. Yablonovich. *IEEE Proceedings*, , 2003.

[5] R. Jansen. *Nature Materials*, **11**:400, 2012.

[6] J.L. O'Brien et al. *Phys. Rev. B*, **64**:161401, 2001.

[7] F. A. Zwanenburg et al. *Rev. Mod. Phys.*, **85**:961, 2013.

[8] M. I. Dyakonov, editor. *Spin Physics in Semiconductors*. Springer, 2008.

[9] A. A. Konakov et al. *Semiconductors*, **47**:1508, 2013.

[10] Z. Wilamowski et al. *Physica E*, **16**:111, 2003.

[11] G. Lampel. *Phys. Rev. Lett.*, **20**:491, 1968.

[12] G. Grzybowski et al. *Phys. Rev. B*, **84**:205307, 2011.

[13] K. Hamaya et al. *J. Appl. Phys.*, **113**:183713, 2013.

[14] L. M. Roth and B. Lax. *Phys. Rev. Lett.*, **3**:217, 1959.

[15] T. Andlauer and P. Vogl. *Phys. Rev. B.*, **79**:045307, 2009.

[16] D. K. Wilson. *Phys. Rev.*, **134**:A265, 1964.

[17] E. M. Gershenzon et al. *Phys. Stat. Sol. B*, **49**:411, 1972.

[18] F. Meier et al. *Phys. Rev. Lett.*, **49**:747, 1982.

[19] J.-M. Tang et al. *Phys. Rev. B*, **85**:045202, 2012.

[20] E. J. Loren et al. *Appl. Phys. Lett.*, **95**:092107, 2009.

[21] E. J. Loren et al. *Phys. Rev. B*, **84**:214307, 2011.

[22] P. Li et al. *Phys. Rev. B*, **86**:085202, 2012.

[23] C. Guite and V. Venkataraman. *Appl. Phys. Lett.*, **101**:252404, 2012.

[24] P. Li et al. http://arxiv.org/abs/1307.4745v1.

[25] A. Jain et al. *Appl. Phys. Lett.*, **99**:162102, 2011.

[26] Y. Zhou et al. *Phys. Rev. B*, **84**:125323, 2011.

[27] J. Wagner and L. Viña. *Phys. Rev. B*, **30**:7030, 1984.

[28] F. Wooten. *Optical properties of solids, Chapter 5*. Academic Press, inc., USA, 1972.

[29] Y. Yu and M. Cardona. *Fundamentals of Semiconductors: Physics and Materials Properties*. Springer-Verlag, Heidelberg, 2010.

[30] G. Mak and H. M. van Driel. *Phys. Rev. B*, **49**:16817, 1994.

[31] J. I. Pankove. *Optical processes in semiconductors*. Nick Holoyak Jr. ed., New Jersey, 1971.

[32] E. Gaubas and J. Vanhellemont. *Appl. Phys. Lett.*, **89**:142106, 2006.

[33] Landolt-Börnstein. Numerical data and functional relationships in science and technology, iii/17a. Springer, Berlin, 1982.

[34] R. R. Lieten et al. *Phys. Rev. B*, **86**:035204, 2012.

[35] Y. P. Varshni. *Physica*, **34**:149, 1967.

[36] C. Haas. *Phys. Rev.*, **125**:1965, 1962.

[37] Y. Yin et al. *Phys. Rev. B*, **52**:8951, 1995.

[38] F. Pezzoli et al. *Phys. Rev. B*, **88**:045204, 2013.

[39] F. Meier and B. P. Zakharchenya, editors. *Optical Orientation, Modern Problems in Condensed Matter Science*. North-Holland, 1984.

[40] X. Sun et al. *Appl. Phys. Lett.*, **95**:011911, 2009.

[41] T. Nishino and Y. Hamakawa. *J. Phys. Soc. Jpn.*, **26**:403, 1969.

[42] C. Lange et al. *Phys. Rev. B*, **81**:045320, 2010.

[43] E. Gatti et al. *Appl. Phys. Lett.*, **98**:031106, 2011.

[44] A. Jain et al. *Phys. Rev. Lett.*, **109**:106603, 2012.

[45] X. Q. Zhou et al. *Phys. Rev. B*, **50**:5226, 1994.

[46] F. Bottegoni et al. *Appl. Phys. Lett.*, **102**:152411, 2013.

[47] K.-R. Jeon et al. *Phys. Rev. B*, **84**:165315, 2011.

[48] K. Kasahara et al. *J. Appl. Phys.*, **111**:07C503, 2012.

[49] L.-T. Chang et al. *Semicond. Sci. Tech.*, **28**:015018, 2012.

[50] R. I. Dzhioev et al. *Phys. Rev. B*, **66**:245204, 2002.

[51] G. Fishmann and G. Lampel. *Phys. Rev. B*, **16**:820, 1977.

[52] M. I. Miah. *Optics Communications*, **284**:1254, 2011.

[53] F. Pezzoli et al. *Phys. Rev. Lett.*, **108**:156603, 2012.

[54] J. Wagner and M. Cardona. *Phys. Rev. B*, **32**:8071, 1985.

[55] K. Tanaka et al. *Phys. Rev. B*, **50**:10694, 1994.

[56] J. C. Sturm et al. *Phys. Rev. Lett.*, **66**:1362, 1991.

[57] C. Rosenblad et al. *J. Vac. Sci. Technol. A*, **16**:2785, 1998.

[58] M. Virgilio and G. Grosso. *J. Phys.: Condens. Matter*, **18**:1021, 2006.

[59] M. Bonfanti et al. *Phys. Rev. B*, **78**:041407(R), 2008.

[60] `http://www.nextnano.de`.

[61] D. J. Paul. *Phys. Rev. B*, **77**:155323, 2008.

[62] Eleonora Gatti. *Recombination processes and carrier dynamics in Ge/SiGe multiple quantum wells*. Universitá degli Studi di Milano Bicocca, 2011.

[63] M. Virgilio and G. Grosso. *Phys. Rev. B*, **80**:205309, 2009.

[64] C. Lange et al. *Phys. Rev. B*, **79**:201306–3, 2009.

[65] J. Feldmann et al. *Phys. Rev. Lett.*, **59**:2337, 1987.

[66] T. Amand et al. *J. Appl. Phys.*, **72**:2077, 1992.

[67] J. Tignon. *Physica E*, **2**:126, 1998.

[68] A. Giorgioni et al. *J. Appl. Phys.*, **111**:013501, 2012.

[69] T. Uenoyama and L. J. Sham. *Phys. Rev. B*, **42**:7114, 1990.

[70] J. Rioux and J. E. Sipe. *Phys. Rev. B*, **81**:155215, 2010.

[71] F. Pezzoli et al. `http://link.aps.org/supplemental/10.1103/PhysRevLett.108.156603`.

[72] C. Lange et al. *Phys. Rev. B*, **85**:241303, 2012.

[73] M.Z. Maialle et al. *Phys. Rev. B*, **47**:15776, 1993.

[74] R. J. Elliott. *Phys. Rev.*, **96**:266, 1954.

[75] C. Weisbuch et al. *Solid State Commun.*, **37**:219, 1981.

[76] A. M. Gilinsky et al. *Europhys. Lett.*, **88**:17001, 2009.

[77] S. Pfalz et al. *Phys. Rev. B*, **71**:165305, 2005.

[78] D. J. Olego et al. *Appl. Phys. Lett.*, **58**:2654, 1991.

[79] A. Twardowski and C. Hermann. *Phys. Rev. B*, **35**:8144, 1987.

[80] T. B. Boykin et al. *Phys. Rev. B*, **69**:115201, 2004.

[81] J. H. Davies. *The Physics of Low-dimensional Semiconductors: An Introduction*. Cambridge University Press, New York, USA, 1998.

[82] S. Glutsch. *Excitons in Low-Dimensional Semiconductors*. Springer, Germany, 2004.

[83] C. Hautmann and M. Betz. *Phys. Rev. B*, **85**:121203(R), 2012.

[84] F. A. Baron et al. *Phys. Rev. B*, **68**:195306, 2003.

[85] G.W. Ludwig and H.H. Woodbury. Electron spin resonance in semiconductors. volume 13 of *Solid State Physics*. Academic Press, 1962.

[86] L. M. Roth et al. *Phys. Rev.*, **114**:90, 1959.

[87] L. M. Roth. *Phys. Rev.*, **118**:1534, 1960.

[88] K. J. Button et al. *Phys. Rev. Lett.*, **2**:161, 1959.

[89] G. Feher et al. *Phys. Rev. Lett.*, **3**:25, 1959.

[90] R. E. Pontinen and T. M. Sanders, Jr. *Phys. Rev. Lett.*, **5**:311, 1960.

[91] D. J. Paul. *Semicond. Sci. Technol.*, **19**:R75, 2004.

[92] E. B. Hanle et al. *Phys. Rev. B*, **12**:2553, 1975.

[93] T. Mitsuma and K. Morigaki. *J. Pjys. Soc. Jpn.*, **20**:491, 1965.

[94] R. W. Keyes and P. J. Price. *Phys. Rev. Lett.*, **5**:473, 1960.

[95] E. L. Ivchenko and A. A. Kiselev. *Sov. Phys. Semicond.*, **26**:827, 1992.

[96] A. A. Kiselev et al. *Phys. Rev. B*, **58**:16353, 1998.

[97] F. Shäffler. *Semicond. Sci. Technol.*, **12**:1515, 1997.

[98] E. D. Palik and J. K. Furdyna. *Rep. Prog. Phys.*, **33**:1193, 1970.

[99] P. Le Jeune et al. *Semicond. Sci. Technol.*, **12**:380, 1997.

[100] Landolt-Börnstein. Intrinsic properties of group iv elements and iii-v, ii-vi, and i-vii compounds, iii/22 a. Springer, Berlin, 1987.

[101] R. Winkler. *Spin-Orbit Coupling Effects in Two-Dimensional Electron and Hole Systems*. Springer, 2003.

[102] C. P. Jr. Poole. *Electron Spin Resonance: a comprehensive treatise on experimental technique*. Dover Publications, 1996.

[103] F. Maier et al. *Phys. Rev. B*, **87**:161305(R), 2013.

[104] E. Collett. *Field guide to polarization*. 2005.

[105] D.H. Goldstein. *Polarized Light*. 2010.

[106] L. Pavesi and M. Guzzi. *J. Appl. Phys.*, **75**:4779, 1994.

[107] I. Zutič et al. *Phys. Rev. B*, **64**:121201, 2001.

[108] C. Rosenblad et al. *Appl. Phys. Lett.*, **76**:427, 2000.

[109] F. K. Le Goues et al. *Appl. Phys. Lett.*, **60**:2862, 1992.

[110] F. Schaeffler. *Semicond. Sci. Technol.*, **12**:1515, 1997.

[111] G.L. Pearson and J. Bardeen. *Phys. Rev.*, **75**:865, 1949.

[112] G. Dresselhaus et al. *Phys. Rev.*, **98**:368, 1955.

[113] Hans Malissa. *Spin-Orbit Interaction of Electrons Confined in Low Dimensional Silicon-Germanium Structures*. Johannes Kepler Universitaet Linz, 2007.

Acknowledgements

First of all, I really want to thank Fabio Pezzoli, who shared with me grief and joy of this scientific adventure and of these years. In his friendship, he showed me what is research and he taught me the enthusiasm. I really want to thank Prof. Mario Guzzi, who took care of me step by step in science and bureaucracy, always with a human attention. They never gave up provoking me and 'betting on me'.

I would like to thank Giovanni Isella and Stefano Cecchi who carried out the sample growth at the LNESS labs in Como and provided the XRD measurements, thanks for the consults and the discussions.

I thank Prof. Wolfgang Jantsch, who hosted me at the Johannes Kepler Universitaet in Linz. I would like to thank him for his willingness and for teaching me the Electron Spin Resonance technique. My stay in Linz was really pleasant, and I will not forget the delicious dinners cooked by his wife, and their presence at my wedding.

I thank Prof. Fanciulli and Stefano Paleari for the ESR measurements at Milano-Bicocca and for the important discussions about the spin properties of conduction electrons in germanium.

I would like to thank Christoph Deneke and Carlos Inoki for the TEM

images of Ge MQWs samples (in short time!) at the Laboratório Nacional de Nanotecnologia of Campinas, and for the high-resolution XRD measurements at LNLS (Brazil).

I cannot forget to thank Prof. Hanan Dery of the Rochester University (New York) and his co-workers for the illuminating discussions and for the Monte Carlo simulations.

Finally, I thank Eleonora Gatti for the absorption spectra of Ge MQWs samples and for her company in every moment, Prof. Emanuele Grilli for his support particularly on the experimental, Emiliano Bonera who hosted me as assistant in the course of material physics, and all the people of our group.

Last but not least, I thank the people of the administrative staff and of the organs of Università degli studi di Milano-Bicocca and of the Johannes Kepler Universitaet of Linz for allowing me to do all I did in my PhD.

Laus Deo.